



---

**Forschungszentrum Karlsruhe**  
in der Helmholtz-Gemeinschaft

---

**Wissenschaftliche Berichte**  
FZKA 7518

# **Tuneable Electron Transport in Metallic Nanostructures**

**S. Dasgupta**

**Institut für Nanotechnologie**

**Oktober 2009**



**Forschungszentrum Karlsruhe**

in der Helmholtz-Gemeinschaft

Wissenschaftliche Berichte

FZKA 7518

**Tuneable Electron  
Transport in Metallic  
Nanostructures**

**Subho Dasgupta**

Institut für Nanotechnologie

vom Fachbereich Material- und Geowissenschaften der  
Technischen Universität Darmstadt genehmigte Dissertation

Forschungszentrum Karlsruhe GmbH, Karlsruhe

2009

Für diesen Bericht behalten wir uns alle Rechte vor

**Forschungszentrum Karlsruhe GmbH**  
Postfach 3640, 76021 Karlsruhe

Mitglied der Hermann von Helmholtz-Gemeinschaft  
Deutscher Forschungszentren (HGF)

ISSN 0947-8620

urn:nbn:de:0005-075182



# **Tuneable Electron Transport in Metallic Nanostructures**

vom Fachbereich  
Material- und Geowissenschaften  
der Technischen Universität Darmstadt  
genehmigte

**Dissertation**  
zur Erlangung des Grades eines  
**Doktors der Ingenieurwissenschaften (Dr.-Ing.)**

vorgelegt von  
**M. Tech Subho Dasgupta**  
geboren am 09.06.1980 in Kolkata, India

Eingereicht am: 20-05-2009  
Tag der Verteidigung: 27-08-09

Referenten:  
Prof. Dr.-Ing. Horst Hahn  
Prof. Dr.-Ing. Heinz von Seggern

Darmstadt 2009  
D17



Die vorliegende Arbeit wurde im Zeitraum von Dezember 2005 bis März 2009 im Institut für Nanotechnologie der Forschungszentrum Karlsruhe unter Herrn Prof. Dr.-Ing. Horst Hahn durchgeführt.

Hiermit versichere ich an Eides statt, dass ich die vorliegende Arbeit selbstständig und nur unter Verwendung der aufgeführten Hilfsmittel durchgeführt habe. Von mir wurde noch kein Promotionsversuch unternommen.

Karlsruhe, den 15.09.2009

---

Subho Dasgupta





To Alakananda



# Contents

<b>CHAPTER ONE: MOTIVATION.....</b>	<b>1</b>
<b>CHAPTER TWO: INTRODUCTION.....</b>	<b>5</b>
2.1 Theoretical Background.....	5
2.1.1 Electrochemistry.....	5
2.1.1.1 The Electrical double layer .....	5
2.1.1.2 Electrochemical terminologies and methods .....	7
2.1.1.3 Electrolytes.....	10
2.1.2 Extremely small nanostructures.....	15
2.1.3 Modification of the macro-properties of nanostructures with external field or spin coating from nanoparticle dispersion.....	17
2.2 Characterization Tools.....	20
2.2.1 X-ray reflectometry (XRR).....	20
2.2.2 Grazing incidence X-ray diffraction (GIXRD).....	22
2.2.3 Transmission electron microscopy (TEM).....	23
2.2.4 Atomic force microscopy (AFM).....	23
2.2.5 Scanning tunneling microscopy and spectroscopy (STM, STS).....	24
<b>CHAPTER THREE: REVERSIBLE TUNING OF RESISTANCE OF THIN GOLD FILMS.....</b>	<b>27</b>
3.1 Background.....	27
3.2. Experimental.....	28
3.3. Results .....	29
3.3.1 Electrochemical measurements.....	29
3.3.2 Surface charge-induced electrical transport.....	31
3.3.3 Atomic force microscopy .....	35
3.4. Analysis of the Results.....	37

<b>CHAPTER FOUR: TUNEABLE ELECTRON MOBILITY IN SURFACE-CHARGED CONDUCTING OXIDE THIN FILMS.....</b>	<b>45</b>
4.1 Background.....	45
4.1.1 Indium tin oxide (ITO) crystal structure.....	45
4.1.2 ITO band structure.....	47
4.1.3 Criteria for the transparent conducting behavior.....	49
4.2 Thin Film Preparation and Characterization.....	50
4.3 Results.....	52
4.3.1 Hall-effect measurements.....	52
4.3.2 Selection of the capacitive potential window.....	55
4.3.3 Surface charge induced electrical transport.....	56
4.3.4 Scanning tunneling microscopy and spectroscopy.....	58
4.4. Analysis of the Results.....	61
<b>CHAPTER FIVE: NANOPARTICLE CHANNEL FIELD-EFFECT TRANSISTOR WITH SOLID POLYMER ELECTROLYTE GATING.....</b>	<b>69</b>
5.1 Background.....	69
5.2 Preparation of the device.....	70
5.3 Results.....	74
5.3.1 Microstructural investigations.....	74
5.3.2 Electrochemistry and transport measurements.....	78
5.3.3 Calculation of the field-effect mobility.....	85
<b>CHAPTER SIX: RELATION TO FUTURE APPLICATION: PRINTABLE ELECTRONICS.....</b>	<b>89</b>
6.1 Printable Electronics.....	89
6.2 State of the Art.....	90
6.3 Suitability of the Present Device: Strengths and Limitations.....	91
6.4. Optimization of the Present Device Towards Industrial Needs.....	93
<b>CHAPTER SEVEN: CONCLUSIONS &amp; OUTLOOK.....</b>	<b>97</b>
7.1 Conclusions.....	97
7.2 Outlook.....	100
<b>REFERENCES.....</b>	<b>101</b>
<b>APPENDIX.....</b>	<b>115</b>
Appendix A: Hall-effect measurement: Sample data sheet.....	115
Appendix B: Variation of carrier concentration of ITO thin films.....	118
Appendix C: UV-VIS-IR spectroscopy of the ITO nanoparticles.....	120

*ACKNOWLEDGEMENT* .....123

*CURRICULUM VITAE*.....124

## List of figures

2.1	Model of the electric double layer .....	6
2.2	Equivalent circuit of an electrochemical cell .....	8
2.3	Simplified circuit of a three-electrode electrochemical cell .....	9
2.4	Schematic representation of the charged surface of a thin metal film .....	16
2.5	Schematic representation of the charged surface of a nanoporous film .....	17
2.6	Relative variation of the electric resistance of porous nanocrystalline Pt with the imposed specific charge density. ....	18
2.7	Length change of the 1 mm thick nanoporous gold sample in 50 mM sulfuric acid.....	19
2.8	(A) Change of the film coercivity for FePt and FePd thin films with respect to an external voltage; (B) percentage change in the Kerr rotation of the 2-nm thick FePt film. ....	20
3.1	Schematic representation of the sample geometry .....	29
3.2	Schematic representation of the experimental setup.....	30
3.3	Cyclic voltammogram of 7 nm Au film with different scan rates.....	31
3.4	Change in the sheet resistance with respect to applied potential for the 7 nm Au film.....	32
3.5	Change in the sheet resistance with respect to applied potential for the 9.3 nm Au film.....	33
3.6	Change in the sheet resistance with respect to applied potential for the 11.6 nm Au film .....	34
3.7	Comparison of the change in sheet resistance of Au films with different thickness and scan rates .....	35
3.8	(a) Section analysis of the AFM image of a 2.3 nm thin gold film, (b) Grain size distribution, (c) Line profile showing surface roughness .....	36
3.9	(a) Section analysis of AFM image of 7 nm gold thin film, (b) Grain size distribution, (c) Line profile showing surface roughness .....	37

3.10	Schematic of the decrease and increase in effective film thickness for a positive and negatively charged film surface.....	38
3.11	Change in resistance vs. applied surface charge measured and calculated from theoretical work.....	42
3.12	Change of effective thickness due to the shift of the center of mass of induced charge vs. surface charge density.....	43
4.1	Crystal structure of indium oxide.....	46
4.2	Variation of lattice parameter with tin doping in indium oxide.....	47
4.3	The band structures of (a) undoped $\text{In}_2\text{O}_3$ and (b) tin-doped $\text{In}_2\text{O}_3$ .....	49
4.4	X-ray reflectometry pattern for ITO thin films.....	51
4.5	(a) The grazing incidence X-ray diffraction patterns of the thin ITO films, (b) the film thickness is plotted against calculated average grain size.....	52
4.6	Data obtained from sheet resistance and Hall-emf measurements performed for the dry samples. The graphs show (a) carrier concentration, (b) resistivity, (c) Hall mobility, (d) electron mean-free path.....	54
4.7	The cyclovoltammogram of the ITO thin film (3.6 nm).....	55
4.8	Electrochemical cell for the charge-induced resistance measurement.....	56
4.9	Change in the sheet resistance ( $R_s/R_{s,0}$ ) of the ITO thin films. Figure (a) shows the gate potential variation, (b)-(e) resistance modulation of the ITO films with different film thickness.....	58
4.10	Scanning tunneling microscopy images of ITO thin films.....	60
4.11	Normalized conductance of the STS measurements on the grains (red) and above the grain boundaries (black).....	61
4.12	Comparison between the variations in the sheet resistance observed and calculated.....	62
4.13	Schematic diagram of the band structure of ITO thin film showing surface band bending.....	64
4.14	Sketch of the geometric surface of the ITO thin film (a); electronic surface of the same film (b); the increased electronic surface roughness and depleted grain boundaries with the negative ions at the surface (c). .....	66
5.1	Schematic of the electrochemically gated field-effect transistor device.....	71
5.2	Schematic representation of the preparation steps of the patterned substrate and ITO nanoparticulate film transistor.....	72
5.3	Optical micrograph of the device showing the source and drain made of sputtered ITO film and the channel made of ITO nanoparticles.....	73

5.4	Schematic representation of the cross-section of the device .....	74
5.5	(a-c) Conventional bright-field TEM image of the ITO nanoparticles .....	76
5.6	(a-c) Surface rendering of the ITO nanoparticles in the binarized and reconstructed tomography images with xy, xz and yz planes facing the plane of the paper .....	77
5.7	Cyclovoltammogram of the dispersed ITO nanoparticles prepared by spin-coating .....	79
5.8	Change in resistance of the ITO channel with the gate voltage varied with a constant rate of $5 \times 10^{-4}$ V/s .....	80
5.9	Change in the channel resistance in response to potential pulses between the gate and channel applied periodically (after 180 s) .....	81
5.10	Transfer characteristics of the solid polymer electrolyte-gated transistor .....	82
5.11	Drain current – drain voltage characteristic of the device with the gate voltage varied between 150 to -450 mV .....	83
5.12	(a) The drain current and (b) source current measured at different gate (= 450 to -650 mV) and drain voltage (= 20 to 100 mV) .....	84
5.13	Gate leakage of the device at different gate voltage .....	85
5.14	Schematic drawing shows the nanowire approximation of the nanoparticulate channel .....	86
6.1	Ink-jet printed solid polymer electrolyte (PVA+H <sub>2</sub> O+KF) on PMMA (A4 950K) coated glass substrate; (a) 200×200 μm, (b) 50×50 μm dots .....	92
6.2	Variation in channel resistance for polymer electrolyte gated ITO transistors with varying post annealing temperature .....	94
A.1	Schematic of the ITO film ITO film (Green) sputtered on silicon wafer (Blue) placed inside the puck .....	116
A.2	Photon Absorption spectra of ITO nanoparticles from ultraviolet to far-infrared radiation .....	120
A.3	Optical band gap of ITO nanoparticles with different temperature of annealing....	121



## List of tables

2.1	Non-aqueous solvent properties .....	11
2.2	Ionic conductivities of different classes of solid electrolytes .....	14
5.1	Morphological data of the ITO nanoparticles from volume analysis of the tomography images .....	78
6.1	Change in on/off ratio of the ITO-polymer electrolyte transistor with the variation in the post-annealing temperature.....	94
A.1	Hall-voltage in micro-volt for positive and negative magnetic field and with different configuration of the applied current and measured voltage .....	116
A.2	The bulk and sheet carrier concentration, positive and negative surface charge density and the corresponding decrease and increase in sheet carrier concentration of the ITO thin films.....	119

## List of abbreviations and symbols

<b>FET:</b>	Field-effect transistor
<b>UHV:</b>	Ultra high vacuum
<b>DLC:</b>	Double layer capacitance
<b>PZC:</b>	Point of zero charge
<b>OCP:</b>	Open circuit potential
<b>HEBM:</b>	High-energy ball milling
<b>ML:</b>	Monolayer
<b>IGC:</b>	Inert gas condensation
<b>JFET:</b>	Junction field-effect transistor
<b>XANES:</b>	X-ray absorption near-edge spectroscopy
<b>XRR:</b>	X-ray reflectometry
<b>GIXRD:</b>	Grazing incidence x-ray diffraction
<b>AFM:</b>	Atomic force microscopy
<b>TEM:</b>	Transmission electron microscopy
<b>STM:</b>	Scanning tunneling microscopy
<b>STS:</b>	Scanning tunneling spectroscopy
<b>RT:</b>	Room temperature
<b>FS:</b>	Fuchs-Sondheimer
<b>MS:</b>	Mayadas-Shatzkes
<b>ITO:</b>	Indium tin oxide
<b>FCC:</b>	Face centered cubic
<b>EMFP:</b>	Electron mean free path
<b>MIBK:</b>	Methyl iso-butyl ketone
<b>PMMA:</b>	Poly methyl methacrylate
<b>PVA:</b>	Poly vinyl alcohol
<b>PAN:</b>	Polyacrylonitrile
<b>PEO:</b>	Poly-ethylene oxide
<b>PVDF:</b>	Polyvinylidene fluoride
<b>HAADF-STEM:</b>	High angle annular dark field scanning transmission electron microscopy
<b>MAVI:</b>	Modular algorithm for volume analysis
<b>TFT:</b>	Thin film transistor
<b>PE:</b>	Printable electronics

**SWCNT:** Single-wall carbon nanotube  
**UV-VIS-NIR:** Ultraviolet-visible-near infrared

$\delta$ :	Screening depth
$E$ :	Electrode potential
$R_s$ :	Sheet resistance
$P$ :	Specularity parameter
$R$ :	Resistance, Grain boundary reflection coefficient
$\sigma$ :	Conductivity, Surface charge density
$\rho$ :	Resistivity
$\varepsilon$ :	Dielectric constant
$z_0$ :	Centre of mass of electron density profile
$D$ :	Repulsive pseudopotential
$n$ :	Charge carrier concentration
$E_F$ :	Fermi energy
$\hbar$ :	Reduced Planck's constant
$E_{g0}$ :	Intrinsic band gap energy
$E_{gm}$ :	Measured band gap energy
$m_c$ :	Mass of the conduction band
$m_v$ :	Mass of the valence band
$\omega_p$ :	Plasma frequency
$e$ :	Elementary charge
$\varepsilon_0$ :	Static dielectric constant
$\mu$ :	Carrier mobility
$\lambda$ :	Wavelength of radiation, Electron mean free path
$n_s$ :	Sheet carrier concentration
$v_F$ :	Fermi velocity
$\tau$ :	Relaxation time
$V_g$ :	Gate voltage
$V_D$ :	Drain voltage
$I_D$ :	Drain current
$V_p$ :	Pinch-off voltage
$\mu_{FE}$ :	Field-effect mobility
$I_{DSS}$ :	Drain current at zero gate bias
$g_m$ :	Transconductance
$S$ :	Subthreshold swing

## Chapter 1

# Motivation

Tailoring of the properties of metals and alloys by modifying their microstructure has been a well established branch in materials science over the last century. Large changes in properties were observed through alloying or introducing point (dopants, vacancies, interstitials) or line defects (dislocations). After the invention of nanocrystalline [Gle89, Bir84, Gle00, Sur95, Sur05] and highly disordered materials like metallic glasses [Joh86, Gre95, Wan04] large defect concentrations became a means to control various physical properties like mechanical [Val00, Kum03, Vep99, Eck05], electronic [Tri01, Nor08], magnetic [Hen99, Jil03], catalytic [Bec92] etc. Although many novel properties and consistent structure-property correlations were obtained, all these property modulations via microstructural modifications suffer from the problem of irreversibility. One way to overcome this limitation is to modify material properties by deviating from charge neutrality (i.e., by the application of an external electrostatic field) which can be reversible and dynamic. The field of *tuneable properties* of materials (Gle01a, Gle01b) deals with reversible variation of physical properties of ultra-fine nanostructures via large local electrostatic field applied at the surface/interface. It may also be noted that the principle of tuning properties of nanostructures by introducing surface charge applies quite generally to all physical properties (mechanical, magnetic, electronic, optical, catalytic) that depend on electronic structure/charge carrier concentration.

The idea of external, electrostatic field-controlled tuneable material properties defer from already reported field-effect devices in its material versatility. The reported field-effect devices in the literature are essentially limited to those materials with low carrier density such as semiconductors [Sze81], conducting polymers [Kel04] etc. In this respect, the most renowned and technologically important example of a controlled deviation from charge neutrality is the *Field-Effect Transistor (FET)*'. In an FET, an external field applied via a gate voltage manipulates the electronic transport through a semiconductor. In contrast, the field of tuneable properties of materials aims to include materials with large carrier concentration as well. The prerequisite to observe change in

physical property in such systems is the presence of a large applied local field in extremely small nanostructures. Following this basic principle, tuneable variation in mechanical [Wei03] and magnetic [Wei07] properties in metals have been reported recently.

In this thesis, the external field-controlled reversible variation in electronic transport in metallic systems is presented. Materials such as a pure metal, gold, to metallic conducting transparent oxide, Indium Tin Oxide (ITO), are covered. Model systems such as thin films versus less-defined nanoporous structures are studied. Finally, an electrochemically-gated nanoparticle channel transistor device is presented. The aim of the present study also includes inexpensive processing techniques to obtain field-effect device with appreciable performance. The '*high-tech*' electronic fabrication laboratories require precise control over the processing parameters, film quality, surfaces and interface quality etc. This in turn leads to large initial investments for the expensive ultra-high vacuum (UHV) and clean room processing. In contrast, the so-called '*dirty*' systems, comprising solution-processed nanoparticle channel device with electrochemical gating do not require UHV processing and therefore can easily be suitable for the inexpensive *macroelectronics*.

Next, the necessary conditions for tuning physical properties in metallic systems are summarized. A crucial parameter in any field-effect device is the spatial distance inside a conducting solid which deviates from charge neutrality upon applied field, is called *mean field penetration* ( $\delta$ ). For semiconductors this distance of external field penetration is known as *space-charged region* whereas in case of metals it is often referred to as *Thomas-Fermi screening depth*. The penetration of the applied field inside a conducting solid essentially depends on the free carrier concentration [Gha80, Tos79]. For a semiconductor with carrier concentration of the order of  $10^{16}/\text{cm}^3$ , field penetration or screening length can be as high as 100 nm (approximately 300 atomic layers) [Gle01a]. The number of carriers that can be injected by an external field using a dielectric (e.g.,  $\text{SiO}_2$ ) gating is also significantly higher compared to the already present carrier density. In contrast, in case of metals the carrier concentration is more than  $10^{22}/\text{cm}^3$ . This results in less than a monolayer screening length (0.25-0.3 nm for gold [Kem85]) which in turn produces a negligible change in carrier concentration with the dielectric gating. Consequently, in order to tune the properties of conductors via an external field very high induced surface charge density per unit volume is necessary. A high surface-to-volume ratio of nanoparticles is thereby one of the prerequisites to observe measurable changes in physical properties of materials with large carrier concentration.

Apart from the use of extreme nanostructures to maximize surface-to-volume ratio the other key to increase surface charge density is to utilize electrochemical charging. Most metals possess a high *double layer capacitance* (DLC); therefore, with the electrochemically applied surface charge a local field in excess of  $10 \text{ MVcm}^{-1}$  is possible; orders of magnitude higher than for any existing gate dielectrics. In addition, for a nanoporous structure with interconnected nanoparticles the necessity of the electrochemical gating increases even further as an electrolyte can penetrate the

nanopores to surround the nanoparticles from all sides. Therefore, each particle experiences the external field and a surface charge from all side as opposed to a dielectric gating where the field is applied only from one side and the particles far from the gate oxide interface hardly sense the applied field. The applied field (voltage) is of course limited to the predominantly capacitive double layer region of an electrolyte-metal combination to avoid redox reactions. Therefore, to examine only the field-effect and not any irreversible chemical phenomena non-adsorbing supporting electrolytes were used.

The motivation of the thesis includes:

- I. To tune the electronic transfer properties (electrical resistance) of metallic and high conducting nanostructures with electrochemical surface charge.
- II. To understand the observed effect quantitatively using thin film geometry as a model system. The thin film geometry facilitates control over the geometrical parameters such as the surface area and surface-to-volume ratio.
- III. To explore application possibilities of surface charge-induced tuneable variation of transport properties of nanostructures.

The present chapter (**first chapter**) includes the motivation of the thesis. In the **second chapter** the '*electrochemical double layer*' will be defined and electrochemical measurement techniques and terminologies will be introduced followed by a short summary on electrolytes. Next, the published articles on tuneable properties of nanomaterials will be summarized.. All the characterization techniques used in this study will also be introduced very briefly. The **third chapter** will deal with the experimental results and quantitative analysis of a surface charge-induced variation in sheet resistance in metallic (gold) thin films. The **fourth chapter** will deal with a conducting system (conducting oxide) with lower carrier density than a pure metal. Surface-charge induced variation in transport property of ultra-thin Indium Tin Oxide (ITO) films will be presented and it will be shown that a charge-induced reversible modulation in scattering cross-section leads to a large effect-size in electrical transport in conducting oxides. The **fifth chapter** will demonstrate an all-solid-state junction field-effect transistor device using ITO nanoparticles as the active layer and a solid polymer electrolyte as the gate dielectric. The **sixth chapter** will inquire the application possibilities of this aforementioned device. The summary and outlook will comprise the **seventh chapter**.

## CHAPTER ONE



## Chapter 2

# Introduction

### 2.1 THEORETICAL BACKGROUND

In this chapter the theoretical background of the thesis will be presented. The earlier work in the field of surface charge induced tuneable variation in physical properties of the materials will be discussed. The present study is interdisciplinary one; besides electronic transport measurements in nanostructures and device physics, it also deals with electrochemistry. Therefore it may be necessary to define a few electrochemical terminologies and methods in the beginning to facilitate a better understanding of the next sections of literature review.

#### *2.1.1 Electrochemistry*

##### *2.1.1.1 The electrical double layer*

The *electrical double layer* at the metal-electrolyte interface is almost analogous to a simple plate capacitor. Fig. 2.1 shows the schematic of a capacitive double layer at the metal/electrolyte interface with several models to explain the counter ion concentration near the surface of the contact. It was first proposed by Hermann Ludwig Ferdinand von Helmholtz in 1879, that a metal electrode immersed in an electrolyte forms a capacitive double layer at the metal/electrolyte interface [Rie87].

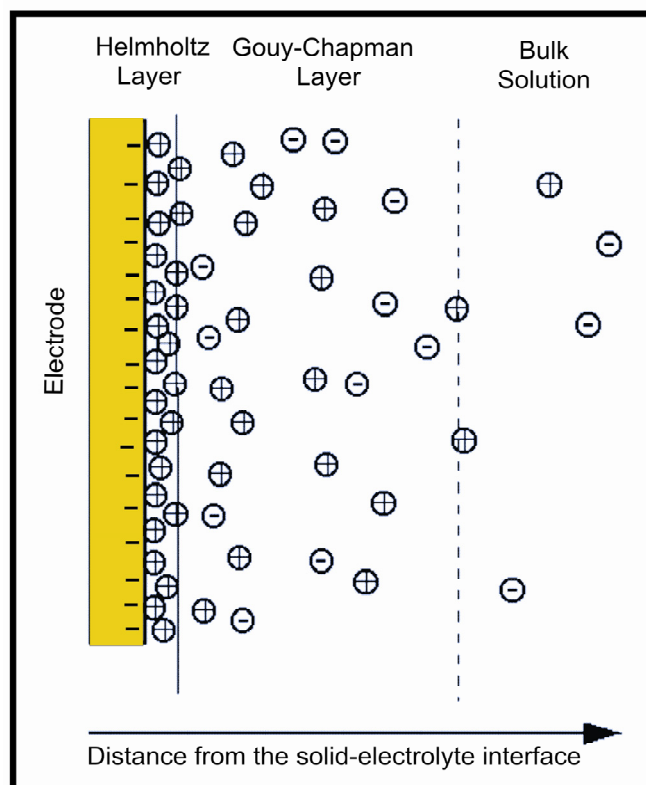


Figure 2.1 Model of the electric double layer

Helmholtz model (1879): In this model the double layer was mathematically treated as a simple capacitor with an immobilized layer of counter ions at the surface attached by electrostatic attraction; such that the surface charge is completely neutralized. Therefore, in the Helmholtz model the electric potential falls from its surface value to zero within the bulk solution over a thickness equal to the thickness of the counter ions attached to the surface.

Gouy-Chapman Model (1910-1913): In this model the random thermal motion of the ions is considered. Consequently, the counter ions cannot be immobilized unless they are chemically (or physically) adsorbed at the electrode surface. Therefore, the counter ions which neutralize the surface charge are spread out into the solution, forming what is known as a diffuse double layer. According to this model the surface potential drops slowly to zero in the bulk solution over a large distance (compared to the width of the Helmholtz layer) within the solution.

The Gouy-Chapman model gives a simple exponential potential decay with an increase in distance  $x$  from the Helmholtz plane [Pli08].

$$\Phi_x = \Phi_H e^{-kx} \quad (2.1)$$

where,  $\Phi_x$  is the potential at a distance  $x$  from the Helmholtz plane,  $\Phi_H$  is the potential

at the Helmholtz plane and  $k$  is the proportionality constant (Debye-Hückel parameter). The inverse of this constant ( $k^{-1}$ ) is the distance at which the potential,  $\Phi$ , drops to  $(1/e)$  of its initial value at the Helmholtz plane  $\Phi_H$ , and this distance is called the *double layer thickness* or the *diffuse layer thickness* or the *Gouy-Chapman layer thickness* ( $d_{GC}$ ).  $d_{GC}$  is given by [Jar97]:

$$d_{GC} = k^{-1} = \left( \frac{1000e^2 z^2 c N_A}{\epsilon_0 \epsilon_r k_B T} \right)^{-1/2} \quad (2.2)$$

where,  $c$  is the electrolyte concentration,  $z$  is the valency of the electrolyte,  $\epsilon_r$  is the dielectric constant of the solvent,  $N_A$  is the Avogadro number and other symbols with their usual meaning. Therefore,  $d_{GC}$ , is wider if the electrolyte concentration is lower, extends up to tens of nanometer [Tan05].

Stern Model (1924): This model is a combination of the Helmholtz and Gouy-Chapman models. In this model it is considered that there is indeed a layer of ions of one type (counter ions) near the electrode surface (Helmholtz layer), but the numbers are not enough to neutralize the charge. Hence the remainder of the charge is neutralized by a diffuse layer (Gouy-Chapman layer) extending out into the solution.

### 2.1.1.2 Electrochemical terminologies and methods

This section defines a few important electrochemical terminologies and measurement techniques which are used extensively throughout the thesis.

#### The equivalent circuit

Fig. 2.2 shows an equivalent circuit of an electrochemical cell [Rie87].  $\Delta\Phi_1$  and  $\Delta\Phi_2$  are the two electrode-solution potential differences, the difference between which ( $\Delta\Phi_1 - \Delta\Phi_2$ ) is the equilibrium cell potential,  $E$ .  $C_1$  and  $C_2$ , are the double layer capacitances (formed by the ion-electron electrical dipole at the electrode-solution interface) at the two electrodes,  $Z_{F1}$  and  $Z_{F2}$ , are the Faradaic impedances, and  $R$  is the electrolyte resistance.

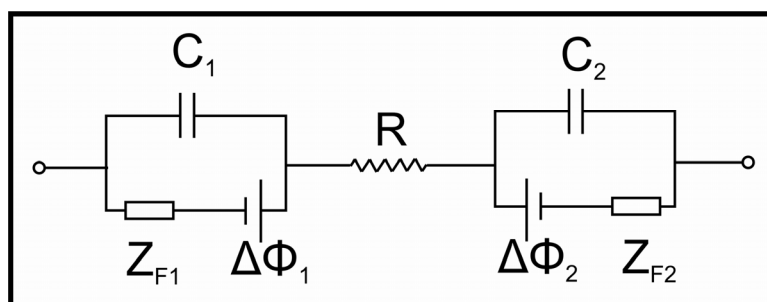


Figure 2.2 Equivalent circuit of an electrochemical cell

## Electrodes

**Working electrode:** The **working electrode**, (sometimes also referred to as the indicator electrode) in an electrochemical system is the electrode of interest. This is the electrode under study where the interesting electrochemical processes or reactions are occurring.

**Counter or Auxiliary electrode:** The **auxiliary electrode** which is also known as the **counter electrode**, is an electrode used in an electrochemical cell along with the working electrode to ensure that the current does not run through the reference electrode. Generally, the current through the counter electrode is not measured, however, in standard condition where no current is flowing through the reference electrode; the current through the counter should be same in magnitude, but opposite in sign to the current through the working. One important criterion which is often necessary for the counter electrode to have is a much larger surface area compared to the working in order to ensure that the electrochemical processes occurring on the working electrode are not surface area limited.

**Reference electrode:** A **reference electrode** should be an electrode with a stable and well-known electrode potential. A high stability is usually achieved by redox systems with the concentration of the participants of the redox reaction which do not change with time (buffered or saturated). For practical purposes a reference electrode should also be easily and reproducibly prepared and maintained, relatively inexpensive, stable over time and stable under a wide variety of conditions. Standard Calomel ( $E = +0.242$  V saturated) and silver/silver chloride ( $E = +0.225$  V saturated) electrodes are most commonly used as reference.

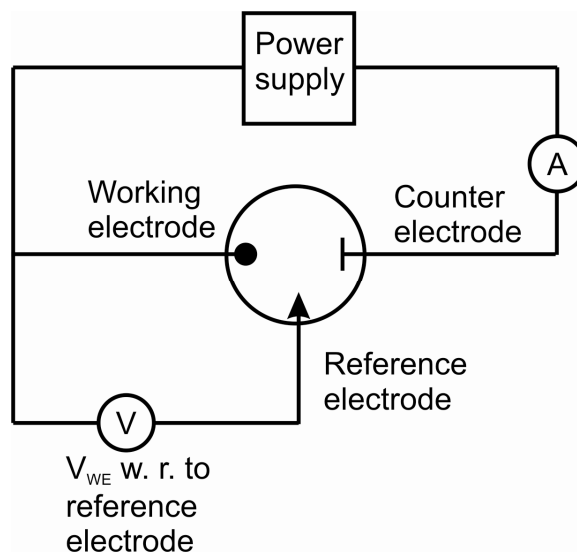


Figure 2.3 Simplified circuit of a three-electrode electrochemical cell

Until 1950 electrochemical cells used to comprise two electrodes, however, from the beginning of 1950's three-electrode electrochemical cells have started to be employed where a precise control over the potential of the working electrode is necessary. The control of potential of the indicator electrode is achieved with operational amplifiers and some further instrumentation; the device is called a potentiostat. A true reference electrode is used to measure the cell voltage accurately. A voltage follower attached to the reference electrode minimizes the current flowing through it. Therefore, the purpose of the auxiliary/counter electrode is to pass the bulk of the current.

In three electrode electrochemical cell the working electrode is virtually grounded via an operational amplifier such that the potential of working electrode is very close to  $V = 0V$ . If one needs a potential at the working electrode  $V$  with respect to the reference electrode the reference should have a potential of  $-V$  (since, working is at  $V = 0V$ ). Therefore, a varying potential sometimes referred to as '*control potential*' is added to the actual potential of the reference electrode such a way that with the help of a feed-back loop the potential of the reference electrode eventually approaches to  $-V$ . Fig. 2.3 shows a very simplified diagram of the instrumentation in a three-electrode electrochemical cell set up.

### Cyclic-voltammetry

Cyclic-voltammetry or CV is probably the most popular electrochemical technique to study electrochemistry of solid electrodes. CV is a potentiodynamic electrochemical process where the potential of the working electrode is ramped with respect to the reference electrode. The potential of the working electrode is changed at a constant rate (scan rate). After reaching a peak (set) potential the ramp direction is reversed. This process may continue for various cycles. During the ramping of the

electrode potential, the current flowing between working and counter electrodes is recorded; the plot of this recorded current versus applied potential is called cyclovoltammogram. Other than the study of electrochemical properties and redox reactions of an electrode in a given solution, cyclic-voltammetry may also be used to study kinetics of an electrochemical process from the analyses of cyclovoltammogram recorded at various scan rates.

### **Chronopotentiometry**

Chronopotentiometry (CP) is the most basic constant current electrochemical experiment where the potential is measured as a function of time at a constant current. A zero current chronopotentiometry disconnects the counter electrode and measures the change in open circuit potential with time.

### **Chronoamperometry**

Chronoamperometry is an electrochemical technique in which the potential of the working electrode is pulsed and the resulting current with respect to time is recorded. The recorded current variation with respect to time can itself identify the electrode process taking place. Within the capacitive region the current should vary with time following the equation,  $i \propto e^{-t/RC}$  (with  $R$ , electrolyte resistance and  $C$ , electrode capacitance) whereas when the redox reactions interfere, the diffusion limited faradaic current prevails ( $i \propto t^{-1/2}$ ).

### **Point of zero charge (PZC)**

Point of zero charge (PZC) is a concept describing the condition when the surface charge density of a given electrode surface is zero. Generally PZC is defined in relation to the pH value of the electrolyte, however, here it is defined as the potential applied (in Volts) to make the surface charge of a working electrode zero, for a given electrode/electrolyte combination. Therefore, the point of zero charge can also be used to determine the absolute electrode potential of a certain electrode in a given electrolyte.

### **Open circuit potential (OCP)**

The open circuit potential (OCP) (also referred as the steady-state, the equilibrium or the rest potential) is the potential of the working electrode relative to the reference electrode when no potential or current is being applied to the cell.

#### ***2.1.1.3 Electrolytes***

##### **(a) Liquid electrolytes**

The term electrolytes usually refer to the liquid electrolytes if not otherwise stated. A liquid electrolyte can be defined as a conducting liquid medium usually with a

large ionic and low electronic conductivity. The conductivity comes from dissolved conducting ions in an aqueous or non-aqueous solvent. Table 2.1 summarizes few commonly used non aqueous solvents with their liquid range, dielectric constant, room temperature vapor pressure, room temperature viscosity and stability potential window [Rie87]. As in the present study we are interested in the electrochemical field-effect with negligible chemisorption at the electrode surface, it is very important to use non-adsorptive supporting electrolytes (salts). Generally it has been observed that strong cations (highly electropositive) or strong anions (highly electronegative) show less tendency of chemisorptions at the metal electrode. As an example R. M. Tucceri [Tuc04] has reported that the tendency of anion absorption on gold electrodes decreases from fluoride to iodide  $F^- < HSO_4^- < Cl^- < Br^- < I^-$ .

Table 2.1 Non-aqueous solvent properties [Rie87, Man69]:

Solvents	Liquid range (°C)	Vapor pressure (kPa)	Dielectric constant	Viscosity ( $10^{-3} \text{kg.m}^{-1}\text{s}^{-1}$ )	Stable potential range/V (Pt ref.)*
Propylene carbonate (PC)	-49 to 242	<0.1	64.4	2.5	1.7 to -1.9
Dimethylsulfoxide (DMSO)	19 to 189	0.1	46.7	2.0	0.7 to -1.8
N,N-Dimethylformamide (DMF)	-60 to 153	0.5	36.7	0.8	1.6 to -1.6
Acetonitrile (AC)	-44 to 82	11.8	37.5	0.34	1.8 to -1.5
Ethyl Acetate (EA)	-84 to 77	12.7	6	0.42	**
Tetrahydrofuran (THF)	-108 to 66	26.3	7.6	0.46	**

\* Data for sodium perchlorate ( $\text{NaClO}_4$ ) supporting electrolyte, \*\* Stability potential window data is not found for  $\text{NaClO}_4$  supporting electrolyte

## (b) Solid electrolytes

Solid electrolytes can be divided into three major classes [Bru95]:

- I. Crystalline solid electrolytes (also known as ceramic electrolyte).

II. Glassy solid electrolytes.

III. Polymer electrolytes.

Table 2.2 summarizes the different class of solid electrolytes with active ions and ionic conductivity.

### Crystalline solid electrolytes

This class of electrolytes is often also known as ceramic electrolytes. The ionic conduction occurs by means of ion hopping from one site to another and therefore a partial occupancy is needed for energetically equivalent or near-equivalent positions. Two broad kinds of conduction mechanism can be distinguished - vacancy or interstitial migration. It can also be a co-operative ion migration as opposed to a single ion hopping as in case of Na- $\beta$ -alumina. Typical examples of high conductivity solid electrolytes include Na- $\beta$ -alumina, RbAg<sub>4</sub>I<sub>5</sub>,  $\alpha$ -AgI.

According to the type of conducting ions they can be classified as:

- a. Alkali ion conductor: NASICON (NaZr<sub>2</sub>(PO<sub>4</sub>)<sub>3</sub>), LISICON ( $\gamma$ -Li<sub>2</sub>ZnGeO<sub>4</sub>).
- b. High temperature oxide ion conductor: Yttria stabilized zirconia (YSZ), CeO<sub>2</sub>, ThO<sub>2</sub>, Bi<sub>2</sub>O<sub>3</sub>.
- c. Fluoride conductor: PbF<sub>2</sub>, CaF<sub>2</sub>, SrF<sub>2</sub>, BaF<sub>2</sub>.
- d. Proton Conductor: Hydrated SrCe<sub>0.95</sub>Yb<sub>0.05</sub>O<sub>3-x</sub>H<sub>x</sub>

### Glassy solid electrolytes

These electrolytes are amorphous in nature. Preparation procedures typically include novel techniques like High Energy Ball Milling (HEBM) or Rapid Quenching (RQ). Generally, the particle size of the electrolyte materials varies between 500 nm to 2  $\mu$ m. A further decrease in particle size is not possible. The higher energy supplied to the system in order to decrease the particle size results in crystallization of the glassy particles. Crystallization decreases the conductivity by many orders of magnitude. Li<sub>3</sub>PO<sub>4</sub>-Li<sub>2</sub>S-SiS<sub>2</sub> and Ag<sub>2</sub>S-SiS<sub>2</sub> are two Li and Ag ion conducting glassy solid electrolytes, respectively.



### Polymer electrolytes

Polymer based solid electrolytes are generally classified according to the type of conducting ions and the presence of any additional solvent or supporting electrolyte (inorganic/organic). The different broad classes which can result from this are listed below:

- a. True-polymer electrolyte or polyelectrolyte: Charged groups either anions or cations covalently bonded with a low molecular weight polymer. Mostly it is either cation or anion conductor (NAFION: Na conductor, LIPON: Li conductor).
- b. Polymer-salt complexes: A supporting electrolyte (salt) is dissolved in a polymer. The salt is ionized and provides the conduction. The polymer acts as solvent in this case. In contrast to polyelectrolyte, both cations and anions are mobile here. Examples are  $\text{LiPF}_6$ ,  $\text{LiBF}_4$  in poly-ethylene oxide (PEO) or in polyacrylonitrile (PAN).
- c. Gel-polymer electrolyte: A solvent ( $\text{H}_2\text{O}$ , non-aqueous solvents, ionic liquid) is also dissolved generally in a high molecular weight polymer (PVA, PEO, PVDF). One typical example is PVA+KOH+ $\text{H}_2\text{O}$  gel polymer electrolyte.
- d. Superionic gel-polymer electrolyte: polymer gel electrolytes with nanocrystalline ceramic fillers embedded in the polymeric network. For example,  $\text{ZrO}_2$ ,  $\text{SiO}_2$ ,  $\text{SnO}_2$ ,  $\text{TiO}_2$  nanoparticles are used.

Table 2.2 Ionic conductivity of different classes of solid electrolytes:

Solid Electrolytes			Mobile ion	Ionic conductivity (Scm <sup>-1</sup> )	Temperature (°C)
Group	Subgroup	Electrolyte			
Crystalline electrolyte	Alkali ion conductor	Na-β-alumina [Whi71],	Na <sup>+</sup>	1.4 × 10 <sup>-2</sup>	RT
		RbAg <sub>4</sub> I <sub>5</sub> [Kee76]	Ag <sup>+</sup>	2.5 × 10 <sup>-1</sup>	RT
		NASICON [Goo76]	Na <sup>+</sup>	10 <sup>-1</sup>	300
		LISICON [Bru84]	Li <sup>+</sup>	10 <sup>-1</sup>	300
	Oxide ion conductor	YSZ [Che02]	O <sup>2-</sup>	10 <sup>-1</sup>	1000
		Y-doped Bi <sub>2</sub> O <sub>3</sub> [Tak78]		10 <sup>-2</sup>	500
	Fluoride conductor	PbF <sub>2</sub> [Ben75]	F <sup>-</sup>	10 <sup>-7</sup>	RT
				1	460
	Proton conductor	SrCe <sub>0.95</sub> Yb <sub>0.05</sub> O <sub>3-x</sub> [Iwa86]	H <sup>+</sup>	8 × 10 <sup>-3</sup>	900
		H <sub>3</sub> (PW <sub>12</sub> O <sub>40</sub> ), 29H <sub>2</sub> O [Nak79]		1.7 × 10 <sup>-1</sup>	RT
Glassy electrolyte		B <sub>2</sub> S <sub>3</sub> -Li <sub>2</sub> S-LiI [Wad83]	Li <sup>+</sup>	10 <sup>-3</sup>	RT
		Ag <sub>2</sub> S-SiS <sub>2</sub> [Pen02]	Ag <sup>+</sup>	6.9 × 10 <sup>-2</sup>	RT
Polymer electrolyte	Poly-electrolyte	NAFION [Gan89]	Na <sup>+</sup>	10 <sup>-5</sup>	RT
		LIPON [Ban89]	Li <sup>+</sup>		
	Polymer-salt complexes	LiPF <sub>6</sub> , PEO [Jac89]	Li <sup>+</sup> , PF <sub>6</sub> <sup>-</sup>	2.5 × 10 <sup>-3</sup>	100
	Gel-polymer electrolyte	PVA, KOH, H <sub>2</sub> O [Lew00]	K <sup>+</sup> , OH <sup>-</sup>	10 <sup>-3</sup>	RT
	Superionic gel-polymer electrolyte	PVA, KOH, H <sub>2</sub> O, ZrO <sub>2</sub> [Yan06]	K <sup>+</sup> , OH <sup>-</sup>	2.67 × 10 <sup>-1</sup>	RT

### 2.1.2 Extremely small nanostructures

One important prerequisite to ensure surface charge-induced change in macro-properties in metals or other high conducting materials is the use of extremely small nanostructures. An exceptionally large surface-to-volume ratio of nanostructures with number of surface atoms comparable to the bulk can be achieved with ultra-thin films or with interconnected nanoparticle networks.

#### a) Ultra-thin films:

To grow ultra-thin continuous/percolating metal films on insulating substrate is a challenge itself. For the monolayer by monolayer (Frank-van der Merwe growth mode) growth to occur, the surface energy of the growing film ( $\gamma_f$ ) and the interfacial energy of the film and substrate ( $\gamma_{in}$ ) must be less than or equal to the surface energy of the substrate ( $\gamma_s$ ) [Bau86].

$$\gamma_f + \gamma_{in} \leq \gamma_s \quad (2.3)$$

The condition is easily fulfilled for the growth of A on A (homoepitaxy), in which case  $\gamma_f = \gamma_s$  and  $\gamma_{in} \equiv 0$ , and more generally for films growing on substrates with lattice matching (heteroepitaxy), i.e., zero misfit between growing film and substrate lattice. This results in the strain contribution of the interfacial energy to be zero. However, this condition is difficult to achieve when growing a metal film on an insulating oxide substrate. Therefore, at the early stage of film growth always the three-dimensional island mode (Volmer-Weber growth mode) prevails.

The other parameters which determine the minimum achievable thickness of a continuous film include proper choice of the deposition technique, substrate, substrate temperature, buffer layer etc. Oates *et al.* have reported the percolation threshold ( $t_{\min}$ ) of Ti and Au to be between 2.7 to 3.1 nm and 4 to 4.5 nm, respectively, when grown on silicon oxide at room temperature [Oat04, Oat03]. With the selection of a proper substrate (with a lattice matching for certain growth direction of the metal under consideration) growth of percolating few nanometer thick metal films has been achieved. The substrate dependent variation of percolation threshold for Au thin films has been shown by Lee *et al.* [Lee04]. Substrate temperature may also play a role, while, generally a lower substrate temperature results a smaller value of  $t_{\min}$  [Maa94]. Aging of the films may also be an important issue for the ultra thin films near percolation threshold [Byo03]. However, the choice of a proper substrate and/or a selection of a correct buffer layer may be the key to achieve few monolayers (ML) thick continuous film. A 2.5 ML thick continuous gold film on Si [Kim01] and 2-4 nm thick FePt or FePd films on MgO substrate with Pt or Pd buffer layer have been reported in the literature [Wei07]. However, it may be noted that for the measurement of surface charged induced electron transport in ultra-thin metallic film the possibility of using a metallic buffer layer (with preferred lattice matching to obtain few monolayer thick continuous film) is right away excluded. During the transport measurement it would not be possible to separate the electron transport through the film of interest and the (metallic) buffer layer. As mentioned previously, the fabrication of a few monolayer thick metallic films is of high

importance in the present study, because only for an ultra-thin film the induced surface charge would be comparable to the number of charge carriers present in the film. Thus, the measurement of any changes in physical property which depends on the number of free carriers in a system would also be possible. Fig. 2.4 shows schematically the charged surface of a few-monolayer thick metal film immersed in an electrolyte.

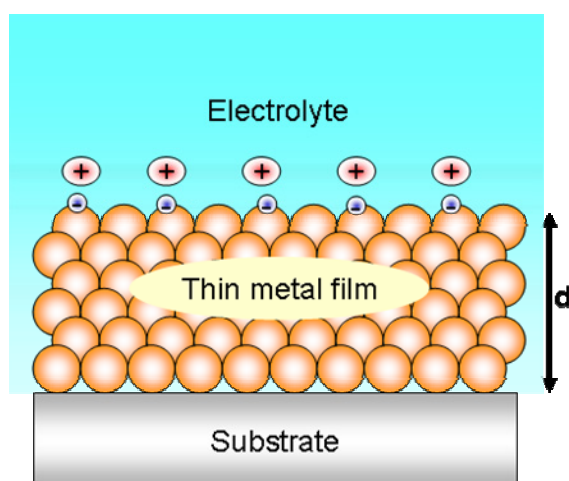


*Figure 2.4 Schematic representation of the charged surface of a thin metal film inside an electrolyte*

- b) Interconnected nanoparticles synthesized via inert gas condensation or spin coating from nanoparticle dispersion:

Nanoparticles of metals or alloys (with average particle size of a few nanometers) can be prepared by inert gas condensation (IGC) technique, thermally evaporating the metal or the master alloy [Bir84]. The obtained loose agglomerate is usually compressed slightly to obtain a nanoporous disc [Wei03]. The loosely compressed disc consists of interconnected nanoparticle network and nanometer sized pores which are easily accessible by the electrolyte.

One of the simpler ways to obtain a percolating (interconnected) nanoparticulate film is spin coating of nanoparticle dispersion on a substrate. Fig. 2.5 shows such a film immersed in an electrolyte.

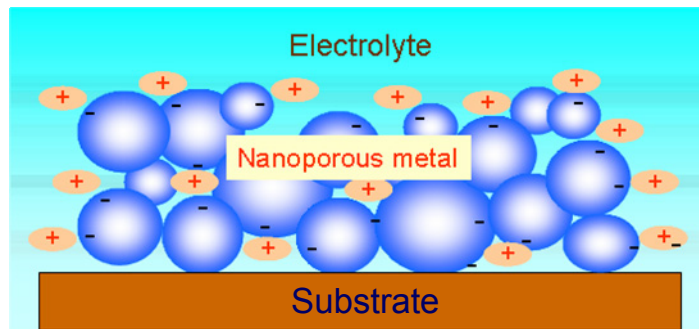


Figure 2.5 Schematic representation of the charged surface of a nanoporous film/aggregate immersed in an electrolyte

c) Nanoporous network of noble metal by de-alloying:

De-alloying is a process of leaching which refers to the selective removal of electrochemically more active metal from a master alloy. Typical examples of de-alloying could be dezincification (dissolving zinc from brass to get a porous copper structure), decarburization (graphitic corrosion from grey cast iron) or corroding silver out from a silver-gold alloy. The resultant nanoporous, spongy network normally composed almost entirely of the electrochemically more noble metal or alloy. Although the physics behind the formation of nanopores is not entirely clear [For79], it has been observed experimentally that the ligament (made of the nobler un-dissolved metal) and pore size essentially depends on the applied de-alloying potential: the higher the potential the finer the resultant microstructure is [Par06, Erl04].

### ***2.1.3 Modification of the macro-properties of nanostructures with external field***

As mentioned earlier there are various physical properties which can be tuned reversibly through a deviation from charge neutrality by an external field.

a) Electrical properties:

The most renowned example of controlled enhancement or depletion of the local charge carrier density by an external applied field is '*Junction Field-Effect Transistor (JFET)*' [Sze81]. The device principle is to modulate the current flowing through a semiconductor channel by an external field applied by a gate oxide dielectric. In case of a n-channel JFET an enhancement or depletion of channel conductance (current through the semiconductor) is possible by a positive or negative gate bias, respectively. Therefore, it might also be possible to vary the conductivity of a pure metal or a near metallic system with higher local electric field at the surface. To tune the conductance of a

metallic system a large surface-to-volume ratio of the nanostructures and an electrochemical gating was used. A reversible change in resistance of  $\pm 4\%$  of a nanoporous compact of Pt nanoparticles with an aqueous electrolytic gating has been reported recently (Fig. 2.6) [Sag06]. Similarly change in resistance of a few percent has also been observed recently in de-alloyed nanoporous gold [Mis08] and for AuFe nanoparticles [Ban07].

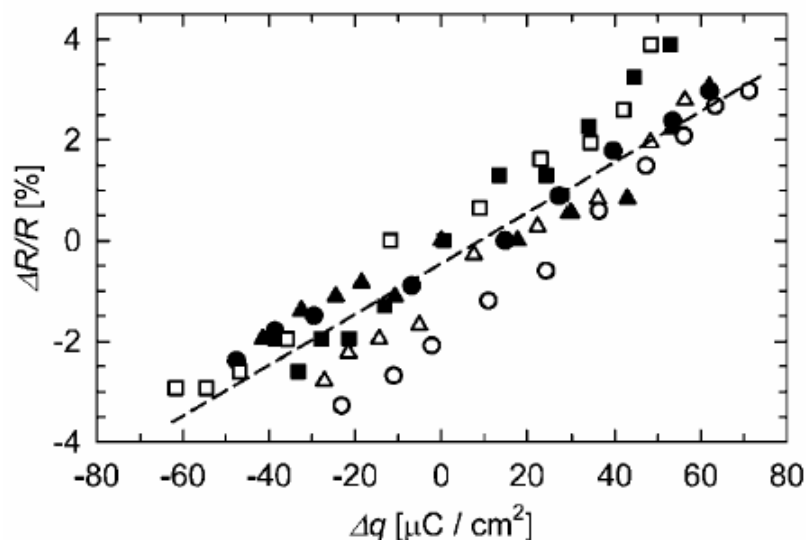


Figure 2.6 Relative variation  $\Delta R / R$  of the electric resistance of porous nanocrystalline Pt with the imposed specific charge density  $\Delta q$  using KCl as electrolyte with different pH values; (■, □ refers to pH 12); (●, ○ refers to pH 2); (▲, △ refers to pH 7). Filled and empty symbols refer to charging in positive and negative direction, respectively [Sag06].

#### b) Mechanical properties:

Field-induced reversible variation in length of a material has earlier been observed widely for piezoelectrics [Viv08, Yag06] and conducting polymers [Sme03, Fre07], which have found widespread applications in sensors [Wol07] and actuators [Pon05]. However, similar field-induced reversible strain in a metallic system has not been demonstrated until Weissmüller *et al.* [Wei03]. The piezoelectric response of the order of 0.1% or above was observed for a nanoporous platinum compact when surface charge was applied with an aqueous solution of KOH. The strain was seen to vary in phase with the applied potential. Since the hydrostatic pressure of the liquid electrolyte cannot produce strain in the system, the observed strain was thought to be an effect of pressure produced by the surface charge. To verify this, in-situ measurements of X-ray diffraction studies of nanoporous platinum were carried out. A reversible variation of lattice parameter by 0.14% was observed. Recently, the same group has shown 0.24% linear strain in

dealloyed nanoporous gold [Jin08]. Although the *electrocapillarity*, i.e., strain caused by an external voltage in an electrode due to electric double layer, has been well known since nineteenth century, this was the first demonstration of large strain in a pure metallic system. Fig. 2.7 shows the length change of a 1 mm thick nanoporous gold sample measured in the dilatometer during a series of potential jumps from -0.2 to 1.0 V [Kra04]. It has also been shown that a large macroscopic bending of a bimetallic (metal-nanoporous metal) cantilever of the order of several millimeters is possible with the same basic principle [Kra04].

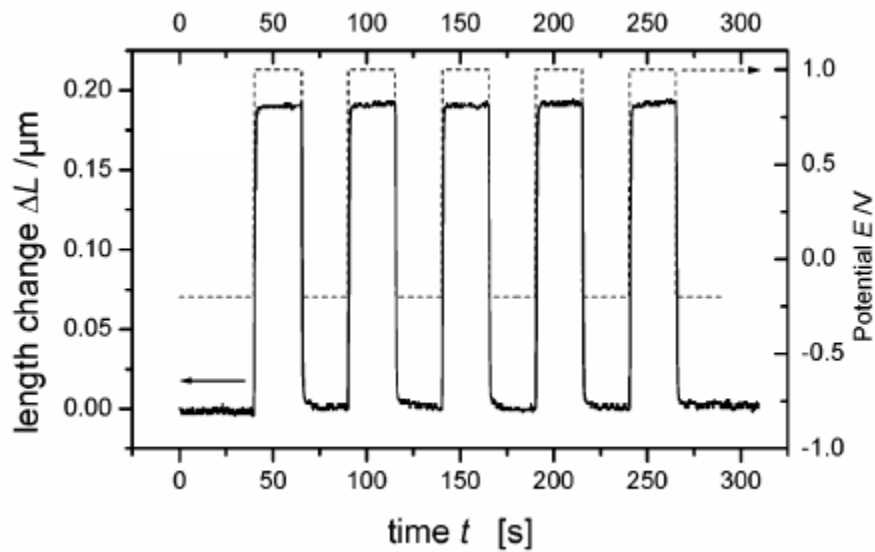


Figure 2.7 Length change ( $\Delta L$ ) of the 1 mm thick nanoporous gold sample in 50 mM sulfuric acid, measured in the dilatometer during a series of potential jumps from -0.2 to 1.0 V and back (dashed line: potential) [Kra04].

c) Magnetic properties:

Magnetization in 3-D transition metals arises from partly filled d-band. It was proposed [Gle01a, Gle01b] that an external field can reversibly change the d-band state of a ferro- or paramagnetic metal or alloy resulting in a change in magnetization. Indeed, a 1% variation in magnetic susceptibility is observed for paramagnetic nanoporous Pd upon electrochemical charging [Dri06]. The result has been explained on the basis of a core-shell model, which implies that the observed susceptibility is the sum of the susceptibilities of the surface atoms affected by the surface charge and that of unaffected core atoms. An effect of pressure on the variation of susceptibility was also considered. It has been observed with X-ray absorption near edge spectroscopy (XANES) that a significant change in d-band occupation of platinum occurs when the Pt nanoparticles-electrolyte interface are electrochemically charged [Muk95]. Recently, a charge induced

variation of coercivity and magnetic anisotropy was reported (Fig. 2.8) for the ultra-thin Pt-Fe and Pd-Fe films [Wei07]. The later can be taken as a more convincing proof of the change in d-band filling in a ferromagnet by an external electrostatic field.

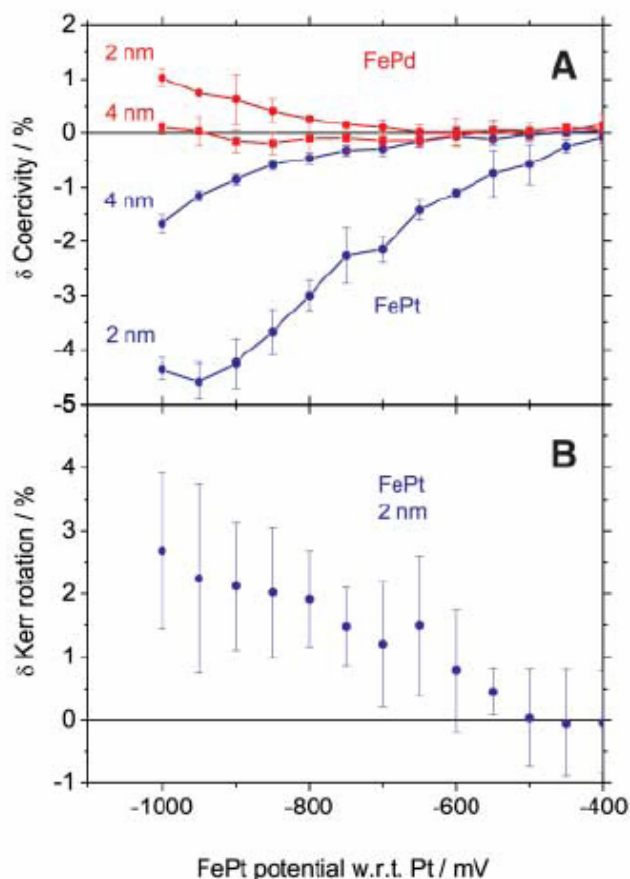


Figure 2.8 (A) Change of the film coercivity for FePt and FePd thin films with respect to an external voltage; (B) percentage change in the Kerr rotation of the 2-nm thick FePt film with respect to the value at -400 mV [Wei07].

## 2.2 CHARACTERIZATION TOOLS

### 2.2.1 X-ray reflectometry (XRR)

X-ray reflectometry (XRR) is carried out through  $\theta - 2\theta$  scan like X-ray diffraction, however, is limited only to angles  $0 < \theta < 10^\circ$ . When X-rays strike a surface with a small glancing angle they can reflect from the surface. XRR exploits the different reflectivity of X-ray depending on the surface roughness and thickness of the film covering the surface by measuring the intensity of X-rays reflected from a surface as a function of the incident angle. First experiment on total reflection of X-rays from flat



and smooth surfaces was reported by Compton [Com23] in 1923. In 1931, H. Kiessig found oscillations of the reflected X-ray intensity of a thin layer on a substrate [Kie31]. The position of these oscillations is related to the thickness of the thin film and nowadays these oscillations are called Kiessig-fringes. In 1963, Yoneda [Yon63] reported the intensity modulation in the angular distribution of X-ray diffuse scattering, which was afterward named *Yoneda wings*.

The refractive index ( $n$ ) of a material for the X-rays is a complex quantity which takes into account amplitude damping and phase shift due to dispersion ( $\delta$ ) and absorption effects ( $\beta$ ).

$$n = 1 - \delta - i\beta \quad (2.4)$$

Here the dispersive correction,  $\delta$ , is associated with the real part of the average atomic scattering factor as [Boe95]

$$\delta = \frac{N_A r_e \lambda^2 \rho f'}{2\pi M} \quad (2.5)$$

where,  $N_A$  is Avogadro's number,  $r_e$  is the classical electron radius,  $\lambda$  is the wavelength of incident X-ray,  $\rho$  is the density of the material,  $f'$  is the real part of the atomic scattering factor,  $M$  is the atomic mass.

The absorption correction,  $\beta$ , is proportional to the imaginary part of atomic scattering factor, however, can also be expressed in terms of the linear absorption coefficient  $\mu$  [Boe95].

$$\beta = \frac{\lambda \rho \mu}{4\pi} \quad (2.6)$$

These two parameters are very small quantities ( $< 10^{-4}$ – $10^{-8}$ ) [Sto99]. For X-rays, any material is optically less dense (i.e.,  $n < 1$ ) than vacuum ( $n = 1$ ). Consequently, total reflection of X-rays entering the medium from vacuum side will occur for incident angles smaller than a critical angle  $\theta_c$ . The critical angle is defined as

$$\theta_c = \sqrt{2\delta} \quad (2.7)$$

However, it may be important to note that for certain combination of elements and energies of X-ray radiation, the dispersion term,  $\delta$ , of the refraction index is negative, and total reflection cannot be observed in these cases [Sto99]. Combining equation 2.5 and 2.7 one can obtain

$$\theta_c = \sqrt{2\delta} = \sqrt{\frac{N_A r_e \lambda^2 \rho f'}{\pi M}} \quad (2.8)$$

Therefore, it is clear that the angle of total reflection is dependent on material density, the denser the material, the lower the angle of total reflection (e.g.,  $\theta_c(\text{Cu}) = 0.39$  and  $\theta_c(\text{Al}) = 0.2$ ). XRR can provide informations on surface and interface roughness and thickness of the thin films. If the thickness is known from other techniques (e.g., cross-section scanning or transmission electron microscopy) the density of the material can also be obtained.

### 2.2.2 Grazing incidence X-ray diffraction (GIXRD)

Grazing incidence X-ray diffraction (GIXRD) uses small fixed incident angles for the incoming X-ray so that diffraction can be made surface sensitive. For ultra-thin film sample with decrease in film thickness it becomes increasingly difficult to use Bragg-Brentano ( $\theta-2\theta$ ) geometry and hence GIXRD is employed. Here, the sample is illuminated by the incident beam at fixed angle of few degrees and the detector is scanned to obtain Bragg-condition satisfied at different angles. Thus the scattering geometry in grazing incidence actually combines the Bragg condition with the conditions for X-ray total external reflection from crystal surfaces. This provides superior characterization compared to the other diffraction schemes in the studies of thin surface layers, since the penetration depth of X-rays inside the sample surface is reduced by three orders of magnitude, typically from 1-10  $\mu\text{m}$  to 1-10 nm. Therefore, Bragg reflections are only coming from the surface structure [Boe95, Sto99].

For grain size analysis from X-ray diffractogram several models can be followed. The measured intensity first of all is a convolution of structural and instrumental counterpart:

$$I(2\theta)_m = I(2\theta)_s * I(2\theta)_i \quad (2.9)$$

Depending on the shape of the reflection the measured integral width ( $\beta_m$ ) can be [Cul59]:

Gaussian: 
$$\beta_m^2 = \beta_s^2 + \beta_i^2 \quad (2.10)$$

Lorentzian: 
$$\beta_m = \beta_s + \beta_i \quad (2.11)$$

where,  $\beta_s$  and  $\beta_i$  are the structural and instrumental broadening respectively. After the correction made for the instrumental broadening, the grain size can be obtained using classical Scherrer equation [Cul59]:

$$\beta_s = \frac{k\lambda}{t \cos \theta} \quad (2.12)$$

where,  $k$  is the form factor,  $t$  is the average primary particle size,  $\theta$  is the diffraction angle and  $\lambda$  is the wavelength of the incident X-ray. Scherrer equation is valid only in absence of significant microstrain. In presence of large microstrain Williamson-Hall equation should be used can also estimate microstrain along with the average grain size. Fitting the complete diffraction pattern with Warren-Averbach method it is possible to get a grain size distribution profile rather than the average grain size in earlier methods.

### ***2.2.3 Transmission electron microscopy (TEM)***

The transmission electron microscope (TEM) [Wil96] was first proposed and demonstrated by Max Knoll and Ernst Ruska in 1932. TEM operates with the same basic principles as the light microscope but uses electrons instead of light. TEM uses electrons as “light source” with much lower wavelength making it possible to get a resolution over thousand times better than with a light microscope. In TEM a beam of electrons is transmitted through an ultra thin specimen (typically less than 100 nm) and interact with the specimen as they pass. An image is formed from this interaction of the electrons transmitted through the specimen, which is magnified and focused by an objective lens and onto an imaging device, such as a fluorescent screen, on a layer of photographic film, or detected by a sensor such as a CCD camera. The image contrast is therefore the result of the different spatial intensity of the transmitted beam on the image plane. Developments after the initial invention have made TEM a versatile tool today. Besides conventional transmission electron microscopy it can be used as high resolution transmission electron microscopy (HRTEM), analytical electron microscopy, Energy filtered transmission electron microscopy (EFTEM), Scanning transmission electron microscopy (STEM) etc. TEM tomography [Fra92] on the other hand can be defined as the three-dimensional imaging technique using the transmission electron microscope. This is a three dimensional reconstruction of an object generated from the two dimensional TEM images. The sample normally is rotated with small angular step and the 2-d images are collected which are later used to reconstruct 3-d image using different simulation package.

### ***2.2.4 Atomic force microscopy (AFM)***

Gerd Binnig, Kelvin Quate and Christoph Gerber invented atomic force microscopy (AFM) in 1986. AFM is a method of surface characterization which measures the surface topography of almost any type of surface, including polymers, ceramics, composites, glass, and biological samples, making the technique significantly important in the fields of materials science, chemistry, biology, physics, and the specialized field of semiconductors [Mey92, Gie03]. It is a high-resolution type of scanning probe microscope, with demonstrated resolution of fractions of a nanometer, more than 1000 times better than the optical diffraction limit. The AFM works by scanning a fine ceramic or semiconductor tip (radius 20 nm) over a surface using a feedback mechanism that measures surface–tip interactions on the scale of nanoNewtons (nN). Variations in the tip height are recorded while the tip is scanned repeatedly across the sample, producing a topographic image of the surface. Piezoelectric elements facilitate tiny but accurate and precise movements of the tip which is positioned at the end of a cantilever beam. As the tip is repelled by or attracted to the surface, the cantilever beam deflects. The magnitude of the deflection is captured by a laser that reflects at an oblique angle from the very end of the cantilever. A plot of the laser deflection versus tip position on the sample surface provides the topography of the

surface. Atomic force microscopy can also be used to manipulate matter at the nanoscale. The basic principle of AFM also led to the creation of a variety of other scanning probe microscopes (SPM), such as the magnetic force microscope (MFM), the dipping force microscope (DFM), the friction force microscope (FFM), and the electrostatic-force microscope (EFM). By these new developments the field became further subdivided. Concurrently, there is also a unifying tendency to combine different methods such as STM/AFM, AFM/MFM, AFM/FFM etc.

### ***2.2.5 Scanning tunneling microscopy and spectroscopy (STM, STS)***

Scanning tunneling microscopy (STM) was invented by Gerd Binnig and Heinrich Rohrer at IBM Zürich in 1981. STM is a powerful technique for viewing surfaces at the atomic resolution in ultra-high vacuum, moderate vacuum, different gases including air at atmospheric pressure, and liquids of various kind, non-aqueous solvents, water, liquid nitrogen and even conducting solutions [Han87, Bes96]. The STM is based on the concept of quantum tunneling. When a conducting tip is brought very near to a metallic or semiconducting surface, a bias between the two can allow electrons to tunnel through the vacuum between them. A piezo-electric scanner is used to accurately position an atomically sharp metallic tip above a sample. Changing the position in the lateral (x,y) plane allows to scan continuously across the sample surface and changing the vertical (z) position allows to maintain the desired tip-sample distance. Variations in current as the probe passes over the surface are translated into an image. For low voltages, the tunneling current is a function of the local density of states (LDOS) at the Fermi level,  $E_F$ , of the sample. The exponential dependence of tunneling current on the tip to sample distance results in a high vertical resolution. For STM, good resolution is considered to be 0.1 nm lateral resolution and 0.01 nm depth resolution. It is very important to remember that the image cannot just be interpreted as a topographic map as the tunneling current is influenced by the lateral and vertical variation of the electronic state density at the surface. STM is a challenging technique, as it requires extremely clean surfaces and sharp tips. The STM can be used not only in ultra high vacuum but also in air and various other liquid or gas ambient, and at temperatures ranging from near 100 milliKelvin to a few hundred degree Celsius.

***Scanning tunneling spectroscopy (STS)*** studies the local electronic structure of a sample surface. It is a powerful experimental technique to probe the local density of electronic states (LDOS) and band gap of materials at the atomic scale. STS records current-voltage ( $I-V$ ) curves, however, they can be obtained in several ways: (a) taking “topographic” (constant-current) images using different bias voltages and comparing them; (b) taking current (constant-height) images at different heights and comparing them; (c) disabling the feedback loop to position the tip over a certain feature at a fixed height and ramping of the bias voltage while recording the tunneling current. These current vs. voltage ( $I-V$ ) curves characterize the electronic states of that specific (x,y) location on the sample surface. STS can be set up to collect  $I-V$  curves at every point

in a data set, providing a three-dimensional map of electronic structure. One can obtain  $dI/dV$  (conductance) or  $dI/dz$  (work function) vs.  $V$  curves with a lock-in amplifier. Since the tunneling current in a scanning tunneling microscope only flows in a region with diameter  $\sim 5\text{\AA}$ , STS is unique in comparison with other surface spectroscopic techniques, which usually average over a larger surface area.

## CHAPTER TWO

## Chapter 3

# Reversible tuning of resistance of thin gold films

### 3.1 BACKGROUND

A reversible change in material properties with an external electric field is well known for semiconductors [Sze81], conducting polymers [Kel04] and carbon nanotubes [Pop04]. However, in case of metals due to large number of free charge carriers, it is unlikely to observe any measurable change of physical properties as a function of applied electric field. The mean penetration depth of an external field,  $\delta$ , has been calculated to be nearly independent to the applied surface charge and for a gold surface it varies between 0.25 to 0.3 nm, i.e. less than a monolayer [Kem85]. Consequently, in order to obtain a measurable change in overall properties of a metal such as gold, upon external applied field/surface charge, the surface-to-volume ratio should be adequately large. This is because a large surface-to volume ratio relates to a high screened volume (screened volume = screening depth in the order of one monolayer  $\times$  surface area), which is then comparable to the total volume of the sample. Indeed, reversible change in physical properties as a function of applied charge has been observed for the nanostructured pure metals that have a high density of surfaces/interfaces [Wei03, Sag06]. The term *tuneable properties* has been proposed in order to express the physical properties of metals that can be modulated reversibly by application of an external voltage, [Gle01a, Gle01b].

In this chapter, surface charge-induced reversible change in resistance of thin gold films (film thickness of several nanometers) is shown and discussed. Sagmeister *et al.* [Sag06] have shown recently that a reversible change in resistance by  $\pm 4\%$  is possible for nanoporous compacts prepared from Pt black with a particle diameter of 10 nm. The first attempt to change the resistance of a metal electrochemically was made by Anderson and Hansen [And73a, And73b] in 1973 using a thin gold film in an aqueous  $\text{Na}_2\text{SO}_4$  solution. The experiments, however, yielded only 0.4% changes in resistance. A

contradictory result was obtained by Tucceri and Posadas [Tuc85, Tuc90, Tuc04], who observed a non-linear response of  $\Delta R/R$  vs. charge for a gold film in 0.02 M aqueous solution of  $K_2SO_4$  and concluded that the change in resistance arise from the specific adsorption at the surface. It may be noted that all these previous works [Sag06, Ban07, And73a, And73b] were interpreted considering a change of the charge carrier density upon charging. However, it was observed that such a change in carrier concentration upon charging cannot explain the total observed effect [Sag06]. Therefore, it can be concluded from the previous studies that the origin of the resistance change upon applied electrolytic surface charge is not completely understood. There are controversial results with the linearity of  $\Delta R$  with respect to the applied potential and its relation to the possibility of surface adsorption of ions causing the non-linearity [Tuc85]. Surprisingly, it has never before been considered in depth that a part of the change in resistance may also result from a change in carrier mobility/scattering cross-section of the charge carriers. However, a change in surface scattering can be expected with a large surface charge applied to a metal surface. To investigate this hypothesis, thin gold films with well defined geometry are used as a model system. Based on the results, a new model is proposed in order to consider the change in scattering behavior of the electrons with respect to surface charge density.

In order to apply a large electrostatic field at the metal surface, a surface inactive non-aqueous electrolyte is used. To ensure that the majority of the effect arises from double layer charging (electron/ion electrical dipole without electron transfer across the interface) and the chemisorption is insignificant a suitable potential window was selected by using a very slow cyclo-voltammetry measurement. To differentiate the double layer capacitive charging from chemical effects (redox reactions) at the interface the term *electrostatic doping* can be proposed. The electrostatic doping is a surface phenomenon which results in a creation of an electric double layer with controllable charge carrier density at the metal-electrolyte interface. In the electrostatic doping the applied field/surface charge density is therefore related to the capacitance of the electric double layer formed at the interface, hence, a solvent with high dielectric constant (Propylene Carbonate,  $\epsilon_{PC} = 65$ ) should be selected. A high surface-to-volume ratio of ultra-thin films is used to maximize the surface charge per unit volume.

## 3.2. EXPERIMENTAL

Thin gold films were fabricated with dc magnetron sputtering on thermally oxidized silicon (100) wafers without any buffer layer. The silicon substrates were used as-received without further cleaning of the substrates. The sputtering of thin films was performed at room temperature. The sputtering power was 29 Watt, for a 1.25 inch sputter target. The target-substrate distance was 7.5 cm. The process pressure was  $5 \times 10^{-3}$  mbar, while the base pressure was  $3.5 \times 10^{-7}$  mbar. The thicknesses of the films determined by X-ray total reflectometry were 7, 9.3 and 11.6 nm. Two shadow masks were used to obtain the thin gold film (7-11.6 nm) and the thicker gold contact leads (50



nm). The thin film samples had a shape of a square of 10×10 mm with four leads at the four corners for resistance measurements (Fig. 3.1). The contact lead at the middle of the square connects the working electrode of the potentiostat. It is placed exactly at the middle of the corner contacts to avoid transient effects (Tuc04).

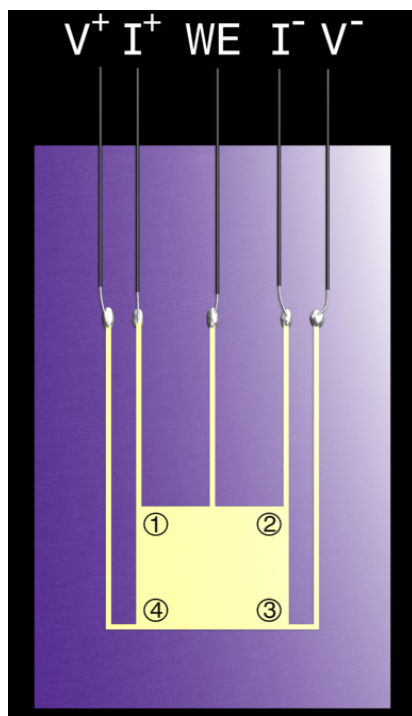


Figure 3.1 Schematic representation of the sample geometry

### 3.3. RESULTS

#### 3.3.1 Electrochemical measurements

Electrochemical measurements were carried out with an *Autolab potentiostat PGSTAT 302* equipment, in a conventional three-electrode cell. The complete experimental setup is shown in Fig. 3.2. A solution of 0.1 molar sodium perchlorate ( $\text{NaClO}_4$ ) (Sigma-Aldrich) in propylene carbonate (Merck) was used as an electrolyte. Pure (99.995%) Pt wire (Chempur GmbH) was used as a pseudo-reference electrode. To carry out the measurement of the surface charge-induced variation in electrical resistance, primarily it is necessary to select a potential window with negligible surface-adsorption. The selection of this appropriate potential range was then performed with very slow ( $5 \times 10^{-4} \text{ Vs}^{-1}$ ) cyclo-voltammetry.

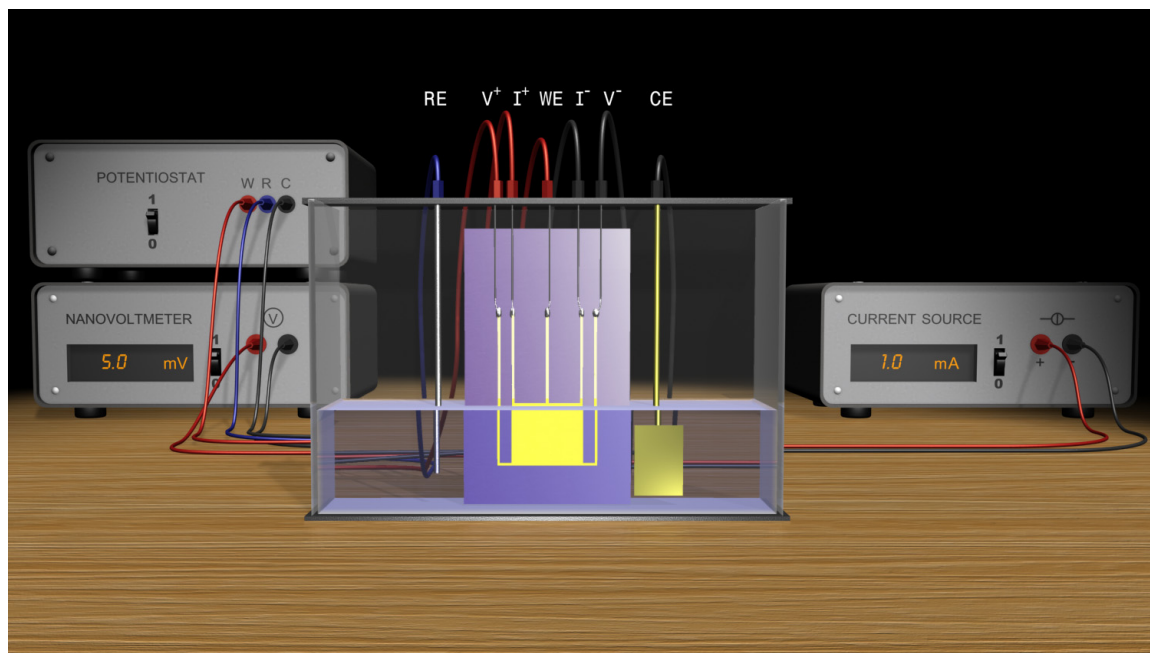


Figure 3.2 Schematic representation of the experimental setup

The open circuit potential (OCP) of the gold thin film electrodes were measured by zero current chronopotentiometry. The OCP was observed close to -100 mV with respect to the reference electrode. Therefore, during the measurement of resistance modulation the potential was stabilized at OCP for few minutes and then cyclovoltammograms were initiated from there to minimize sudden current jump (charge-offset).

Fig. 3.3 shows the cyclovoltammograms recorded at the sweep rate of  $10^{-2} \text{ Vs}^{-1}$  and  $5 \times 10^{-4} \text{ Vs}^{-1}$ , respectively, with the potential varied between a predominantly adsorption-free potential window of 500 mV (-250 mV to +250 mV). The charge accumulated on the film surface was calculated by integrating the charging current. The resistance variation was also measured with potential pulse chronoamperometry. In this case the potential of the working electrode was pulsed with respect to the reference electrode at a step size of 100 mV and the holding time at each potential was 10 minutes. This procedure is referred in the present study as the static mode of surface charging. In this case a sufficiently large time (10 minutes) was allowed to achieve a complete charging of the sample surface.

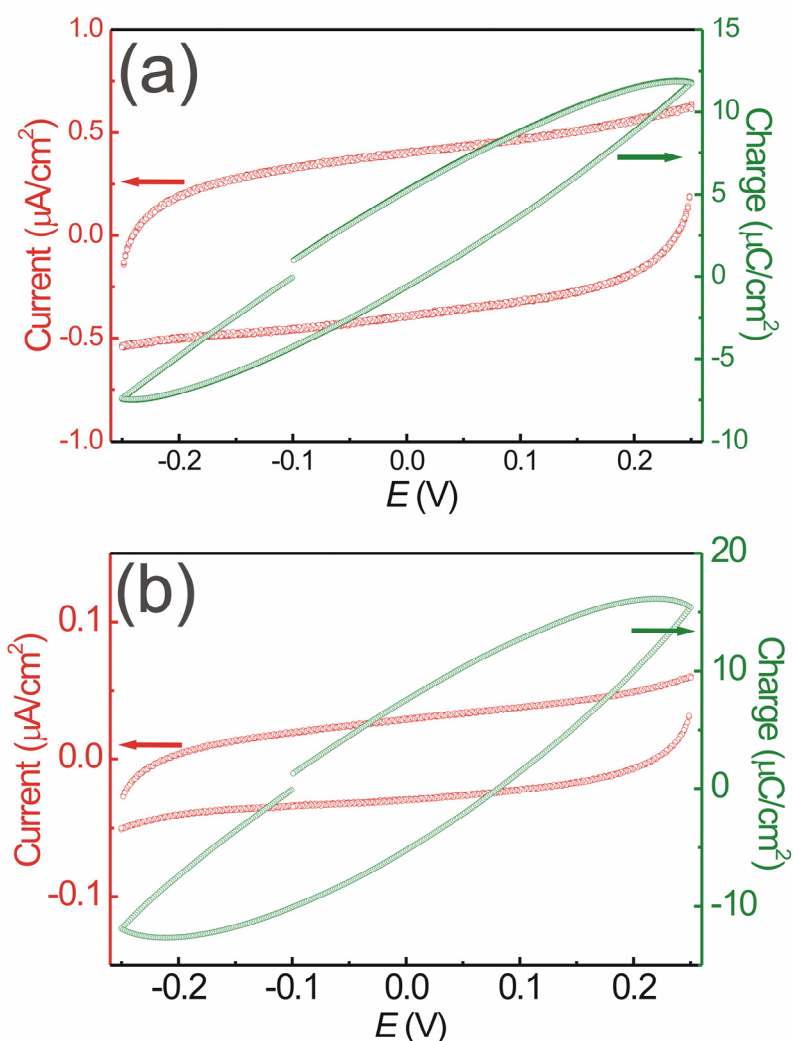


Figure 3.3 Cyclic voltammogram of 7 nm Au film with the scan rate of 10 mV/s, (a) and 0.5 mV/s, (b) in 0.1 M  $\text{NaClO}_4$  in propylene carbonate with the calculated specific charge density

### 3.3.2 Surface charge-induced electrical transport

A Keithley 6221 AC and DC current source and a Keithley 2182A nanovoltmeter were used for the four probe resistance measurements. All resistance measurements were done following the van der Pauw method [Pau58a]. As pointed out earlier, the middle contact of the thin film was attached to the working electrode of the potentiostat to carry out the electrochemical measurements (voltammetry and chronoamperometry). At the same time a constant current of 1 mA was passed through one edge of the sample (for instance,  $I_{12}$ ) and the voltage drop was recorded across the opposite edge (in that case,  $V_{43}$ ) to calculate the sheet resistance (Fig. 3.1). The original van der Pauw equation to calculate the sheet resistance is,

$$e^{-\pi R_A/R_S} + e^{-\pi R_B/R_S} = 1 \quad (3.1)$$

where,  $R_S$  is the sheet resistance, and  $R_A = \frac{V_{43}}{I_{12}}$ ,  $R_B = \frac{V_{23}}{I_{14}}$ .

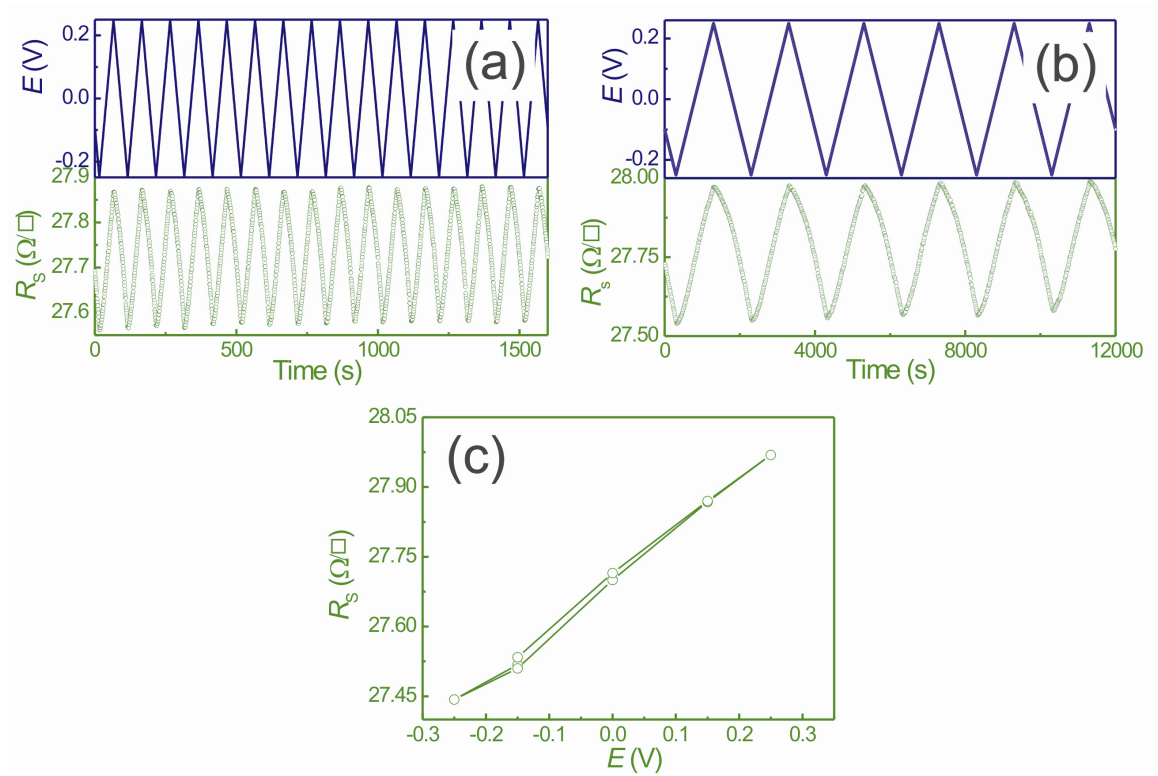


Figure 3.4 Change in the sheet resistance with respect to applied potential for the 7 nm Au film for a scan rate of 10 mV/s (a), 0.5 mV/s (b) and 100 mV potential pulses (c), respectively

In our case, during the dynamic measurement (i.e., with ramping the potential of the thin film with respect to the reference electrode continuously through typical cyclic voltammetric scans) the resistance was measured in one configuration only; let us call it  $R_A$ . In the present study, the good geometrical symmetry of the films assures that  $R_A = R_B$ . Thereby, the sheet resistance of the samples can be calculated as [Pau58b],

$$R_S = \frac{\pi R_A}{\ln 2} \quad (3.2)$$

Fig. 3.4-Fig. 3.6 show the resistance modulation observed for different thickness gold thin films. Fig. 3.7 summarizes the observed effect. It can be noticed that the change in sheet resistance decreases with an increase in film thickness from 7 nm to 11.6 nm.

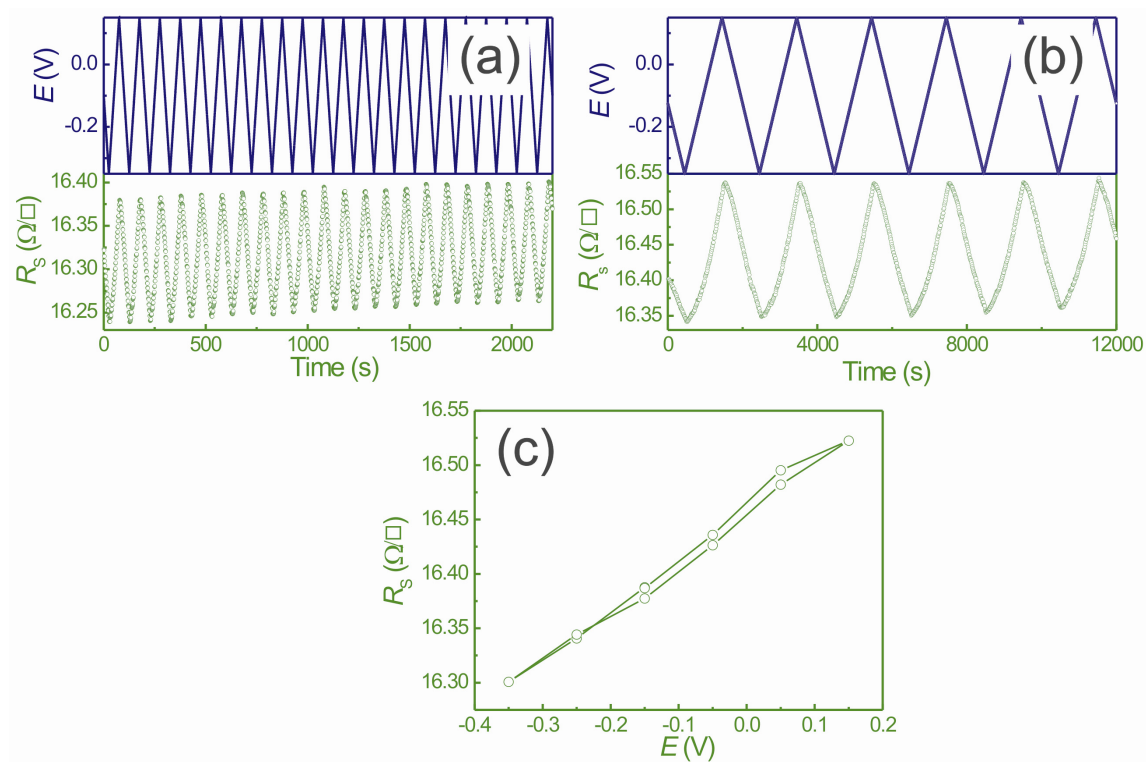


Figure 3.5 Change in the sheet resistance with respect to applied potential for the 9.3 nm Au film for a scan rate of 10 mV/s (a), 0.5 mV/s (b) and 100 mV potential pulses (c), respectively

This decrease in effect-size is rather obvious as with an increase in film thickness the surface-to-volume ratio decreases, in turn decreasing the effect of external charge/electrostatic doping. It can also be observed from Fig. 3.7, that the effect increases with a decrease in frequency of potential sweep. For example, an increase in effect-size from 1.06%, 1.49% to 1.88% was observed for the thinnest (7 nm) film when the potential sweep rate was changed from  $10^{-2}$  Vs $^{-1}$ ,  $5 \times 10^{-4}$  Vs $^{-1}$  and to the static charging, respectively. This increase in effect size may result either from a more complete (capacitive) charging with a decrease in the rate of potential sweep or due to a chemical adsorptions at the sample surface getting more pronounced with the slower scan rate.

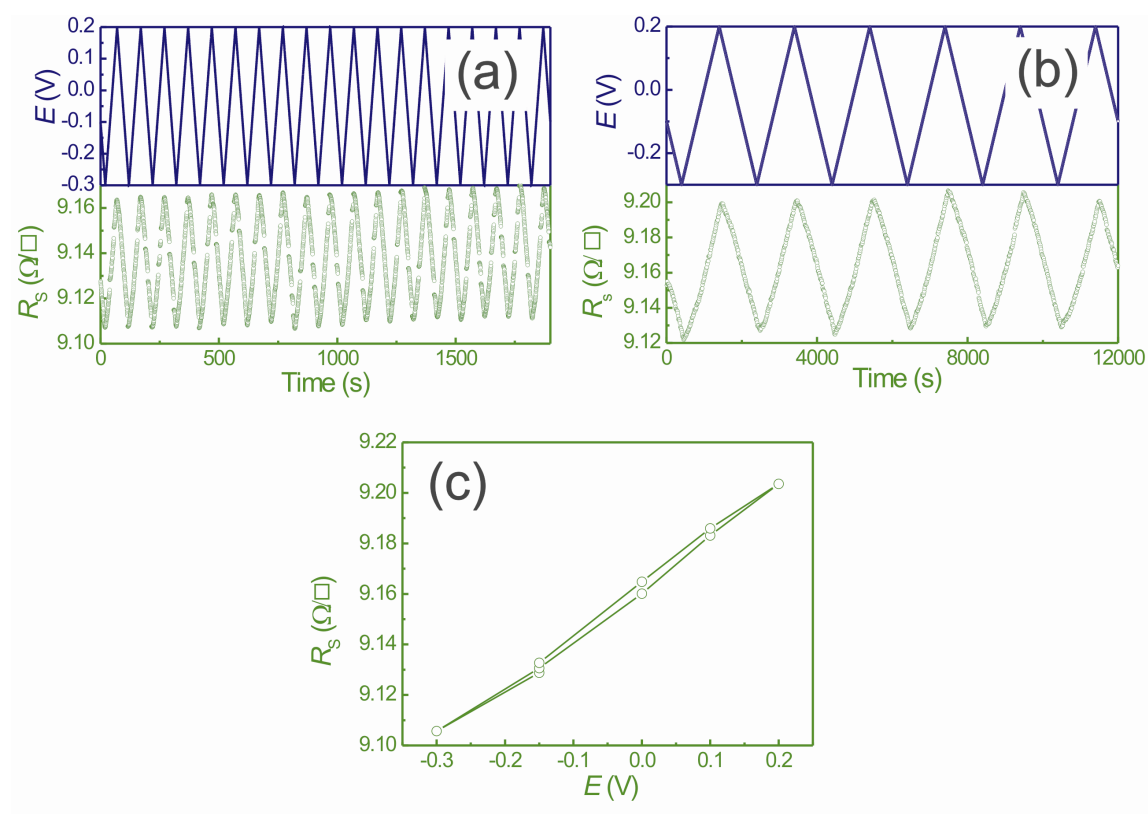


Figure 3.6 Change in the sheet resistance with respect to applied potential for the 11.6 nm Au film for a scan rate of 10 mV/s (a), 0.5 mV/s (b) and 100 mV potential pulses (c), respectively

The first reasoning is believed to be more likely in this case; because, (i) the cyclic voltammograms with different scan rates (Fig. 3.3) result in different charge density at the surface keeping exactly the same ratio as the ratio observed in effect size, (ii) a very small window of 150 mV near the open circuit potential (OCP) also shows an increase in effect-size with decrease in scan speed. The ratio of effect-size with the change in scan rates is still the same for these smaller potential windows.

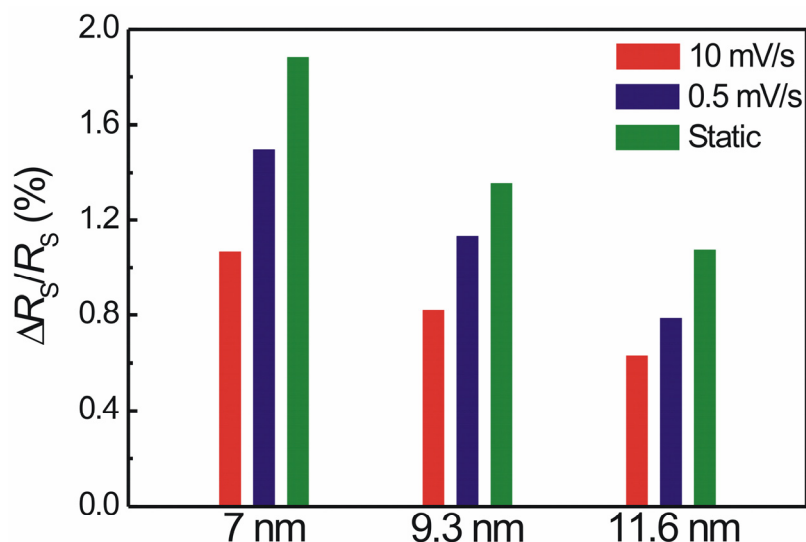


Figure 3.7 Comparison of the change in sheet resistance of Au films with different thickness and scan rates. For any individual film the increase in the effect size was observed with a decrease in the scan rate from 10 mV/s to 0.5 mV/s to static charging, respectively

With the involvement of the specific adsorption a smaller window (150 mV) (which was very close to an ideal capacitive region, showed nearly constant current with potential sweep) should show lesser extent of adsorption than a bigger one (500 mV). Therefore, it can be considered as a logical argument that the increase in effect-size with a decrease in scan rate is primarily due to the insufficient charging at the faster potential sweep.

### 3.3.3 Atomic force microscopy

The grain size and surface morphology of thin gold films were determined using Atomic Force Microscopy (AFM) with a *Digital Instrument Multimode IIIA* AFM analyzer. All the images were taken in intermittent contact mode or tapping mode. Fig. 3.8 shows a 5×5 μm section of 2.3 nm (according to the calibrated sputter rate) thin film. As was expected 3D growth of isolated islands was observed for ultra-thin film thickness. The films were sputtered at room temperature (RT), however, the atomic mobility of gold at RT is large enough to encourage Oswald ripening; resulting large island sizes of 80-90 nm and a high surface roughness ranging between ± 20 nm from the average plane.

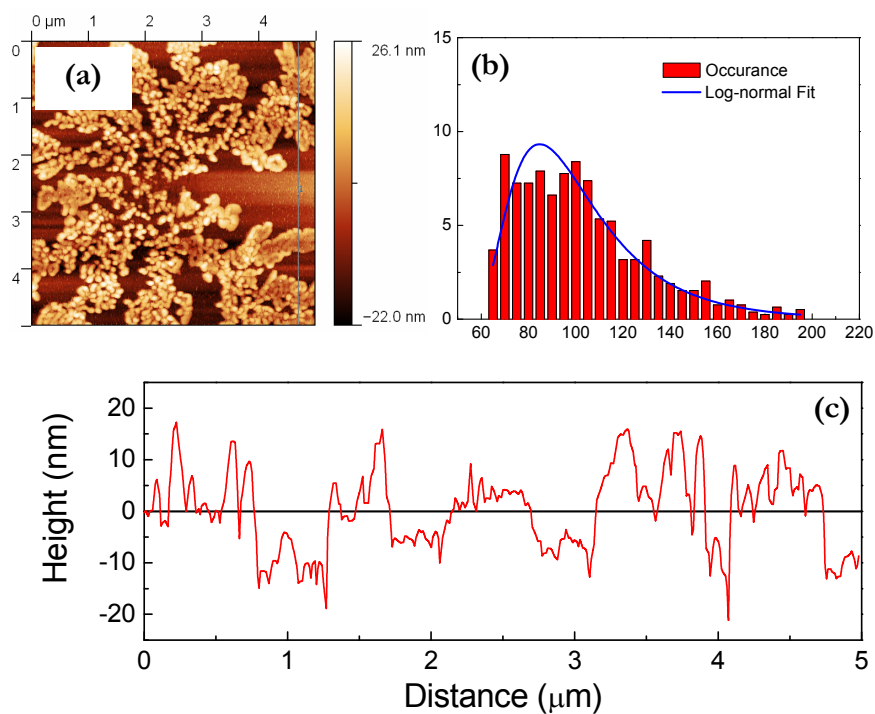


Figure 3.8 (a) Section analysis of the AFM image of a 2.3 nm (according to the sputter rate calibration) thin gold films, showing very rough 3D growth of gold for ultra-thin film thickness, (b) Grain size distribution with log normal fitting, average size of island lies between 80-90 nm, (c) Line profile showing surface roughness

It was reported in the literature that the percolation threshold for thin gold films on Si/SiO<sub>2</sub> substrate appears between 4 to 4.5 nm [Oat03]. However, in this study a linear/Ohmic I-V characteristic was observed for the minimum thickness of 7 nm. Fig. 3.9(a) shows the atomic force micrograph of the 7 nm gold sample. The average grain size ( $\approx 35$  nm) was found quite large compared to the film thickness. The line profile with roughness values less than  $\pm 2$  nm indicates a complete coverage of the substrate.



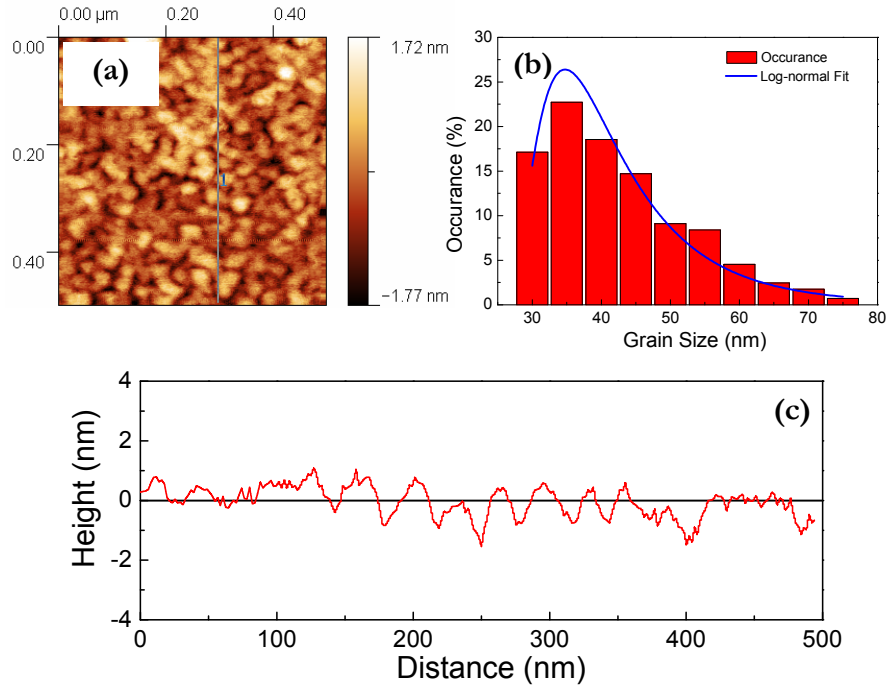


Figure 3.9 (a) Section analysis of AFM image of 7 nm gold thin film, (b) Grain size distribution with log normal fit, (c) Line profile showing surface roughness

### 3.4 ANALYSIS OF THE RESULT

The sheet resistance of a thin metal film is a function of resistivity and the film thickness, whereas the resistivity ( $\rho$ ) itself is a function of the thickness ( $t$ ), specular parameter ( $P$ ), surface charge density ( $\sigma$ ) and average grain diameter ( $d_{avg}$ ).

$$R_s = \frac{\rho(t, P, \sigma, d_{avg})}{t} \quad (3.3)$$

It is a reasonable assumption that the average grain diameter ( $d_{avg}$ ) remains unchanged during the entire period of the electrochemical surface charging and discharging.

Therefore, a change in the sheet resistance can only be associated with the other parameters in equation 3.3. Thereby, differentiating equation (3.3) we get,

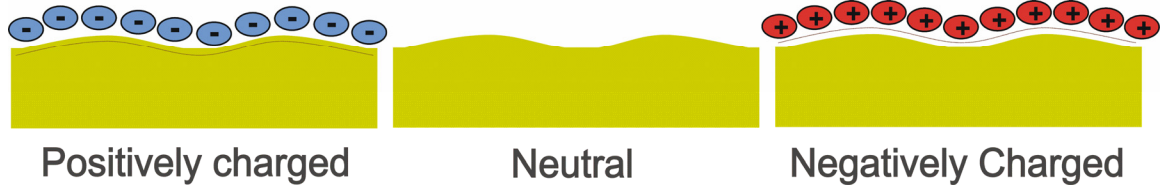


Figure 3.10 Schematic representations of the decrease and increase in effective film thickness for a positive and negatively charged film surface, respectively, versus a neutral surface

$$\frac{\Delta R_s}{R_s} = \frac{\frac{\partial \rho}{\partial t} \Delta t + \frac{\partial \rho}{\partial P} \Delta P + \frac{\partial \rho}{\partial \sigma} \Delta \sigma}{\rho} - \frac{\Delta t}{t} \quad (3.4)$$

The last component in equation (3.4),  $\frac{\Delta t}{t}$ , implies that the film thickness can also vary during the surface charging. This point however may need further clarification. The change in film thickness mentioned above relates to the change in *electronic thickness* of the film and not an atomic displacement. This virtual change in film thickness arises from the change/shift in the electron density profile with the large surface charge density. The electron density profile can be pushed towards or away from the metal/electrolyte interface with positive and negative surface charge, respectively [Gie86]. This shift is interpreted in this study as a decrease or increase of the effective thickness of the film [Das08a]. So the change in the effective thickness of the film,  $\Delta t(\sigma)$ , is a function of the applied surface charge or external field. Fig. 3.10 shows schematically, the decrease and increase in effective film thickness with respect to a large positive and negative surface charge density, respectively. For the analysis of the experimental data the change in resistance caused by both the change in the effective thickness,  $\Delta t(\sigma)$ , and by the change in scattering length,  $\frac{\partial \rho}{\partial t} \Delta t$ , are considered. It will be shown in this chapter that these two contributions can lead to a very good agreement with the experimental results.

The other two contributions shown in equation (3.4) are not considered in detail. It was not possible to consider the effect of the change in specularity,  $\frac{\partial \rho}{\partial P} \Delta P$ , quantitatively as no theoretical or experimental work is available in the literature which can quantify or relate mathematically the change in specularity with surface charge density. The remaining term in equation (3.4),  $\frac{\partial \rho}{\partial \sigma} \Delta \sigma$ , is the change of resistivity due to charge-induced surface strain (local change of the lattice parameter near the surface). Recently, Weissmüller *et al.* [Wei03] have shown the charge-induced change in lattice parameter for a nanoporous metal compact in an electrolyte. According to Sundqvist *et al.* [Sun85] the electrical resistance  $R$  of polycrystalline gold decreases linearly with pressure such as:

$$(\Delta R / R) / p = -0.028 \text{GPa}^{-1} \quad (3.5)$$

Using the value of charge induced surface stress calculated by Weissmüller *et al.* [Wei03] and the equation (3.5), the change in resistance is found to be only 0.18%, for the surface charge applied in the present study.

However, this calculation is for a nanoporous compacts, whereas the scenario in case of thin films is different. When the thin films are subject to surface charge, the film, along with the substrate behaves like a coherent lattice. The rigid substrate acts against the shear stress at the surface and as a result the change in lattice parameter becomes eventually zero even at the free surface. Therefore, we can safely disregard any contribution in resistance modulation from charge-induced surface strain in the present study.

Next, the two components which have been taken into account to explain the result are discussed in detail. The surface scattering of the carriers,  $\frac{\partial \rho}{\partial t} \Delta t$ , has a significant effect on the resistivity of the thin films when the film thickness is in the order of the bulk mean free path,  $\lambda_0$ , or smaller. This effect can be calculated using the Fuchs-Sondheimer model (FS) [Fuc38, Son52]. According to the FS model the resistivity of a thin film is given by,

$$\frac{\rho_0}{\rho_f} = 1 - \frac{3}{2k} \int_0^1 du (u - u^3)(1 - P) \frac{1 - e^{-k/u}}{1 - P e^{-k/u}} \text{ and } k = \frac{t}{\lambda_0} \quad (3.6)$$

where  $\rho_0$  and  $\rho_f$  are the bulk and thin film resistivity values, respectively,  $t$  is the film thickness,  $\lambda_0$  is the bulk mean free path, and  $P$  is the surface scattering factor (specularity parameter).

Equation (3.6) can be approximated [Son52] to offer a more convenient form for numerical calculation as,

$$\frac{\rho_f}{\rho_0} = 1 + \frac{3}{8k} (1 - P), \text{ with } k \gg 1, \text{ and} \quad (3.7)$$

$$\frac{\rho_f}{\rho_0} = \frac{4(1 - P)}{3(1 + P)} \frac{1}{k \log(1/k)}, \text{ with } k \ll 1 \quad (3.8)$$

Equation (3.8) has been revised by Mayer [May59] to give a better approximation,

$$\frac{\rho_f}{\rho_0} = \frac{4(1 - P)}{3(1 + P)} \frac{1}{k \log(1/k) + 0.4228} \quad (3.9)$$

In the present study the highest reported value of the specularity parameter,  $P$  ( $= 0.5$ ), for gold [Dur00] is used for the calculations, which in turn should result in a minimum contribution (underestimation) of surface scattering to the overall observed

effect. Before applying Fuchs-Sondheimer equation to calculate  $\frac{\partial \rho}{\partial t} \Delta t$  it is necessary to point out that the FS model alone cannot explain the observed resistivities of the thin gold films (dry samples, before introduced to the electrolyte) with different thicknesses. Therefore, it is evident that the grain boundary scattering should increase the resistivity of the ultra-thin gold films. Furthermore, the average grain size of the 7 nm film as observed from the section analysis of the AFM image (Fig. 3.9) is of the order of bulk mean free path; thereby it is reasonable to consider that the grain boundary scattering contributes largely to the increase of resistivity value. Hence, it is not possible to obtain  $\frac{\partial \rho}{\partial t} \Delta t$  just by simple differentiation of the FS equation (equation 3.9).

A model proposed by Mayadas and Shatzkes [May69, May70] (MS) considers the grain boundary scattering in increasing the resistivity of the thin films with small nanometer-size grains. Applying Mathiessen's rule to the FS and MS models, Durken and Welland [Dur00] have shown that the combined model can explain the observed resistivity very well for polycrystalline gold nanowires. The same has been done in the present study. To calculate the grain boundary scattering contribution from MS model, the average grain size obtained from AFM micrographs (=35 nm) is taken. A recently reported value of the grain boundary reflection coefficient,  $R$  (=0.85), calculated by Durken and Welland [Dur00] is used for the calculation. It can be noted that the current tunneling potentiometry study by Schneider *et al.* [Sch96] also yielded a similar value of the grain boundary reflection coefficient ( $R = 0.7-0.9$ ). Applying Mathiessen's rule to the FS and MS contribution, and taking into account that the FS and MS models both considers phonon and impurity scattering (background), the resistivity  $\rho$  of the thin films can be written as,

$$\rho_f = \rho_{FS} + \rho_{MS} - \rho_B \quad (3.10)$$

where,  $\rho_B$  is the residual (background) resistivity.

With the above values of  $P$  (=0.5) and  $R$  (=0.85), the resistivity values calculated from equation (3.10) match well with the experimentally observed resistivities for different film thicknesses (dry samples). In addition, in this way, the selection of the value of specularly parameter as 0.5 is also corroborated.

Therefore it may be noted once again that equation (3.9) is valid for an epitaxial thin film or films with very large grains in the order of micrometers but not for the films with grain size in the order of the bulk mean free path. Thereby, equation (3.9) should be modified for the polycrystalline films with nanometer-sized grains as,

$$\frac{\rho_f}{\rho_{FS}} = \frac{4(1-P)}{3(1+P)} \frac{1}{k \log(1/k) + 0.4228} \quad (3.11)$$

Differentiating equation (3.11) and using  $P = 0.5$  and the value of  $\rho_{FS}$  for the 7 nm film, we get the estimation of the scattering contribution i.e., a change in resistivity due to surface charge induced change in scattering cross-section:

$$\frac{\partial \rho}{\partial t} \frac{\Delta t}{\rho} = -0.16 \frac{\Delta t}{t} \quad (3.12)$$

Equation 3.12 implies that for the polycrystalline gold the surface charge induced change in resistance does not primarily originate from the change in scattering cross-section. In this case it is only one-sixth of the other contribution ( $\frac{\Delta t}{t}$ , the change in effective/electronic thickness of the thin film). However, as an outlook, it may be pointed out that the change of surface scattering due to an applied potential will be more pronounced and will thus contribute to a larger extent to the total change in resistance for an epitaxially grown film, i.e. without grain boundaries. Additionally a much larger contribution may also be expected for materials with higher screening depth than in a pure metal. However for a metal such as gold, the change in electronic transport possible by a change in scattering cross-section is limited by the small screening length ( $\delta$ ) of the applied surface charge in the order of a monolayer.

In absence of contribution from free surface specularly and charge induced strain equation (3.4) reduces to,

$$\frac{\Delta R_s}{R_s} = \frac{\partial \rho}{\partial t} \frac{\Delta t}{\rho} - \frac{\Delta t}{t} \quad (3.13)$$

The value of  $\Delta t(\sigma)$  is obtained from the theoretical calculation of the shift of the electron density profile from the work of Gies and Gerhardtts [Gie86] and Theophilou and Modinos [The72].

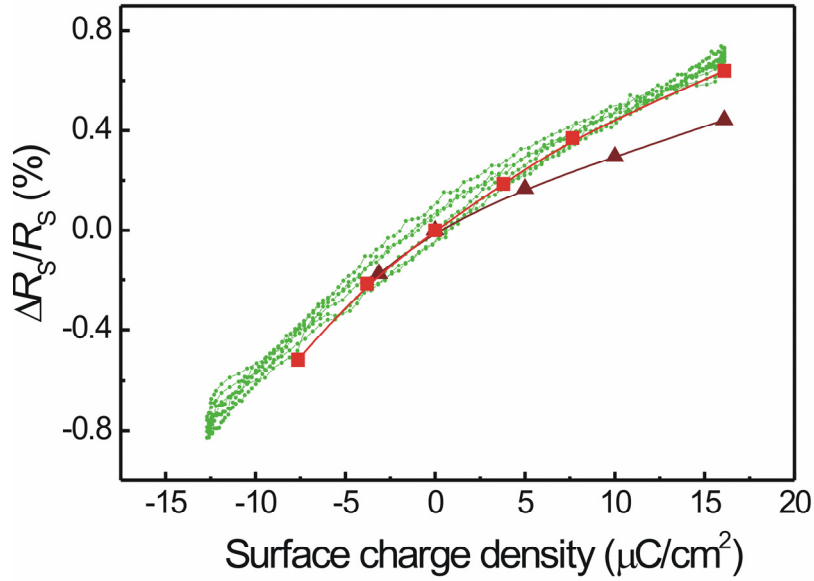


Figure 3.11 Change in resistance vs. applied surface charge density ●-● (experimental), the same calculated with  $\Delta t(\sigma)$  taken from the work of Theophilou and Modinos [The72] ▲-▲, and Gies and Gerhardtts [Gie86] ■-■

In Fig 3.11, the experimental plot of  $\frac{\Delta R_s}{R_s}$  vs.  $\sigma$  for the thinnest film (7 nm) (and therefore with a largest change in resistance) is plotted along with the effect calculated from equation (3.13). It can be noticed that the effect-size calculated theoretically matches very well with the experimental observations, in particular when the value of  $\Delta t(\sigma)$  is taken from the work of Gies and Gerhardtts [Gie86]. Therefore, it can be inferred that the strain-effect ( $\frac{\partial \rho}{\partial \sigma} \Delta \sigma$ ) and the contribution from the change in specularity ( $\frac{\partial \rho}{\partial P} \Delta P$ ), which were discarded in the beginning, seemingly do not affect the thin film resistance anyway, as the considered components are proved to be sufficient to explain the observed effect (Fig. 3.11).

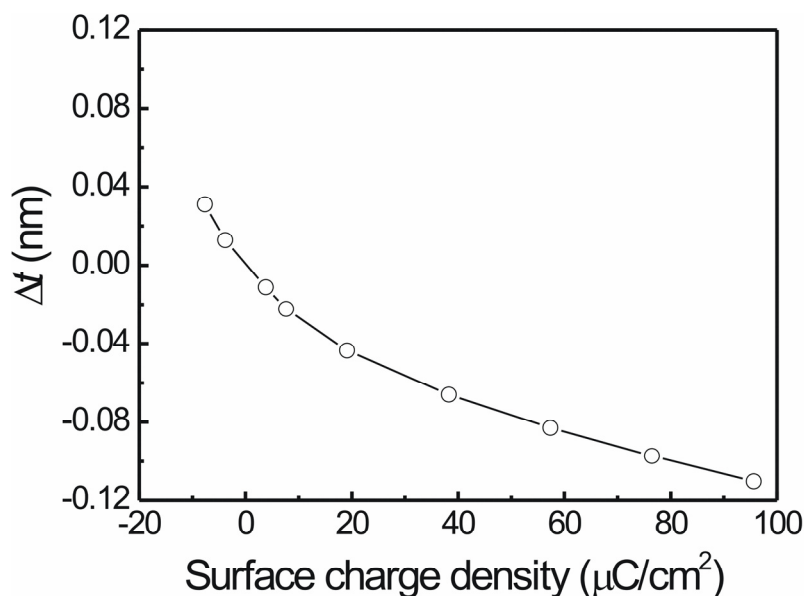


Figure 3.12 Change of effective thickness due to the shift of the center of mass  $z_0$  of induced charge vs. surface charge density, according to a self consistent calculation of the electron density by Gies and Gerhardtts [Gie86]

It is believed that further discussion is necessary regarding the relative change in effective thickness ( $\frac{\Delta t}{t}$ ) as a function of surface charge density at the metal/electrolyte interface. In the theoretical calculations by Gies and Gerhardtts [Gie86] and Theophilou and Modinos [The72] the variation of center of mass of electron density profile with the surface charge density ( $\frac{dz_0}{d\sigma}$ ) for a metal/vacuum interface remains nearly constant for the positive charge at the surface. However, an onset of a large change in slope and a rapid shift of  $z_0$ , i.e. an abrupt increase in effective film thickness ( $\Delta t$ ) is predicted for the negative surface charge (Fig. 3.12).

The spread of the electron density profile for the negative surface charge in the above mentioned theoretical predictions can be understood as an absence of repulsive force to prevent the spreading in case of a metal/vacuum interface. For instance, Gies and Gerhardtts model fails at greater than  $-8 \mu\text{C}/\text{cm}^2$  surface charge density, as it approaches the field emission regime. Therefore, it is quite straightforward that a metal/electrolyte interface will behave differently than the metal/vacuum interface described in the above models. A theoretical description for the metal/electrolyte interface was proposed by Dzhavakhidze *et al.* [Dzh91, Dzh92]. In case of a metal/vacuum interface (dielectric constant,  $\epsilon = 1$ , repulsive pseudopotential constant,  $D = 0$ ) the metal's electronic profile was free to shift/spread out of the metal/vacuum interface. In contrast, in case of a metal/electrolyte interface with a higher dielectric constant of the solvent and a non-zero

$D$  (repulsive force from the solvent towards metal's electronic profile to push it back towards metal side) the shift of the electronic profile for negative surface charge gets diminished. The spread of the profile reduces, it becomes more compact and thereby the polarizability decreases. Consequently, a strong shift of the center of mass of induced charge ( $\frac{dz_0}{d\sigma}$ ) cannot be expected as in the case of a metal/vacuum interface. However,

the shift of electronic profile for the positive charge remains practically the same for the metal/vacuum and the metal/electrolyte interfaces. The difference between metal/vacuum and metal/electrolyte interfaces disappears because of a negligible overlap between electronic tail and the medium/solvent in case of positive surface charges.

Nevertheless, a steeper slope of  $\frac{dz_0}{d\sigma}$ , for the negative surface charge may still be

expected compared to the positive charge at the surface. The actual behavior of the electronic tail for negatively charged metal/electrolyte interface is not well known and consequently, nominal non-linearity may be anticipated compared to the positively charged surface. This assumption holds as the repulsive pseudopotential ( $D$ ) within the solvent/electrolyte should always be less compared to its value inside a pure metal (with large carrier density). Therefore it may be possible to conclude that the nonlinearities in the resistance variation with respect to applied surface charge as observed in Fig. 3.11 are a result of the nonlinear relationship of the shift of the electron density profile at different signs of the surface charge, and are not necessarily resulting from the onset of a chemical reaction at the metal/electrolyte interface.



## Chapter 4

# Tuneable electron mobility in surface-charged conducting oxide thin films

### 4.1 BACKGROUND

The preceding chapter dealt with reversible change in resistance of a pure metal (gold). A highly reproducible small variation in resistance of a few percent was observed and the result was quantitatively explained with a new model proposed. Since the effect strongly depends on charge carrier density, a much larger change in electrical transport can be expected in conducting systems with carrier concentration lower than in a pure metal. On this line the surface-charge induced electric transport was measured for ultra-thin films of Indium Tin Oxide (ITO). ITO is tin doped indium oxide ( $\text{In}_2\text{O}_3$ ), is a degenerately doped semiconductor with a carrier concentration ( $n$ ) varying between  $10^{20}$   $\text{cm}^{-3}$  and  $10^{21}$   $\text{cm}^{-3}$ . Since it is degenerately doped its Fermi level lies at the conduction band and the temperature dependence of the resistivity is similar to a metal [Lin04]. The conduction electrons in ITO show free-electron like characteristic as in a metal [Oda01, Mry 01]. Another very well-known feature of ITO is its high optical transparency (over 90%) making it the best known transparent conductor available.

Before getting into the experimental details, it is worthwhile at this stage to discuss shortly the crystal structure and band structure of ITO and the criteria for a semiconductor to be optically transparent.

#### *4.1.1 Indium tin oxide (ITO) crystal structure*

To facilitate the visualization of the ITO crystal structure, let us start with the crystal structure of the parent indium oxide.  $\text{In}_2\text{O}_3$  exhibits a fluorite-type cubic bixbyite structure (space group  $Ia-3$ ). In case of a fluorite structure, such as  $\text{CaF}_2$ , calcium atoms

sit at the corners and face centers of a FCC lattice, and the eight tetrahedral interstitials are occupied by eight fluorine atoms. Thereby the calcium atoms are situated at the octahedral interstitials created by the fluorine atoms. Thus it is clear that two sublattices, both cubic, exist; one with calcium atoms, each atom surrounded by eight fluorine atom, the other with fluorine atoms, where each fluorine atom have four calcium nearest neighbors.

In case of indium oxide indium atoms occupy the calcium site and oxygen are in the fluorine site. However, in case of  $\text{In}_2\text{O}_3$  one fourth of the oxygen atoms are missing. This in turn results in two types of indium atom sites. Three-fourths of the indium atoms are located in highly distorted octahedral coordinates (d-site), which is marked as the type-1 indium site in Fig. 4.1. The other one-fourth atoms are located in the triagonally compressed octahedral sites (b-type), the type-2 indium atom in Fig. 4.1. The oxygen vacancies are located along the four  $\langle 111 \rangle$  directions. Therefore, it is possible to visualize that the smallest unit cell should contain eight of such  $\text{CaF}_2$ -type units in order to have 3-dimensional translation symmetry. The effective number of indium atoms for each of such  $\text{CaF}_2$ -type unit is four (the sublattice made of indium atoms is FCC), hence, the unit cell of indium oxide should contain 32 indium atoms and 80 atoms in total (24 d-type indium, 8 b-type indium and 48 oxygen atoms). This eventually results in a large unit cell with a lattice parameter larger than one nanometer.

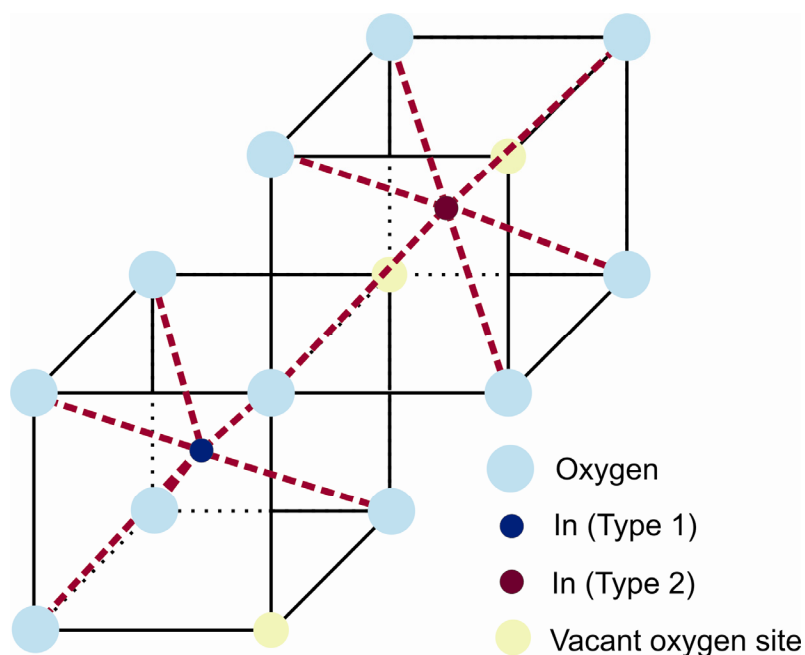


Figure 4.1 Crystal structure of indium oxide

With the addition of tin to the indium oxide lattice to form Sn doped indium oxide (ITO), Sn atoms substitute In atoms which in contradiction to Vegard's law increases the lattice parameters [Nad98]. According to Vegard's law the Sn doping ( $\text{Sn}^{4+}$  ionic radius 0.71 Å) in  $\text{In}_2\text{O}_3$  ( $\text{In}^{3+}$  ionic radius 0.81 Å) should decrease the lattice parameter. Interestingly the reported Sn-O shell radius (2.0 Å) is also smaller than the In-O radius (2.18 Å) in  $\text{In}_2\text{O}_3$ . The increase in lattice parameter with Sn doping is shown in Fig. 4.2. Above 6 at.% of Sn no further change is observed indicating the solubility limit of Sn in  $\text{In}_2\text{O}_3$ . This means that above 6 at.% the excessive Sn goes to a second phase and hence the lattice parameter of Sn doped  $\text{In}_2\text{O}_3$  phase does not alter [Nad 98]. Therefore at the solubility limit of Sn in  $\text{In}_2\text{O}_3$  is such that effectively there is one tin atom per unit cell.

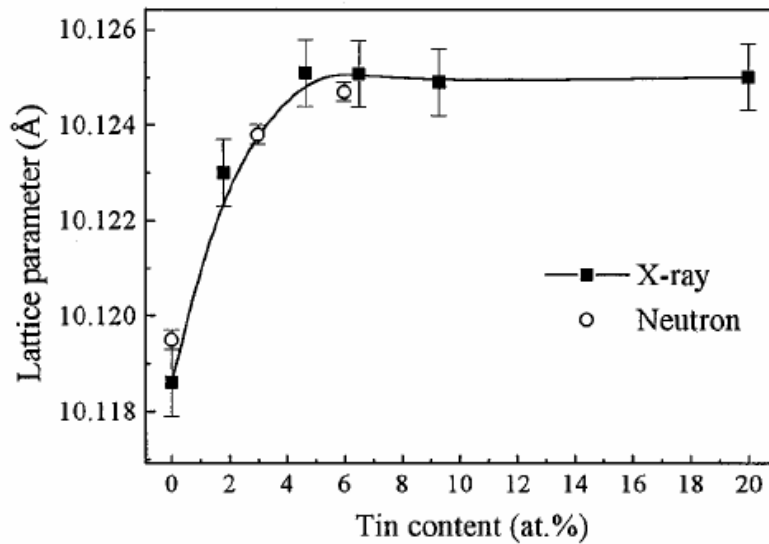


Figure 4.2 Variation of lattice parameter with tin doping in indium oxide [Nad98]

#### 4.1.2 ITO band structure

Indium oxide is a large band gap semiconductor. Direct band gap observed from optical measurement is 3.75 eV. In case of  $\text{In}_2\text{O}_3$ , the Fermi level lies in the middle of the gap. The dopant states originating from the oxygen vacancies lie below the conduction band edge. Therefore, temperature dependence of conductivity (increase in temperature increases the number of carriers in the conduction band and hence increases conductivity) is similar to a regular band-gap semiconductor. The tin doped indium oxide (ITO) however, is a degenerately doped semiconductor at room temperature. This means that the Fermi level in ITO lies above the conduction band edge. The variation of the band gap with carrier density at the conduction band of ITO is usually explained by so-called Moss-Burstein model [Gup89]. The Moss-Burstein effect results from Pauli's exclusion principle. With an increase in doping level, i.e., carrier at the

conduction band, the band gap increases. The shift arises due to a partially filled conduction band. When an optical measurement is performed to determine the direct band gap, the filled states in the conduction band block the optical excitations. Consequently the measured band gap determined by the onset of photon absorption moves to a higher energy.

The measured band gap ( $E_{gm}$ ) for a certain carrier density ( $n$ ), can be calculated provided that an estimate of the effective masses of the valence ( $m_v$ ) and conduction bands ( $m_c$ ) is possible

$$E_{gm} = E_{g0} + E_F \left( 1 + \frac{m_c}{m_v} \right) \quad (4.1)$$

where,

$$E_F = \frac{\hbar^2}{2m_c} (3\pi^2 n)^{2/3} \quad (4.2)$$

$E_{g0}$  is the intrinsic band gap in  $\text{In}_2\text{O}_3$ ,  $E_F$  is the Fermi energy and  $\hbar$  is the reduced Planck's constant. Fig. 4.3 represents the Moss-Burstein widening, schematically, assuming a parabolic band structure. Therefore in case of ITO one would expect a larger band gap than in  $\text{In}_2\text{O}_3$ . However, the measured band gap of ITO turns out to be very close to undoped indium oxide. The reason is the many body effect: due to the Coulomb interaction between electrons, and electron-impurity interaction, the conduction band bends downward and the valence band bends upward which together compensate the effect of Moss-Burstein widening [Gup89, Oda01].

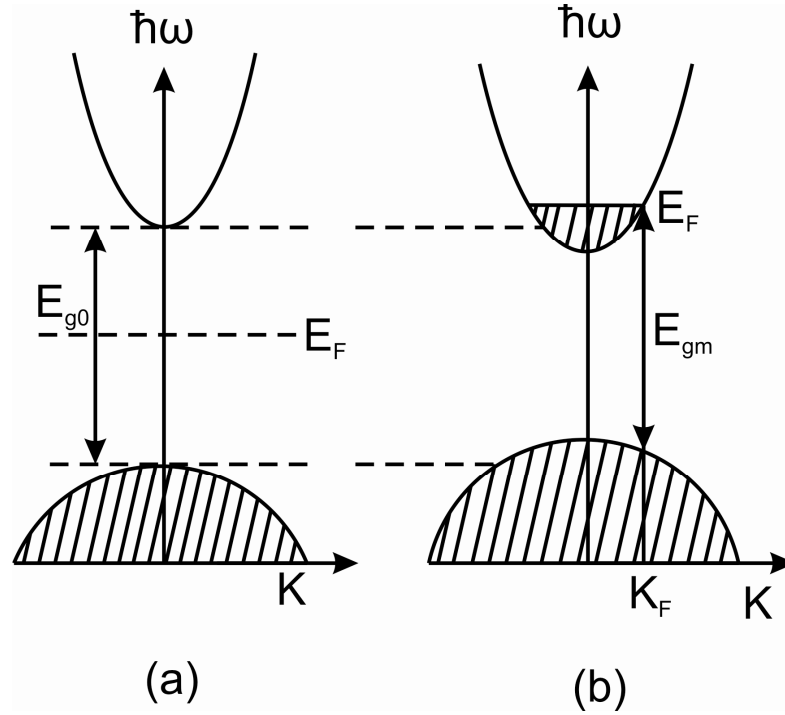


Figure 4.3 Assuming parabolic shape of the valence and conduction band the band structures of (a) undoped  $\text{In}_2\text{O}_3$  and (b) tin-doped  $\text{In}_2\text{O}_3$  are drawn; showing the Moss-Burstein widening

### 4.1.3 Criteria for the transparent conducting behavior

A metal is not transparent because the free carrier plasma frequency is above the visible range. The plasma frequency ( $\omega_p$ ) is the oscillation frequency of the free electrons inside a conducting medium such as metals. Plasma frequency can be given as:

$$\left( \omega_p^2 = \frac{ne^2}{m_e \epsilon_0} \right) \quad (4.3)$$

where,  $e$  is the elementary charge,  $m_e$  is the effective electron mass and  $\epsilon_0$  is the static dielectric constant.

On the other hand the small band gap semiconductors such as silicon are also not transparent because the interband transition occurs at frequency lower than visible range. Therefore the criteria for a transparent conductor can be summarized as [Mry01]:

- a) The material needs to possess a wide enough fundamental band gap to exclude interband transitions in the visible range.
- b) The material needs to have a single character  $s$ -type band at the bottom of the conduction band. That means the material needs to be a degenerate semiconductor. This populated conduction band would also help to increase the

band gap further by Moss-Burstein widening and keep the interband excitation further away from the optical frequency. The  $s$ -character will give high mobility to improve conductivity.

- c) The population of carriers in the conduction band should be such that the plasma frequency stays lower than the visible range.

## 4.2 THIN FILM PREPARATION AND CHARACTERIZATION

Thin films of Indium Tin Oxide ( $\text{In}_2\text{O}_3/\text{SnO}_2 = 90/10$  wt.%) were sputtered from a commercially available sputter target (Kurt J Lesker) at room temperature on thermally oxidized silicon wafer ( $\text{Si}/500\text{nm SiO}_2$ ) with  $2.5 \text{ W/cm}^2$  sputtering power and  $4.5 \times 10^{-3}$  mbar Ar pressure. The base pressure of the system was less than  $10^{-8}$  mbar. To improve crystallinity the as-sputtered films were annealed in air for 2 h at the temperature of  $550 \text{ }^\circ\text{C}$ . A shadow mask was used to obtain the ITO thin films with desired van der Pauw [Pau58a, Pau58b] geometry suitable for four-probe resistance and Hall-effect measurements. X-ray reflectometry and grazing incident X-ray diffraction were carried out using a Bruker D8 diffractometer. The thickness of the sputtered and annealed ITO thin films, as determined through X-ray reflectometry, was of 3.6, 4.5, 6, 9 and 26.5 nm respectively. Fig. 4.4 shows the experimental and simulated X-ray reflectometry data. The simulation software *Leptos* was used for the fitting.

Fig. 4.5a shows the grazing incidence X-ray diffraction patterns of the films. The average grain diameter calculated using the classical Scherrer formula suggests equiaxed grains as the grain size is nearly equal to the film thickness (Fig. 4.5b). The use of the Scherrer equation is justified since the microstrain is known to be negligible for annealed oxide thin films [Aud03].

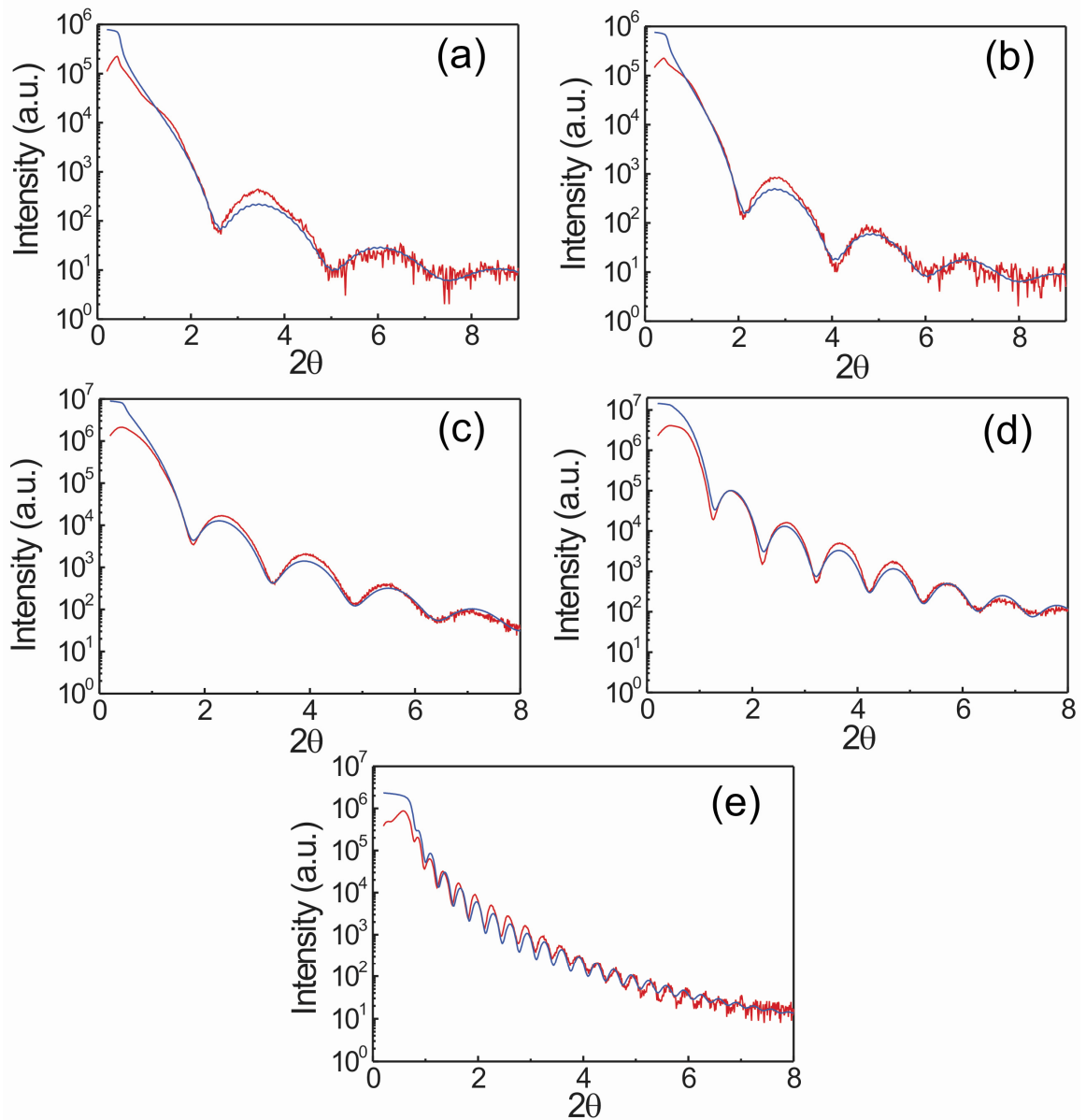


Figure 4.4 X-ray reflectometry pattern for ITO thin films; the film thickness obtained from the fit are (a) 3.6 nm, (b) 4.5 nm, (c) 6 nm, (d) 9 nm, (e) 26.5 nm, respectively. The red and blue curves denote the experimental and the simulated pattern, respectively

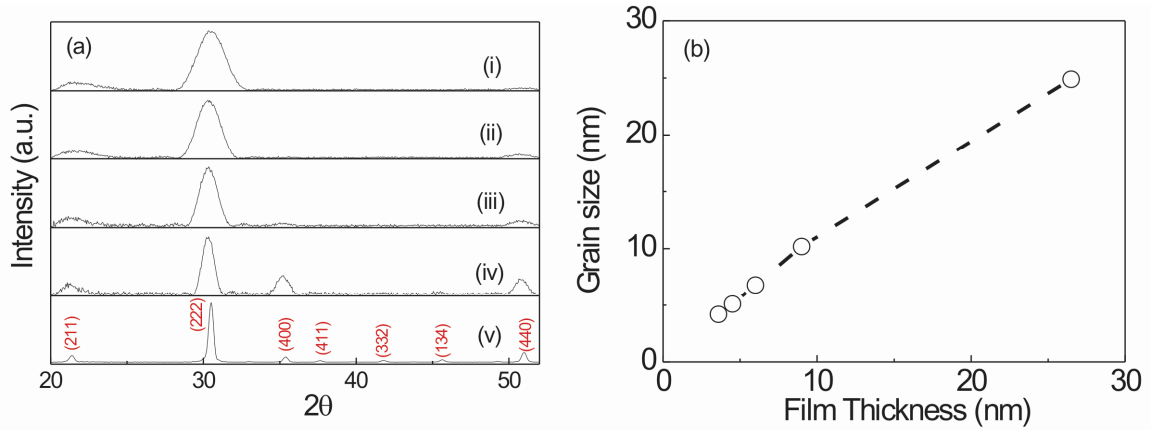


Figure 4.5 (a) The grazing incidence X-ray diffraction (GIXRD) patterns of the thin ITO films; plot (i)-(v) represent film thickness of 3.6, 4.5, 6, 9, 26.5 nm, respectively, (b) the film thickness plotted against the calculated average grain size indicates equiaxed grains

## 4.3 RESULTS

### 4.3.1 Hall-effect measurements

Our ultimate goal is to modulate the carrier concentration and carrier mobility in the ultra-thin ITO films upon electrochemical surface charging. Therefore, to quantify the extent of the modulation the initial carrier concentration ( $n_0$ ) and carrier mobility ( $\mu_0$ ) of the dry sample must be known. Hall-effect measurement of the dry films (before immersing into the electrolyte) are necessary to calculate  $n_0$ . The measured initial (dry sample) sheet resistance ( $R_{s,0}$ ) together with the knowledge of the charge carrier population ( $n_0$ ) enables calculation of the carrier mobility ( $\mu_0$ ) and electron mean free path (EMFP) ( $\lambda_0$ ) in the dry samples.

The Hall-effect measurements were performed using an extraction magnetometer (Quantum Design PPMS) using samples of van der Pauw geometry. Four contacts were placed at the four corners of a square sample, which were then marked as 1 through 4. It may be noted that if good quality digital voltmeter, accurate magnetic field intensity and constant temperature measurement is performed this method can lead to vary accurate value of hall-coefficient. The asymmetry in the sample, if any, due to the inaccurate placement of the contacts, can be taken care of by the following measurement procedure.

The measurement procedure was as follows:

- A positive magnetic field  $B$  was applied.
- A constant current  $I_{13}$  was passed through the sample and  $V_{24P}$  was measured (the suffix  $P$  denotes Hall-voltage at positive field).
- Similarly,  $V_{24P}$ ,  $V_{13P}$ , and  $V_{31P}$  were measured with  $I_{31}$ ,  $I_{42}$  and  $I_{24}$  respectively.



- d)  $V_{24N}$ ,  $V_{42N}$ ,  $V_{13N}$ ,  $V_{31N}$  were also measured likewise with a negative field of  $-B$  and  $I_{13}$ ,  $I_{31}$ ,  $I_{42}$ , and  $I_{24}$  respectively.
- e) Then four potentials were defined such as ( $V_C = V_{24P} - V_{24N}$ ); ( $V_D = V_{42P} - V_{42N}$ ); ( $V_E = V_{13P} - V_{13N}$ ); ( $V_F = V_{31P} - V_{31N}$ )
- f) Now it is possible to determine the polarity of the sample. If ( $V_C + V_D + V_E + V_F$ ) is positive (negative), the sample is  $p$ -type ( $n$ -type) provided the definition of the corner contacts 1 to 4 in the beginning was made counter-clockwise.
- g) In this way the asymmetric placements of the contact are taken care of. These sequence of measurements however would be redundant for perfectly square sample and accurately/uniformly placed corner contacts as the average hall voltage for each of the two diagonal sets of contacts would be the same.

The sheet carrier density ( $n_s$ ) ( $\text{cm}^{-2}$ ) was finally calculated as:

$$n_s = \left| \frac{8 \times 10^{-8} IB}{e(V_C + V_D + V_E + V_F)} \right| \quad (4.4)$$

where,  $B$  is the magnetic field in Oersted (Oe) and  $I$  is the dc current in amperes (A).

The bulk carrier density ( $n$ ) ( $\text{cm}^{-3}$ ) is given by,

$$n = n_s / t \quad (4.5)$$

where,  $t$  is the thickness of the film.

The Hall mobility ( $\mu$ ) can be determined as ( $\text{cm}^2\text{V}^{-1}\text{s}^{-1}$ ),

$$\mu = \frac{1}{entR_s} \quad (4.6)$$

where,  $R_s$  is the sheet resistance.

The electron mean free path ( $\lambda$ ) can now be determined as (nm) [Kit96]

$$\lambda = \frac{m_e v_F \mu}{e} \quad (4.7)$$

and

$$v_F = \frac{\hbar}{m_e} (3\pi^2 n)^{1/3} \quad (4.8)$$

where,  $v_F$  is the Fermi velocity.

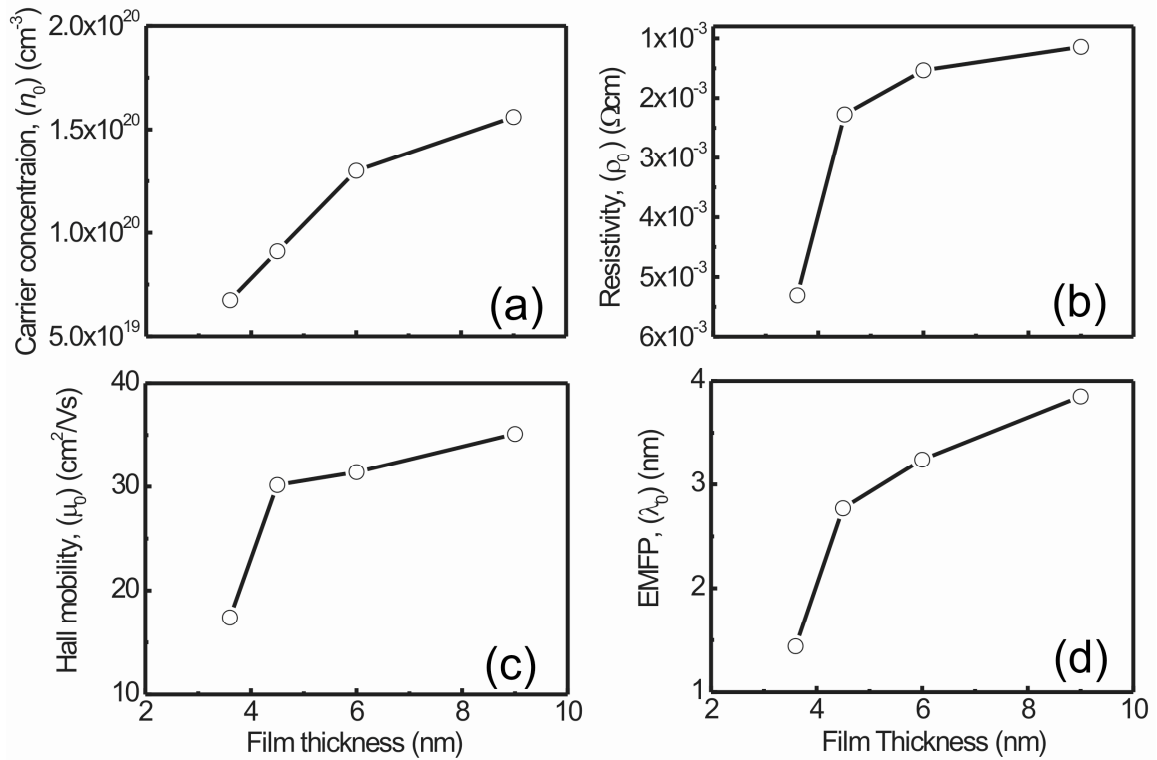


Figure 4.6 Data obtained from sheet resistance and Hall-voltage measurements performed for the dry samples. The graphs show (a) carrier concentration, (b) resistivity, (c) Hall mobility, (d) electron mean-free path, plotted versus film thickness

Fig. 4.6 summarizes the parameters obtained from the sheet resistance and Hall-effect measurements. A gradual decrease in carrier concentration from  $2.52 \times 10^{20} / \text{cm}^3$  to  $6.7 \times 10^{19} / \text{cm}^3$  was observed with the decrease in film thickness from 26.5 nm to 3.6 nm. The measured resistivity ( $\rho_0$ ) ( $\rho_0 = R_{S,0} \times t$ ,  $t$  is the film thickness) and carrier density ( $n_0$ ) allowed the calculation of carrier mobility ( $\mu_0$ ) and electron mean free path (EMFP) ( $\lambda_0$ ).

The small values of the mean free paths are characteristic of the heavily doped semiconductors [Lin04]. However, the pronounced scattering at the surfaces and at the grain boundaries is additionally limiting the EMFP in the ultra-thin, nanograined films as can be seen from Fig. 4.6d, a decrease in  $\lambda_0$  is observed with a decrease in film thickness. Therefore, the abrupt increase in resistivity for the thinnest film (3.6 nm) (Fig. 4.6b) is also due to the abrupt decrease in mobility and EMFP as can be seen from Fig. 4.6(c,d).

### 4.3.2 Selection of the capacitive potential window

A solution of 0.1 molar sodium perchlorate ( $\text{NaClO}_4$ ) (Sigma-Aldrich) in propylene carbonate (Merck) was used as an electrolyte. High surface area ( $> 1000 \text{ m}^2/\text{g}$ ) activated carbon cloth (Kynol) and a freshly prepared Ag/AgCl electrode were used as the counter and reference electrode, respectively.

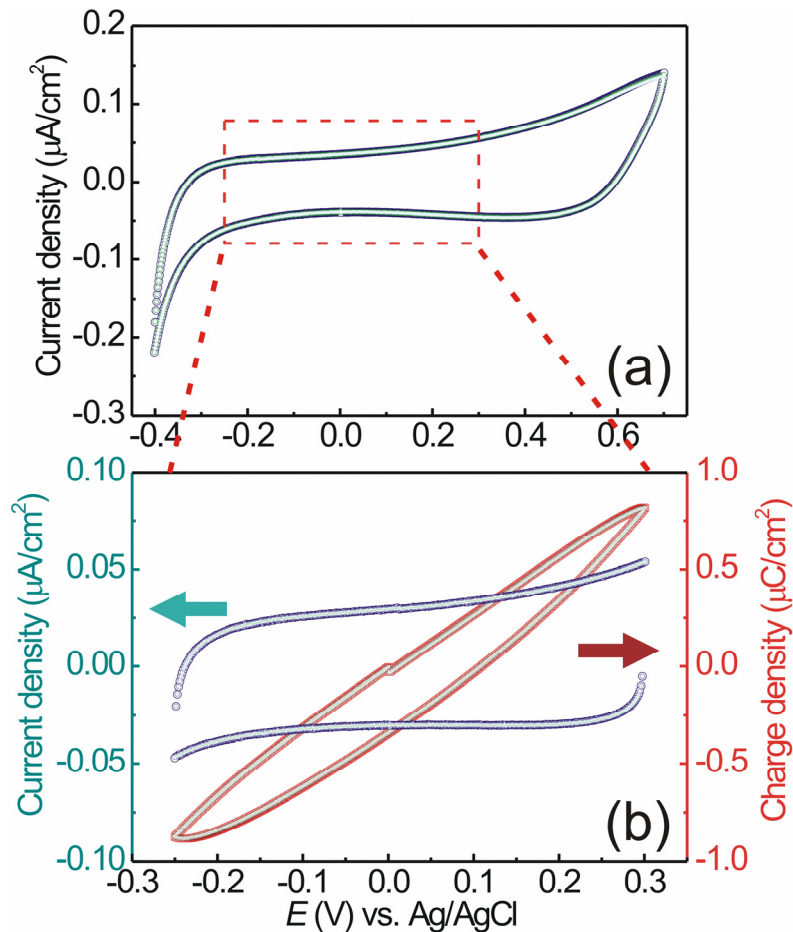


Figure 4.7 The cyclovoltammogram of the ITO thin film (3.6 nm) with a scan rate of  $10^{-3} \text{ Vs}^{-1}$ : (a) selection of the adsorption free predominantly double layer capacitive region, (b) the voltammetric cycles within the selected region, also shows the surface charge density. All the plots contain five complete potential scans

The cyclovoltammograms of the ITO film with nominal thickness of 3.6 nm are shown in Fig. 4.7. Similar to the case of gold thin films a careful selection of the adsorption-free, predominantly capacitive, potential region was performed to avoid chemical reactions at the ITO film/electrolyte interface. Therefore a slow scan-rate ( $10^{-3} \text{ Vs}^{-1}$ ) cyclovoltammetry was carried out (Fig. 4.7a) to select the desired potential window. From Fig. 4.7(a) the capacitive adsorption-free potential window from -0.25 V to 0.3 V

(vs. Ag/AgCl) was selected. Henceforth, for all the ITO films with different thickness, the potential was varied within this window. Fig. 4.7(b) shows the cyclic voltammogram of the same sample within the desired potential region. The charge accumulated on the film surface was calculated by integrating the charging current.

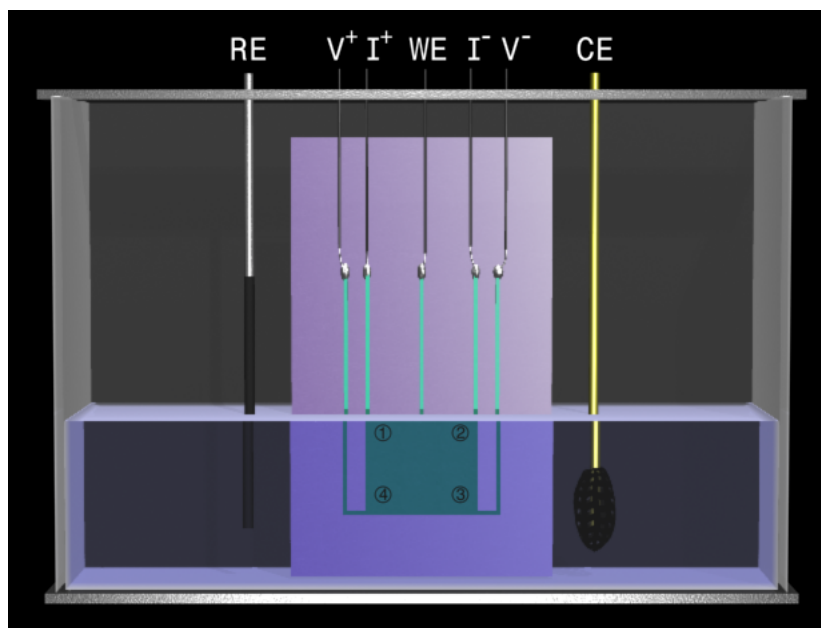


Figure 4.8 Electrochemical cell for the charge-induced resistance measurement is shown, which includes ITO thin film, (working electrode), Ag/AgCl reference and amorphous carbon counter electrode

### 4.3.3 Surface charge-induced electrical transport

The electrochemical cell used for the four probe resistance measurement was similar to that presented in Chapter two (Fig. 4.8), besides the reference and counter electrodes in this case were Ag/AgCl and high surface area carbon cloth, respectively. The charge on the thin film surface was applied by biasing the films with respect to the reference electrode. The potential window was mentioned in the last section. Simultaneously, the resistance of the film was measured passing a constant current. Therefore, this procedure is analogous to the measurement of channel conductance of a transistor with variation of the gate potential; so-called electrochemical gating. The resistance measurements were also performed with the van der Pauw method. A constant current of 1 mA was passed along one edge of the sample (for instance,  $I_{12}$ ) and the voltage across the opposite edge (in that case,  $V_{43}$ ) was measured (Fig 4.8).

To calculate the sheet resistance ( $R_s$ ), the van der Pauw equation<sup>14-15</sup> was used:

$$R_s = \frac{\pi R_A}{\ln 2} \quad (4.9)$$

where  $R_A = \frac{V_{43}}{I_{12}}$ . Fig. 4.9 shows the change in resistance of the ITO films with different thickness and hence different surface to volume ratios. It may be noted that all the measurements shown in Fig. 4.9 were initialized at the *open circuit potential* (OCP) of the thin films. The OCP was at *zero voltage* with respect to the Ag/AgCl reference electrode. Owing to the small build-in surface charge at OCP, the resistance of the films at zero voltage (denoted as  $R_{s,0}$ ) was similar to that of the dry samples. In contrast a large variation in resistance was observed when the electrode (thin film) potential was cycled within the potential window mentioned above. The resistance change ( $R_s/R_{s,0}$ ) is found to increase with a decrease of the film thickness from 9 to 3.6 nm. This is anticipated because the thinner the film is, the larger the surface to volume ratio is and hence higher the effect of surface charging. The highly reversible change in resistance (Fig. 4.9) furthermore ensures that the dominant reason for the resistance modulation is the electrostatic field-effect and that the chemisorption is negligible within the selected potential window. It is also interesting to note a significant non-linearity in the resistance variation observed only for the thinnest film (3.6 nm). Such a non-linear variation in drain current is always observed in transistor when plotted against the gate voltage.

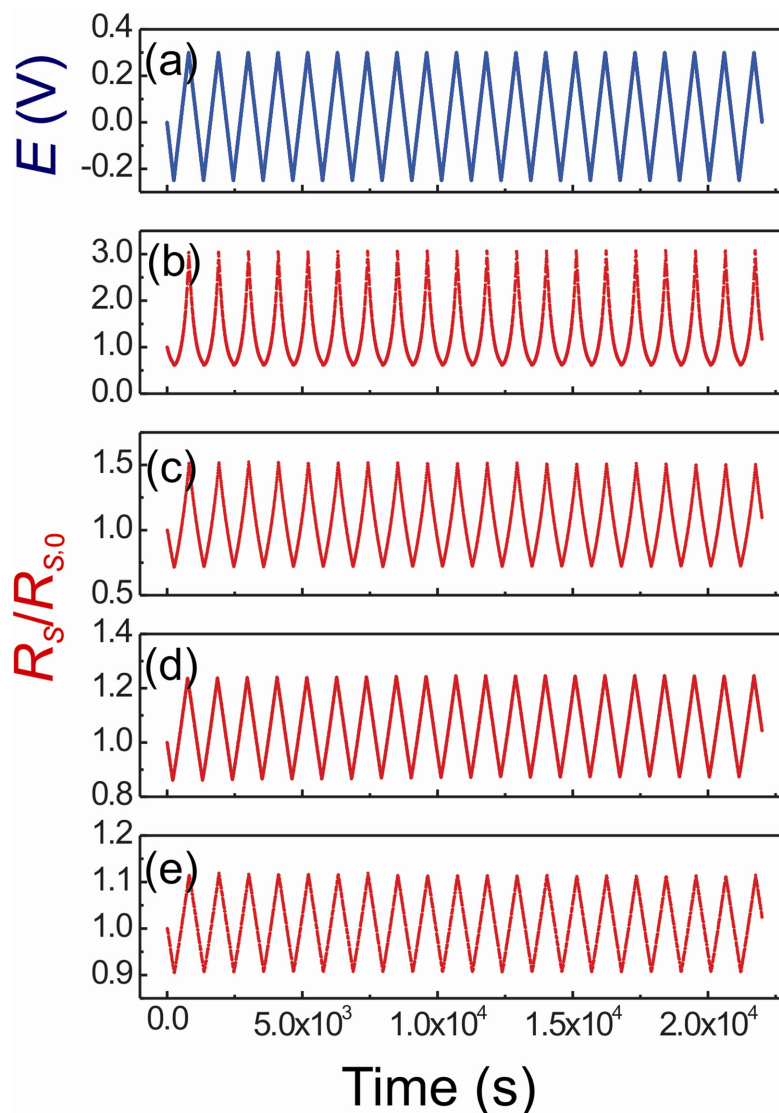


Figure 4.9 Change in the sheet resistance ( $R_s/R_{s,0}$ ) of the ITO thin films. Figure (a) shows the gate potential variation with respect to the Ag/AgCl reference electrode, (b)-(e) show resistance modulation of the ITO films with film thickness of 3.6 nm, 4.5 nm, 6 nm and 9 nm, respectively

#### 4.3.4 Scanning tunneling microscopy and spectroscopy

Scanning tunneling microscopy (STM) and spectroscopy (STS) measurements were performed on selected samples at room temperature. The samples were mounted into the ultra high vacuum (UHV) system and annealed at the temperature of 120-150 °C to remove adsorbed water from the surface. The samples were then transferred to the modified Omicron variable temperature UHV STM. All images shown were recorded in the constant current mode. In the STS mode the tip was moved to the desired position and then the feedback was switched off to keep the sample-tip distance constant. The

current was recorded while the voltage was ramped from zero to  $V = \pm 2.5$  V.

The STM images of the samples with a film thickness of 3.6 nm and 9 nm are shown in Fig. 4.10 (a) and (c), respectively. Grain size and z-corrugation of the samples are best seen in the line scans shown in Fig 4.10 (b) and (d). Apart from a plane or a sphere subtraction to compensate for the inclined mounting of the sample and the z-value artifacts of the single-tube piezoelectric scanner, the images are shown as recorded. The thinner (3.6 nm) sample shows a simple structure consisting of nearly round grains with a diameter of 2-5 nm, while the thicker one (9 nm) shows bigger grains of more irregular shape. Additionally, the bigger grains show some fine substructure. It can be clearly seen that the grains in both samples in Fig. 4.10 (a) and (c) are separated by half a nanometer deep trenches. In contrast, the substructures on the grain surfaces show much smaller height differences only in the range up to 0.1 nm. For the indium oxide lattice, the In-In, In-O, Sn-O atomic distances [Nad98] are always larger than 0.2 nm, therefore this less than 0.1 nm height modulations within the grains is most likely due to a local difference in the electronic states than due to the topography. At this point, it should be noted that the apparent height in the STM images recorded in constant current mode does not always reflect the real topographic surface features. A local increase (decrease) in the surface density of states gives rise to a higher (lower) tunneling current which induces the feedback loop of the STM to retract or approach the tip in order to keep a constant current. This movement of the tip is recorded as the apparent change in height.

To gain insight into the electronic properties of the surface, spectroscopic measurements on the grains and at the grain boundaries were performed. Measurements of the  $I(V)$  curves for the positive and negative polarity were carried out separately. To ensure a better stability of the tip, the voltage was ramped from zero to either positive or negative values. The sample was biased with respect to the tip, which was grounded. Therefore at positive voltage electrons were tunneling from the tip to the positively biased sample. An absence of data points around the Fermi level  $V = 0$  V (Fig. 4.11) can be noticed. The reason is that the smoothening procedure requires several data points on either side to generate the averaged value: therefore after smoothening no data is available around  $V = 0$  V.

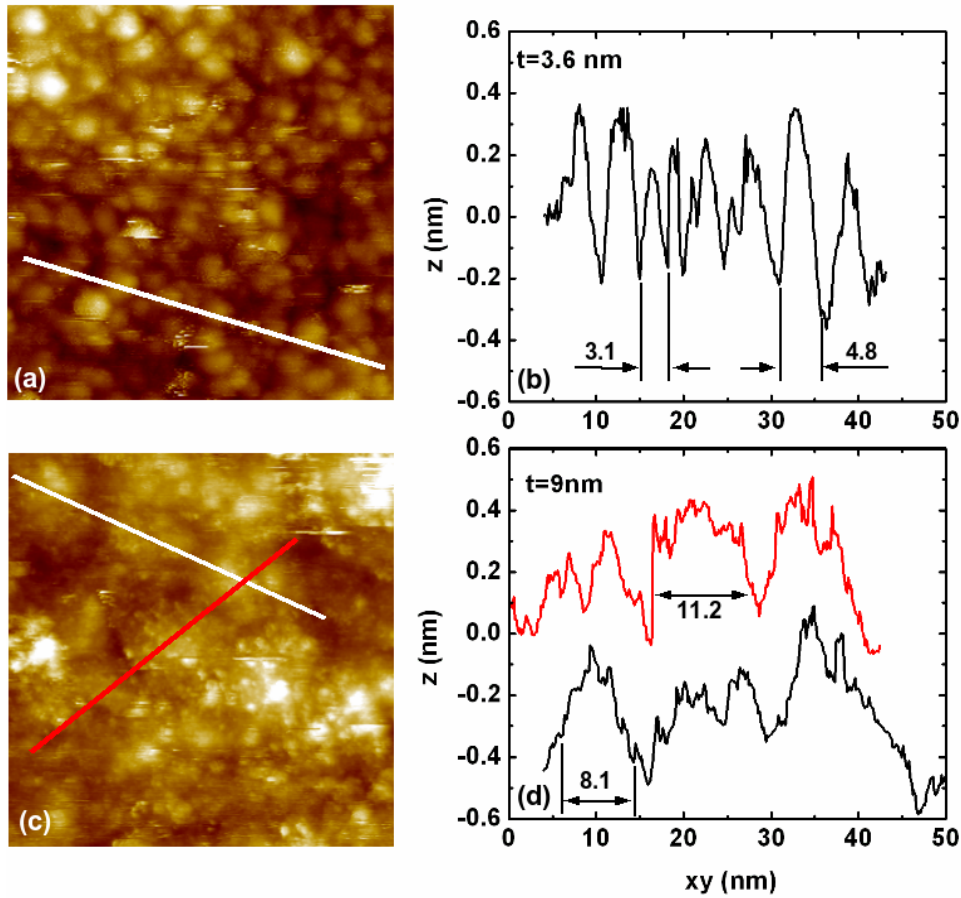


Figure 4.10 Scanning tunneling microscopy images of ITO thin films with nominal thickness of (a)  $t = 3.6$  nm and (c)  $t = 9$  nm. The corrugation along the scan lines indicated in the images is shown in (b) and (d) respectively. The grain sizes observed match well with the results of X-ray investigation

The measurements of  $I(V)$  curves with a negative voltage below  $V = -2.5$  V were possible for only a few times without obvious tip modifications induced by the voltage. Therefore, voltage values below  $-2.5$  V were not further considered due to insufficient statistics. Finally, the conductance  $dI/dV$  was calculated numerically from the smoothed  $I(V)$  data and normalized by  $I/V$  to obtain the logarithmic derivative  $d \ln I / d \ln V = (dI/dV)/(I/V)$ , which has been shown to be related to the surface density of states [Fee94]. In order to extract the characteristic features of the density of states and eliminate artifacts, an averaging over many curves was performed. About 20  $d \ln I / d \ln V$  curves per location and polarity of the applied voltage were added and then the spectra were normalized. These processed spectroscopic data are shown in Fig 4.11. The red and the black curves show the measurements on the grains and on the grain boundaries, respectively. The characteristic features are marked by A through C.



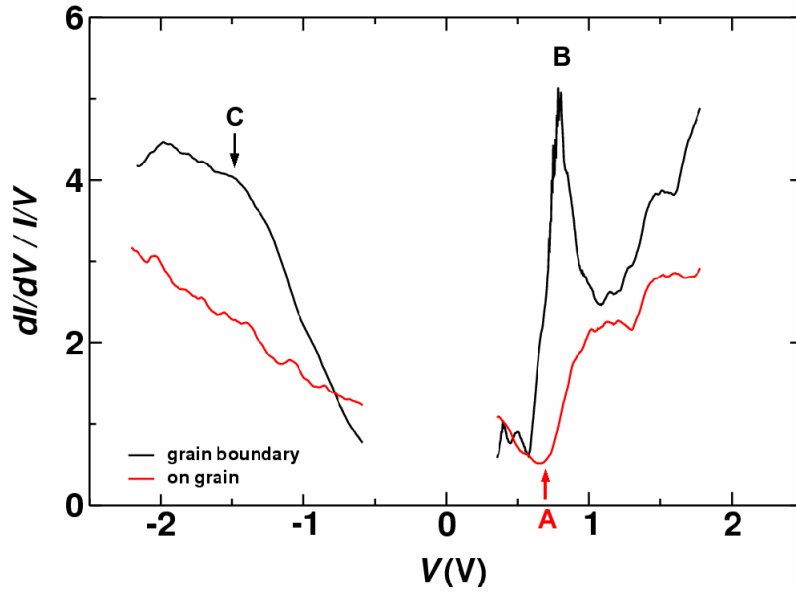


Figure 4.11 Normalized conductance  $d \ln I / d \ln V = (dI / dV) / (I / V)$  of the STS measurements on the grains (red) and above the grain boundaries (black). The characteristic features are labeled A through C

#### 4.4 ANALYSIS OF THE RESULTS

This surface charge induced large change in resistance of the thin ITO films can be analyzed by taking into account: (A) the variation in the carrier density with surface charging, (B) the modification of carrier mobility due to a change in scattering behavior upon charging.

(A) We may start with the classical Drude model [Kit96] to account for the above mentioned counterparts:

$$\sigma = \frac{ne^2\tau}{m_e} \quad (4.10)$$

where,  $\sigma$  is the conductivity and  $\tau$  is the relaxation time. Replacing relaxation time with charge carrier mobility,  $\mu$ , one obtains:

$$\rho = (ne\mu)^{-1} \quad (4.11)$$

where,  $\rho$  is the resistivity.

Hence the resistance change can be expressed:

$$\frac{R_s}{R_{s,0}} = \left( \frac{n}{n_0} \times \frac{\mu}{\mu_0} \right)^{-1} \quad (4.12)$$

where,  $n_0$  and  $\mu_0$  are the initial charge carrier concentration and carrier mobility, respectively.

The carrier concentration in the charged thin films ( $n = n_0 \pm \Delta n$ ) can be calculated knowing the initial carrier concentration ( $n_0$ ) from the Hall-coefficient measurements, measured in dry samples, and the change in carrier concentration derived by integrating the charging current ( $\Delta n = \Delta q / e$ ) of the cyclovoltammograms. The underlying assumption is that all external charges are neutralized by the corresponding change in charge carrier density in the film. This assumption is plausible as the potential window is completely in the double layer regime, without any adsorption and chemical reactions. This way the change in carrier concentration upon surface charging was calculated for all the films with different thickness using this approach. Under the assumption that the carrier mobility does not change with applied surface charge, it is possible to compare the overall experimental change in resistance ( $R_s/R_{s,0}$ ) to the one expected from the change in free carrier concentration ( $n/n_0$ ) (Fig. 4.12). It is evident from this comparison that only a small fraction of the resistance change can be explained by a change in carrier density. Hence, a large change in carrier mobility must be present.

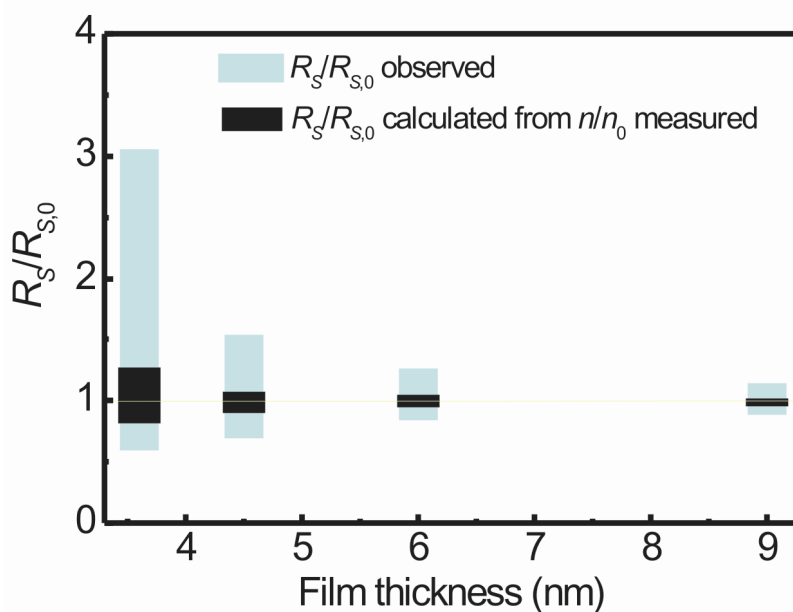


Figure 4.12 Comparison between the variations in the sheet resistance observed and the same calculated from the measured change in the number of charge carriers

(B) To consider the origin of surface-charge-induced modulation of charge carrier mobility, information about surface topography and local density of states on the grains and at the grain boundaries is essential. Therefore a careful scanning tunneling microscopy and spectroscopy study was carried out on selected samples (3.6 nm and 9 nm). The STM images and the STS normalized conductance spectra are shown in Fig. 4.10 and Fig. 4.11, respectively.

A remarkable difference between the spectra taken on the grains and those measured at the grain boundaries is observed, in agreement with Kasiviswanthan *et al.* [Kas97] but in contrast to Matino *et al.* [Mat05]. The density of states observed on the grains resembles quite well the spectra recorded by Feenstra [Fee94] for n-doped degenerate III-IV semiconductors. In degenerately doped n-type semiconductors the Fermi level  $E_F$  lies in the conduction band. Therefore, in absence of surface states one would expect a tunneling current occurring right away for  $V > 0$ . However, in degenerately doped ITO negatively charged surface states may exist [Gas06]. The charge of these surface states has to be leveled-off by a charge in the region below the surface, the so-called space charge. Therefore, the bands bend upward near the surface, bringing the conduction band above the Fermi level (Fig. 4.13). As a result, the usually filled and neutral donor levels become empty and hence positively charged. This depletion layer at  $E_F$  establishes a potential barrier for the electrons that tunnel from the surface through this depletion layer into the conduction band states in the bulk and thus reduces the tunneling probability right above  $E_F$ . Therefore, only a very weak tunneling current is found between  $V = 0-0.5$  V. For the spectra taken on the grains an onset (point A) of conductance at 0.7 eV is seen which can be related to the conduction band edge. A similar band bending induced shift of the onset of conduction band was observed by Kasiviswanthan *et al.* for nanograined ITO thin films. On the other hand, for the negative voltage, a monotonic increase in the density of states is observed. This conductance is attributed to the dopant levels which in case of a degenerate semiconductor are occupied and result in a small tunneling current at small negative voltages. This is denoted as a dopant-induced component in the literature [Fee94, Mat05]. The reported direct band gap of ITO derived from optical measurement is 3.75 eV [Wei66, Yan08, Gup89]. Therefore, if the conduction band edge at the surface is at  $V = 0.7$  eV, the surface valence band edge is expected to be at  $V = -3.05$  eV. Therefore, the onset of the valence band was not recorded within the voltage range of the present measurements.

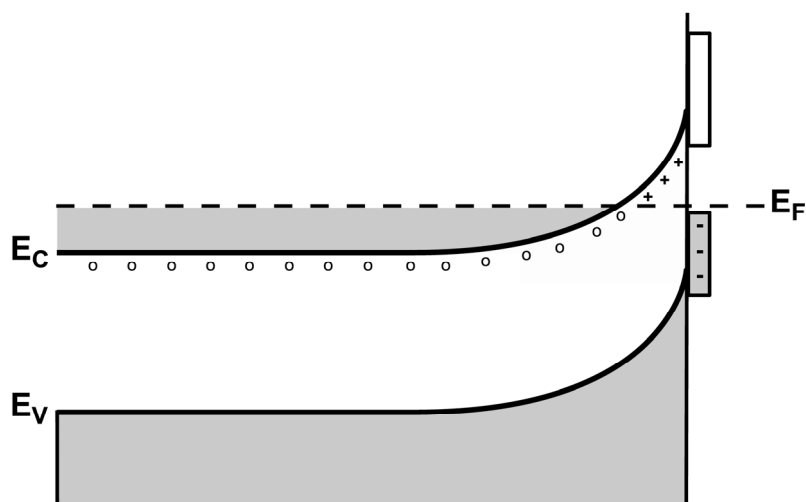


Figure 4.13 Schematic diagram of the band structure of ITO thin film. Band bending at the surface is due to the negatively charged acceptor-like surface states (shown as flat box) below  $E_F$ .

The spectra taken at the grain boundaries show a strong feature at the positive voltage (point B) in contrast to those taken on the grains. This feature can only be due to tunneling from the tip to some surface states (empty states) with a large DOS near the edge of the conduction band (Fig. 4.13). The presence of these surface states makes it difficult to determine the conduction band edge unambiguously: the onset may be somewhere around 1.1 eV. In agreement with the present results, Kasiviswanathan *et al.* also reported a shift in conduction band edge to a higher positive voltage for the spectra on the grain boundaries. An onset of the conduction band at the higher positive potential may result from a larger band bending induced by occupied, negatively charged, surface states. This is corroborated by the fact that the spectra on the grain boundaries show higher DOS at negative bias compared to the spectra on the grains. Therefore, beside the partly filled conduction band, additional occupied surface states must also be contributing to the tunneling current. A broader depletion layer induced by a larger band bending may be the reason for the low conductance between 0 to -0.5 eV. The occupied states of the grain boundaries show a smeared out shoulder with a width of about 1 eV (marked C). This is due to an averaging over a broad distribution of the onset energies for those states.

From the analysis of the STS spectra it can be undoubtedly inferred that the spectra taken above the grain boundaries show more surface states (occupied as well as unoccupied) than those taken on the grains. It is believed that these large surface states result from the crystallographic as well as the compositional disorder such as a higher free volume, Sn segregation [Mor00] and oxidation [Nad98, Eno91, Tah98] near the grain boundaries. For instance, Gassenbauer *et al.* [Gas06] have reported a direct relation between the surface states and the Sn concentration for the ITO thin films.

The excess amount of Sn and oxygen content may be correlated: the higher Sn concentration would lead to the stronger oxidation. For the air-annealed ITO thin films,

an increase in Sn concentration of up to 15 at.% near the grain boundaries compared to 5 at.% in the bulk was reported by Morikawa *et al.* [Mor00]. Since the solubility limit of Sn in  $\text{In}_2\text{O}_3$  is around 6-9 at.% [Nad98, Eno91, Tah98, Fra76, Mry01], an excess of Sn leads to phases such as  $\text{SnO}_2$  or  $\text{In}_4\text{Sn}_3\text{O}_{12}$  [Nad98, Eno91]. The formation of intergranular amorphous phases with high concentration of neutral dopants was also reported [Tah98]. Therefore, Sn segregation at the grain boundaries will bring the local Sn concentration above the solubility limit of Sn in  $\text{In}_2\text{O}_3$ , which would favor oxygen rich phases locally. Furthermore, the presence of these oxygen-rich phases would decrease the carrier concentration and conductivity of the bulk ITO [Nad98, Eno91, Tah98]. The lowest conductivity in ITO occurs at 6.5-10 at.% of the bulk Sn concentration [Nis96, Koe75, Fra82, Agn78, Ala00] which matches well with the reported solubility limit and is coherent with the model discussed here. It is expected that Sn segregation and oxidation at the grain boundaries decreases the local carrier concentration and this should lead to a larger band bending [Moe01]. Indeed, the onset of the conduction band was found to occur at a higher positive bias in the spectra taken on the grain boundaries compared to those on the grains.

Next, the possible relation of this local variation in the density of states with the large change in field-induced resistance will be considered. As can be seen from Fig. 4.10 (b, d) a minor corrugation of the order of less than 0.1 nm was observed on the grain surface, which is believed to be due to a difference in the local electronic states. A local variation in the electronic states on the grains would lead to an inhomogeneous penetration of the electrostatic field applied at the surface. This in turn would make the film electronically rougher. This increase in micro-roughness of the surface may decrease the possibility of specular (elastic) scattering of electrons at the surfaces. It is well known that a variation of surface specularity may lead to a large change of carrier mobility and hence of resistivity [Ber71, Irv66, Luc65]. Furthermore, from the above discussion it may be inferred that the Sn segregation leads to grain boundary oxidation and consequently a decrease in carrier concentration at the grain boundaries. Hence, a positive field applied on the film surface would disrupt the conduction paths deeper at the grain boundaries. This would result in an enhanced grain boundary scattering. The increase in electronic surface roughness and carrier depletion at the grain boundaries for positively charged ITO surface (Negative ions build the double layer) is shown schematically in Fig. 4.14.

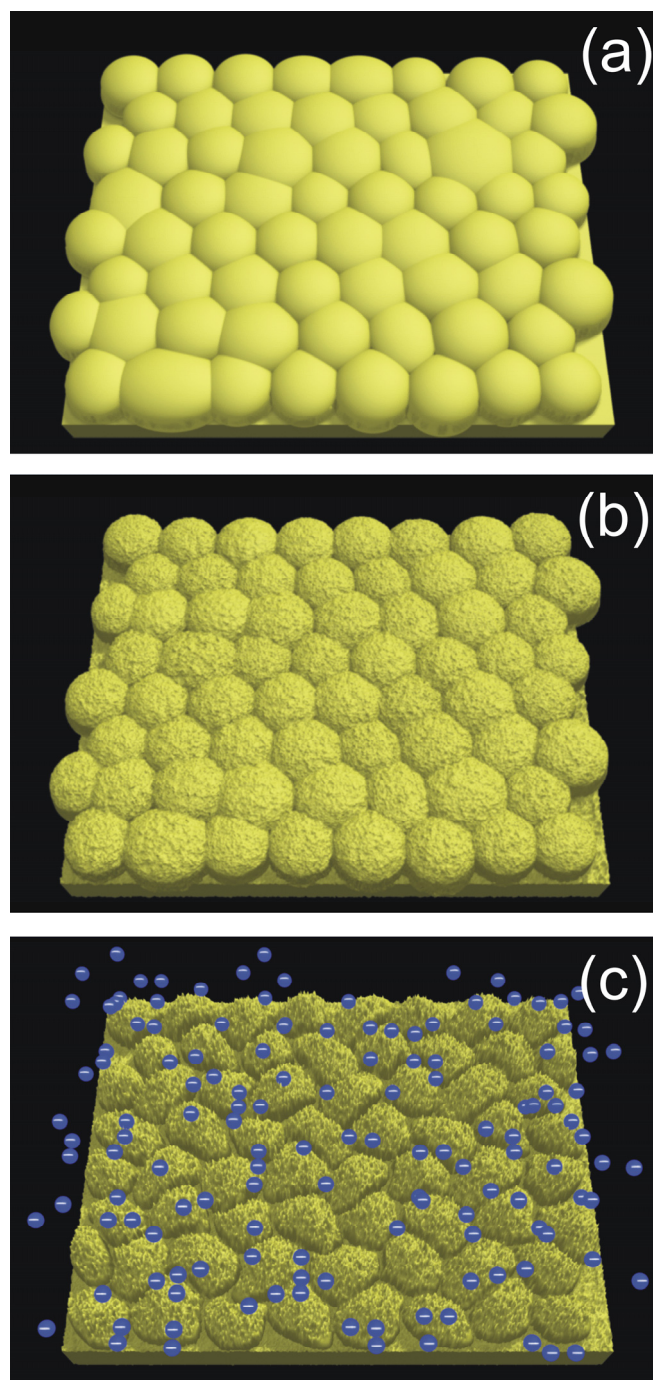


*Figure 4.14 Topological sketch of the geometric surface of the ITO thin film (a); electronic surface of the same film showing minor electronic roughness (variation in LDOS) as was observed in the STM images (b); the increased electronic surface roughness and depleted grain boundaries with the negative ions at the surface forming the electric double layer (c).*

One can conclude that in case of an oxide conductor where the dopant segregation at the grain boundary leads to oxidation and in turn decrease in number of

carriers; the field-induced tuneable modulation in the charge carrier mobility may cause a large field-effect which would not be observed otherwise [Das09a].

To realize the extent of the tuneable charge carrier mobility the thinnest film (3.6 nm) for which the resistance change is maximum is considered. With the positive surface charge (negative ions at the ITO interface) on the ITO surface, an increase in resistance by more than three times is observed. The decrease in mobility ( $\mu = \mu_0 - \Delta\mu$ ) required to balance the equation 4.12 can be calculated. For the positively charged surface a decrease in carrier concentration of  $5.12 \times 10^{12}$  can be calculated from the integration of the charging current of the cyclovoltammogram in Fig. 4.7b. Taking this decrease in carrier concentration into account, a decrease of carrier mobility from  $17.4 \text{ cm}^2/\text{Vs}$  to  $7.6 \text{ cm}^2/\text{Vs}$  is necessary to explain the observed change in resistance. It is interesting to note that a more than two-fold change in carrier mobility is achieved with the change of surface and grain boundary scattering due to the surface charge at the thin film/electrolyte interface.

Of course caution should be exercised when applying the free electron gas model to an electronically inhomogeneous system. If the grain boundaries are the high resistive ligaments in the conducting film and the bulk transport is determined by the number of carriers and their mobility near the grain boundaries, then the electronic transport calculations should rather be carried out for the grain boundary regions only. A higher relative change in carrier concentration around grain boundaries caused by the surface charge would result in a smaller change in mobility required to explain the observed effect. Nevertheless, the main conclusion still holds that an inhomogeneous field penetration, especially at the grain boundaries, is playing a decisive role in modulation of the bulk conductivity of ITO nanostructures. It may be a general trend for the polycrystalline, degenerately doped, semiconducting nanostructures (such as thin films, nanoparticles and/or polycrystalline nanowires) that the dopant segregation near the grain boundary or inter-particle neck results in a large charge-induced resistance modulation. Therefore it can be concluded that a large field-effect on the electronic transport may still be expected for conducting oxides such as ITO even when the applied field is not large enough for sufficient depletion of the bulk charge carriers.

## CHAPTER FOUR



## Chapter 5

# Nanoparticle channel field-effect transistor with solid electrolyte gating

### 5.1 BACKGROUND

The field-effect transistor (FET) devices have redefined human life in the last fifty years with their countless new applications. In this chapter, an all-solid state field-effect transistor device based on Indium Tin Oxide (ITO) nanoparticle channel is presented. The understanding of tuneable transport properties gained from ultra-thin ITO films indicates that ITO nanoparticles with even higher surface area per unit volume and small inter-particle necks would result in a larger change in electronic transport compared to thin films. Indeed, a change in resistance of more than 300 times was observed when an air annealed ITO nanoparticulate film was dipped into the same non-aqueous electrolyte (0.1 M NaClO<sub>4</sub> in propylene carbonate). Another step forward in terms of future applications is a replacement of the non-aqueous liquid electrolyte with a solid one. Therefore the requirement was to have an electrolyte which can be easily solution casted or spin coated over the nanoparticulate film.

The nanoparticulate film made of solution processed (spin coated) ITO nanoparticles shows a resistance variation of more than three orders of magnitude when the surface potential of the nanoparticles is varied by 1100 mV. A device with standard transistor geometry (passive structures and properly selected channel dimensions) was then pursued to achieve current-voltage characteristics similar to a field-effect transistor. In the chosen configuration, therefore, the solid electrolyte works like a gate oxide, and the ITO nanoparticulate channel depletes (narrower) or accumulates (broader) charge carrier with respect to different gate bias making the device analogous to a junction field-effect transistor (JFET).

At this point it may be noted that there are only few reports on nanoparticulate

channel transistor devices in the literature and that those reported ones (PbSe nanoparticle [Tal05] and  $\text{In}_2\text{O}_3$  nanoparticle [Cui05]) do not show very exciting transistor characteristics. In contrast polymer electrolyte gating has been reported widely in the field of single-wall carbon nanotubes [Sid04, Oze05] (SWCNT) and organic semiconductors [Yue07, Pan05, Pan06, Pan07]. However, these approaches mostly involve electrochemical doping (redox reactions i.e., charge transfer through the channel/electrolyte interface), as opposed to the electrostatic doping (field effect) in the present study. In this study the gate voltage is intentionally restricted within the adsorption-free predominantly capacitive double layer potential region. As a first approximation the electric double layer at the nanoparticle/electrolyte interface can be compared with a simple plate capacitor (Helmholtz model). Therefore, in the absence of specific adsorption, a high reversibility and long term reproducibility of the device can be expected.

The advantages of electrochemical gating in case of a nanoparticle channel transistor device are as follows:

- a) orders of magnitude higher charge on the channel compared to any existing gate dielectric,
- b) easy device fabrication,
- c) a low gate voltage requirement,
- d) as already mentioned previously (Chapter Zero: Motivation) in case of a nanoparticle channel transistor, an electrolyte gating offers the significant additional advantage as it easily penetrates the nanoporous network to reach all available surfaces of the nanoparticulate array. Consequently, the applied electric field surrounds the surfaces of each individual nanoparticle and the necks between the nanoparticles as opposed to a field penetration just from one side as it is the case with the dielectric gating.

## 5.2 PREPARATION OF THE DEVICE

The ITO nanoparticulate channel transistor presented in this chapter is an electrochemically gated field effect transistor device which resembles a junction field effect transistor (JFET). Fig. 5.1 shows the schematic of the device. In contrast to a dielectric-gated thin film transistor device generally reported in the literature, here the field is applied with an electrolyte which as mentioned previously suits better for nanoparticle channel device as the applied field surrounds all the nanoparticles comprising the channel. In this regard a careful selection of the electrolyte was necessary. It was intended to have a solid state electrolyte for application benefit. All the different kinds of solid electrolytes are listed in chapter one. The crystalline ones are generally not good conductors at room temperature (RT). Some of the glassy/amorphous electrolytes possess good conductivity at RT and also can be easily

synthesized via high energy ball milling (HEBM). However, in this case the limitation is that the particle size is of the order of microns and increase in milling intensity to reduce the particle size results in crystallization. Generally it is difficult to achieve nanometer-size glassy particles [Gle08]. It is therefore difficult to achieve a composite with ITO nanoparticles and the glassy electrolyte where the nanoparticle interface is sufficiently covered by the electrolyte. Therefore we choose a polymer based solid electrolyte. A gel-type electrolyte with a solvent other than the polymer matrix is chosen as they show high room temperature conductivity. Another important advantage in this case is they are liquid in the beginning hence can easily be solution casted over the nanoparticulate channel and become solid after evaporation of the excess solvent. In this way it is possible that all the exposed surfaces of the nanoparticles including the nanopores are covered with the electrolyte and a smooth electrode-electrolyte interface is also achieved. A water soluble (the polymer was dissolved in deionized  $H_2O$ ) polymer electrolyte was favored to have high conductivity of the electrolyte and high charge density at the electrode surface; the high dielectric constant of water ( $\epsilon_{H_2O} = 80$ ) ensures a high polarizability of an aqueous electrolytes. Potassium fluoride (KF) was chosen as the supporting electrolyte because both the ions are extremely non-adsorbing; hence would result in a larger capacitive potential window. Polyvinyl alcohol (PVA) was the polymeric agent. The dissolved salt (KF) and the solvent ( $H_2O$ ) resulted in a clear (colorless) fluid which turns either to a colorless or a white solid membrane after the evaporation of the excess water.

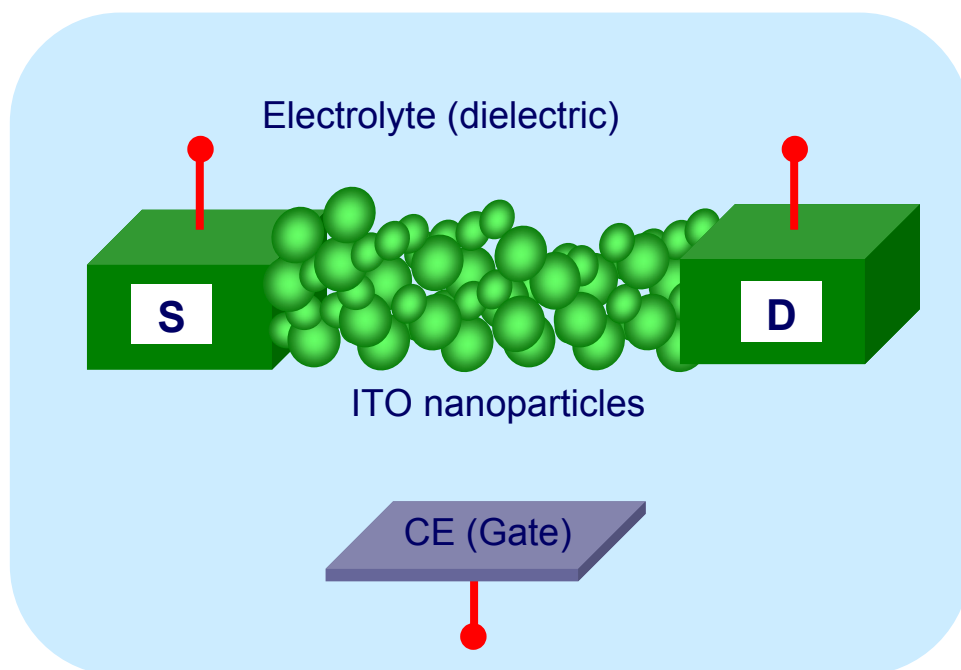


Figure 5.1 Schematic of the electrochemically gated field-effect transistor device

The device fabrication started with a 310 nm thick ITO film sputtered on glass substrate (high quality float glass). The ITO substrate was coated with Poly(methyl methacrylate) (PMMA A4 950K, Micro-Chem) with 3000 rpm rotational speed to end up with a PMMA layer thickness of approximately 200 nm. After baking at 185 °C, the structuring was performed with e-beam lithography. After developing the structure [developer: MIBK (Methyl isobutyl ketone): Isopropanol = 1:3] for 30 s, the exposed areas were etched with argon ion etching (Oxford Plasmalab). The etching time required to etch 310 nm of ITO was 50 minutes (with 100 Watt forward-power and 30 sccm of Ar flow). Subsequently, a second e-beam lithography step followed to determine a  $5 \times 40 \mu\text{m}^2$  window for spin coating of the commercial ITO nanoparticles (5 at.% Sn) dispersion (Evonik GmbH). Fig. 5.2 summarizes the lithography steps schematically. The length and width of the channel (5 and  $40 \mu\text{m}$ ,  $L/D = 1:8$ ) is kept small to ensure fast charging.

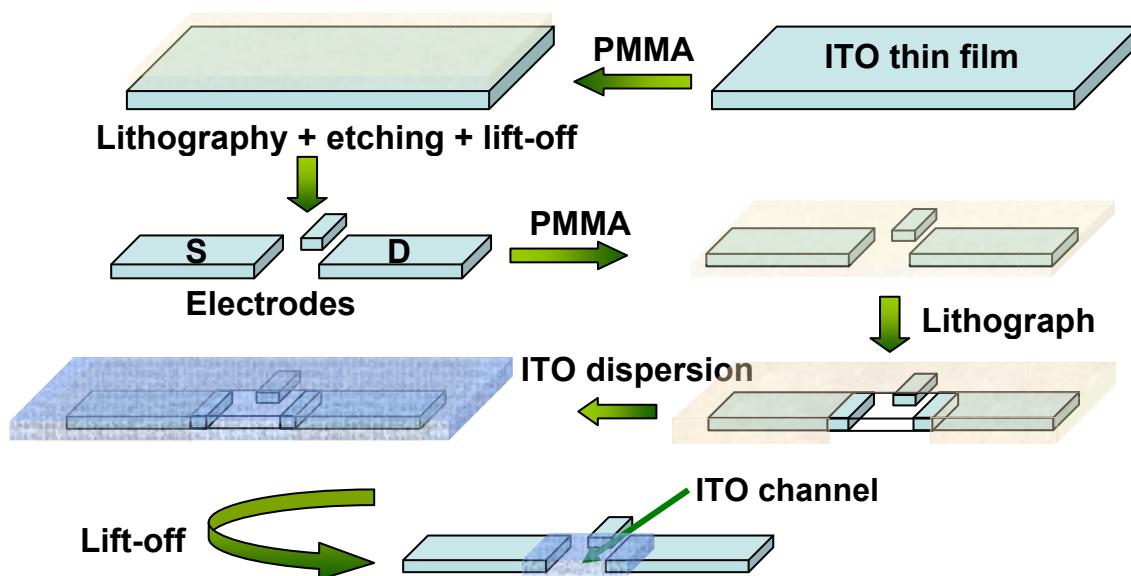
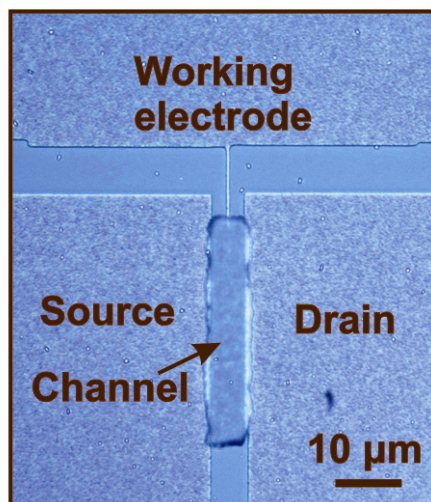


Figure 5.2 Schematic representation of the preparation steps of the patterned substrate and ITO nanoparticulate film (transistor channel) via e-beam lithography

The sample geometry consisting of contact leads and the ITO nanoparticle channel is shown in Fig 5.3. The contact leads are made of sputtered ITO films (rough and dark in Fig. 5.3) on high quality float glass (smooth and bright in Fig. 5.3) substrate. In addition to the source (*S*) and drain (*D*), a third contact, is placed in the middle of the gap between *S* and *D*. This third contact connects to the working electrode of a potentiostat. The purpose of the third contact is to charge the nanoparticle array uniformly with respect to the source and drain to avoid transient effects [Tuc04].



*Figure 5.3 Optical micrograph of the device showing the source and drain made of sputtered ITO film and the channel made of ITO nanoparticles*

After the spin coating of the nanoparticle dispersion a low temperature (185 °C) annealing for 1 h is performed prior to the PMMA layer lift-off with acetone. By this low temperature annealing we promote some adhesion of the nanoparticulate film to the glass substrate in the channel area where it was not covered with PMMA. Therefore during the lift-off with acetone it was possible to use sonication for a short time (15 s) to remove the PMMA and nanoparticulate ITO film from everywhere other than the channel area. After the lift-off the nanoparticulate film is then annealed in air for 2 hrs at 550°C to get rid of organic surfactants present in the dispersion.

A composite solid-state polymer electrolyte composed of polyvinyl alcohol (PVA), potassium fluoride (KF) and water (35:35:30) is used for electrochemical gating. The solid polymeric electrolyte is prepared by the solution casting method. PVA (Sigma Aldrich) and KF (Merck) are used as received without further purification. The degree of polymerization and saponification of PVA were 300-525 and 98% (as reported by the supplier), respectively. A comparatively lower molecular weight polymer was used. It was observed that lower the molecular weight of PVA, the higher the amount of supporting electrolyte can be dissolved in it. A higher concentration of KF was essential to increase the conductivity of the polymer electrolyte. Equal weights of PVA and KF were dissolved separately in water. The PVA and water mixture was kept at 75°C and stirred for 2 hrs. The clear solution of KF was then added to the homogeneous solution of PVA under continuous stirring. The mixture is then stirred at 60 °C continuously until the complete solution became a clear, homogeneous and viscous fluid. This electrolyte was then solution casted and dried in-situ on the ITO channel device. It was observed that depending on the membrane thickness it might take few minutes to several hours to dry at room temperature (RT). It was noticed that to have a homogeneous, defect-free

(cracks) high quality solid electrolyte, slow room temperature evaporation of the excess water was necessary. After the evaporation of the excess water, the electrolyte became solid and opaque (white). The transparency of the solid electrolyte depends on the amount of salt (KF, in this case) dissolved in it. At 1:1 PVA: KF ratio the final form of the solid electrolyte is always opaque (white). Lowering the KF concentration improves transparency but decreases the conductivity of the electrolyte.

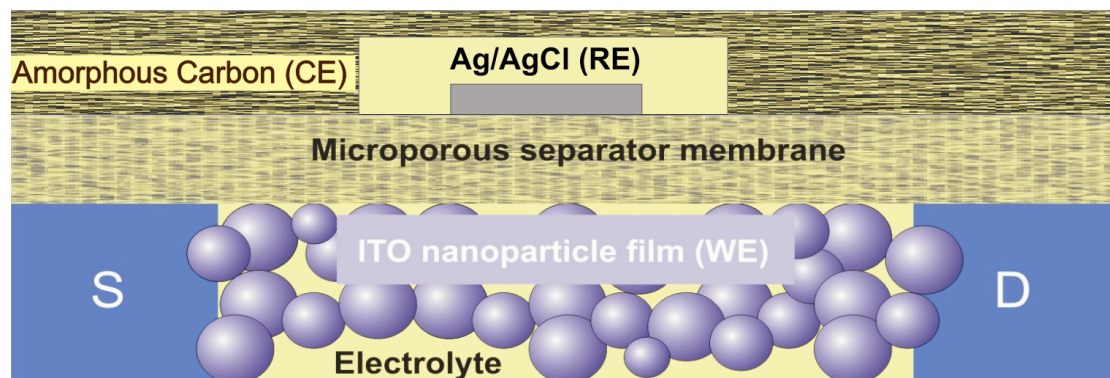


*Figure 5.4 Schematic representation of the cross-section of the device. Source (S) and drain (D) made of sputtered ITO thin film, ITO nanoparticles consisting the working electrode (WE), amorphous carbon and Ag/AgCl are the counter (CE) and reference (RE) electrodes, respectively*

High surface area ( $> 1000 \text{ m}^2/\text{g}$ ) activated carbon cloth (Kynol) and a freshly prepared Ag/AgCl electrode were used as the counter and reference electrode, respectively. A Celgard 2325 microporous membrane (25  $\mu\text{m}$  thickness, 40/90 nm pore size) was used to separate the respective electrodes. Fig. 5.4 shows schematically the cross section of the ITO nanoparticle-based thin film transistor. After placing the separator membrane and other electrodes (as shown in Fig. 5.4), the electrolyte solution was added to the device structure. An all-solid-state device was obtained following the slow, room temperature evaporation of the excess water. The composition of the polymer electrolyte was determined with a mass balance from a dried electrolyte membrane following the complete evaporation of the excess water.

## 5.3 RESULTS

### *5.3.1 Microstructural investigations*

To obtain the essential information about the nanoparticle morphology and interparticle contacts/necks, Transmission Electron Microscopy (TEM) images were taken. It is especially important for the field-effect mobility calculations that a good

understanding of the microstructure of the nanoparticulate aggregate is available. Therefore a series of single-axis tilt-angle tomography images were acquired and analyzed using mathematical algorithm in order to obtain approximated values of morphological parameters like average particle size, pore-to-particle volume ratio etc., which were later utilized for the calculation of field-effect mobility. Samples for transmission electron microscopy were prepared separately on gold and  $\text{Si}_3\text{N}_4$  grids with spin coating parameters and annealing conditions identical as to the original device structure. The silicon nitride grids with 30 nm free standing  $\text{Si}_3\text{N}_4$  membrane were used for the conventional bright-field imaging (Fig. 5.5(a-c)). Equiaxed particles with average size of 15 nm and small size distribution can be seen.

HAADF-STEM tomography was carried out in a *FEI Tecnai F20ST* field-emission gun (FEG)-TEM operated at 200 kV, fitted with a *Fischione FP-5360/20* HAADF detector. The tomography images were acquired automatically using the *Xplore3D 2.0* tomography suite operated in the HAADF-STEM. A camera length of 70 mm (corresponding to a minimum scattering angle of 50 mrad) was used for the signal collection in order to minimize diffraction effects. A total of 111 micrographs were collected over a tilt range of  $\pm 70^\circ$  with  $1.25^\circ$  steps. The alignment of the individual stacks and the reconstruction of the acquired tilt series was done off-line using FEI's software package *Inspect 3D Version 2.1*. The aligned tilt series was reconstructed using the iterative back-projection process SIRT [Gil72] which is actually utilized in the *Inspect 3D* software. The software package *Amira 3.1* has been used for the visualization of the reconstructed structures. For stereological analysis, the reconstruction was binarized and then cropped in all spatial directions (to  $240 \text{ nm} \times 135 \text{ nm} \times 80 \text{ nm}$ ) in order to remove the macroscopic sample surfaces, to avoid artifacts at the borders of the reconstruction, and to ensure that the volume used for analysis is representative of the bulk sample structure.

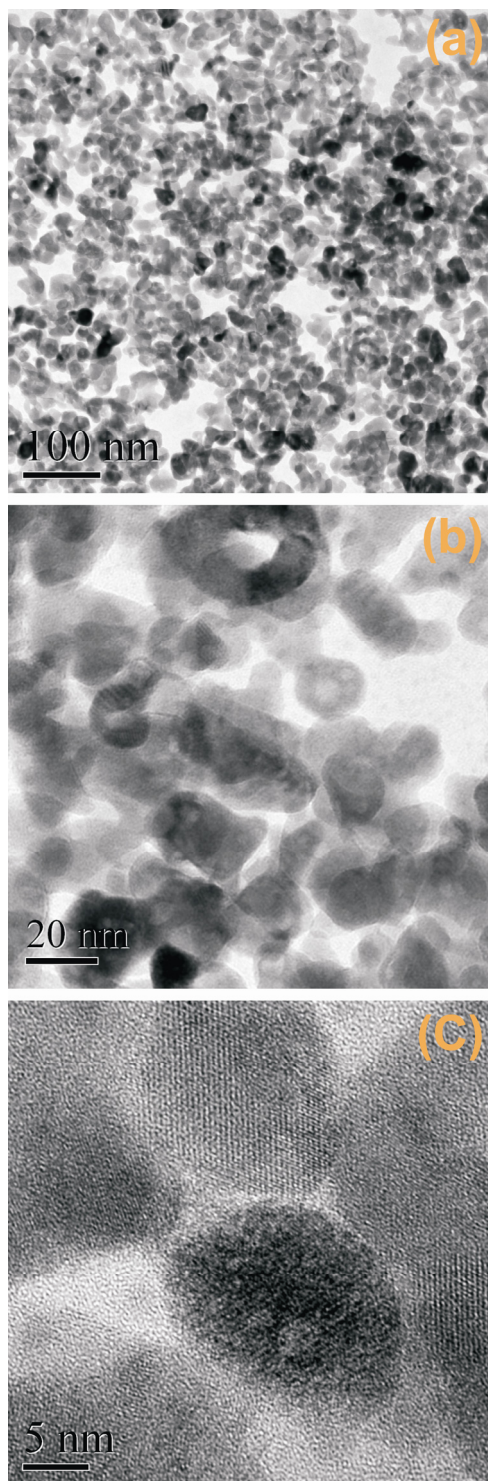


*Figure 5.5(a-c) Conventional bright-field TEM image of the ITO nanoparticles showing a very narrow particle size distribution*



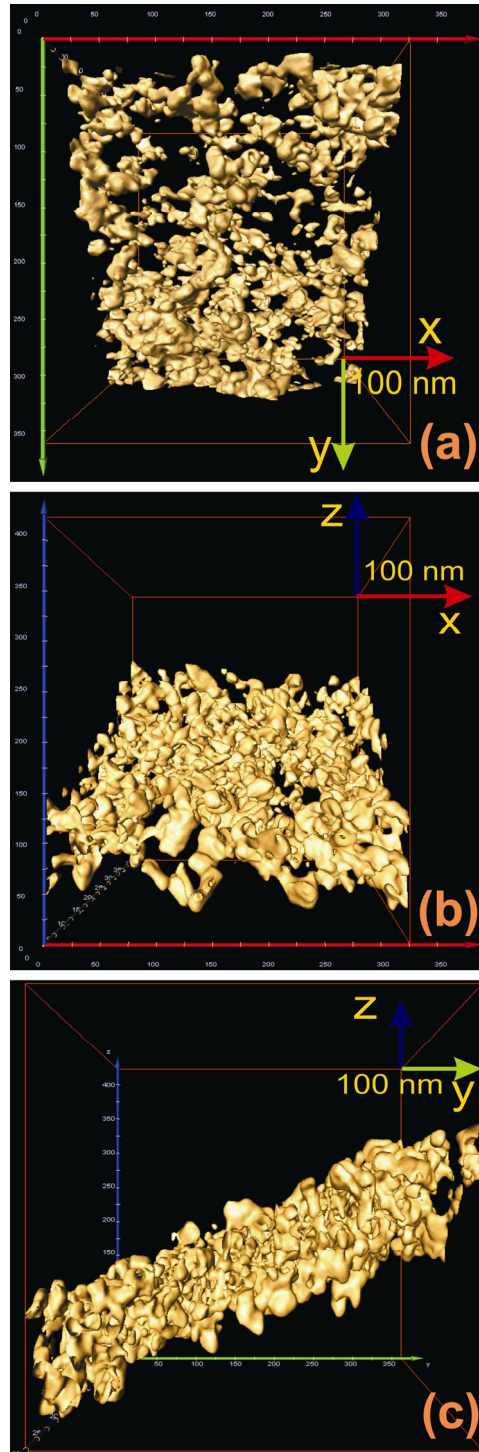


Figure 5.6(a-c) Surface rendering of the ITO nanoparticles in the binarized and reconstructed tomography images with  $xy$ ,  $xz$  and  $yz$  planes facing the plane of the paper, respectively. The thickness of the spin coated film ( $120 \pm 10$  nm) can be estimated from Fig. 5.5c

The reconstructed images with different coordinates facing the plane of the paper are shown in Fig. 5.6(a-c). Quantitative analysis was performed using the program MAVI (Modular Algorithms for Volume Images). MAVI affords a characterization of 3-D

structures by analysis of their representations as binary and spatially discrete images [Ohs00]. Table 5.1 summarizes the result obtained from volume analysis of the tomography images. No particle growth is observed to occur during the annealing in air. This has also been observed for ITO nanoparticles by other authors [Ede03a, Ede03b]. The thickness of the ITO channel of  $120 \pm 10$  nm, measured by profilometry is confirmed by the tomography image (5.6b-c).

*Table 5.1 Morphological data of the ITO nanoparticles from volume analysis of the tomography images*

Sample	Region of Interest (nm)	Porosity (%)	Specific surface area per unit volume ( $\mu\text{m}^{-1}$ )	Mean chord length (Average particle size) (nm)	Mean chord length pore space (Avg. pore size) (nm)
Sample area 1	215×165×110	$85 \pm 1$	45	$13.4 \pm 1$	$75 \pm 1$
Sample area 2	240×135×80	$83 \pm 1$	50	$14.3 \pm 1$	$64.5 \pm 1$

### ***5.3.2 Electrochemistry and transport measurements***

All the measurements were performed at room temperature. Similar to the thin film experiments, a careful selection of the adsorption-free, predominantly capacitive, potential region was performed with a slow ( $5 \times 10^{-4}$  Vs<sup>-1</sup>) cyclo-voltammetry, to avoid chemical reaction at the nanoparticle/electrolyte interface. In our device structure the area of the contact leads is many orders of magnitude higher than the channel area (ITO nanoparticles), therefore a cyclovoltammogram of the device would only show the charging current from the leads and not from the nanoparticles. In order to determine the electrochemical behavior of the nanoparticles alone, a slow scan cyclo-voltammetry was carried out for ITO nanoparticles coated onto a glass substrate (area 25 mm x 25 mm) (Fig. 5.7). The accumulated charge was determined by integrating the charging current. The open circuit potential (OCP) was determined through the zero current chronopotentiometry as -0.15 V with respect to the Ag/AgCl reference electrode.

It has already been mentioned that the electrochemical cell within the capacitive region can be compared with a resistor-capacitor ( $RC$ ) circuit where the time constant,  $\tau$ , is proportional to  $RC$ . The slow reversal of the charging current at the positive or negative potential extremes is therefore caused by a high relaxation time due

to the low conductivity of the polymer electrolyte and a high capacitance (as a result of very high surface area) of the nanoparticulate electrode.

The potential window (gate voltage) used was therefore limited within this capacitive region as shown in Fig. 5.7 for all the experiments performed. The resistance variation of the ITO channel transistor with respect to a slow scan cyclovoltammogram ( $5 \times 10^{-4} \text{ Vs}^{-1}$ ) is shown in Fig. 5.8. A constant current of 100 nA was applied between the drain and source and the potential drop across two terminals was measured. A change in resistance by more than three orders of magnitude was observed (Fig. 5.8) when the potential of the ITO nanoparticles (working electrode) was varied between -0.45 and 0.65 V ( $V_g = -0.65$  to 0.45 V) with respect to the Ag/AgCl reference electrode (Fig. 5.7).

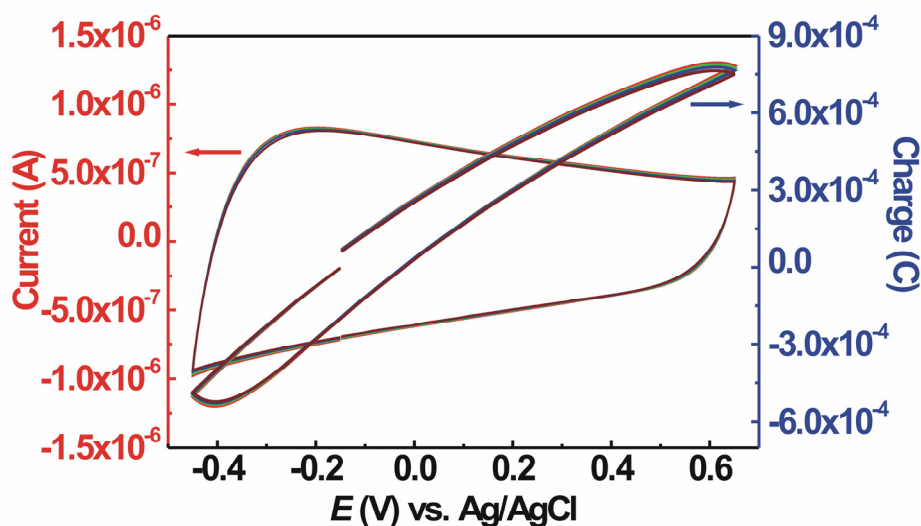


Figure 5.7 Cyclovoltammogram of the dispersed ITO nanoparticles prepared by spin-coating under identical conditions as used for the actual device

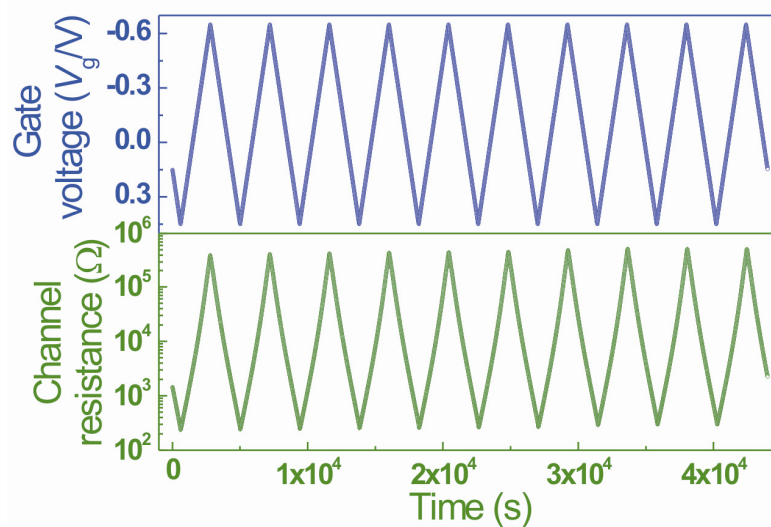


Figure 5.8 Change in resistance of the ITO channel with the gate voltage varied with a constant rate of  $5 \times 10^{-4} \text{ V/s}$

At the negative potential applied to the ITO channel, (positive gate potential) positive ions (i.e.  $\text{K}^+$  ions) come close to the surface of the ITO nanoparticles. As a result, electrons in the ITO nanoparticles are attracted towards the surface to build the charge double layer. Therefore, a positive gate potential increases the carrier (electron) concentration of the ITO nanoparticles resulting in a decrease of the resistance of the channel. In case of positive electrode potential (negative gate potential), negative ions (i.e.  $\text{F}^-$ ) form the charge double layer which repels the electrons away from the surface-electrolyte interfaces, i.e. the electron density of the channel decreases. Furthermore, as discussed in the previous chapter a charge-induced variation in electron scattering at the surface of the nanoparticle and at the inter-particle necks must be playing a decisive role towards the observed change in channel resistance.

Overall, it is clear that the positive or negative ions build the electrostatic double layer at the solid/electrolyte interface and hence work like a gate dielectric to deplete or accumulate charge carriers and alter their mobility. The channel gets narrower and broader with the negative and positive gate voltage, respectively. Therefore this electrochemical double-layer charging of the nanoparticle surface is analogous to the dielectric gating and the nanoparticulate-film device is similar to a normally-on junction field effect transistor (JFET).

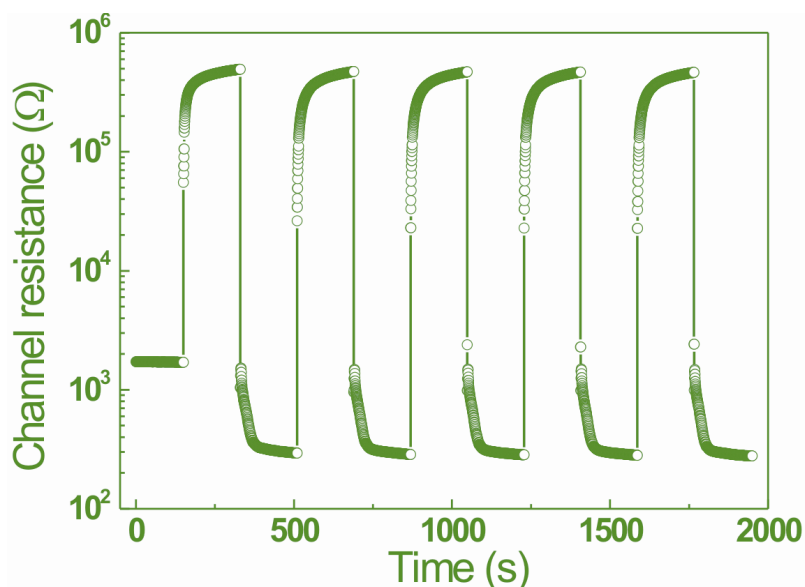


Figure 5.9 Change in the channel resistance in response to potential pulses between the gate and channel applied periodically

Fig. 5.9 shows the response of the device with the gate potential switched between 0.45 and -0.65 V. The resistance of the channel is measured at 100 ms time intervals. This experiment was performed to estimate tentatively the response time (Switching speed) of the device. From Fig 5.9 it is seen that the characteristic charging time (time to charge a capacitor by 63.2%), ( $RC$ ), is in the order of measurement frequency (i.e., 100 ms). Therefore, it is thus clear from the equivalent circuit of an electrochemical cell (Fig. 2.2) that a decrease in the resistance of the electrolyte or the capacitance of the electrode would be necessary for a faster switching. From Fig. 5.8 and Fig. 5.9 it can be noticed that varying the electrode potential within a predominantly adsorption-free capacitive double layer region (field-effect), as opposed to a carrier injection by redox reaction, (electrochemical doping) results in a good repeatability of the device performance.

The transfer characteristic (input = gate voltage; output = drain current) of the device is shown in Fig 5.10. The rate of change of the drain current is observed to be fairly constant over the entire range of gate voltage. In case of electrochemical field-effect the applied charge (field) depends on the double layer capacitance (DLC) of the particle/electrolyte interface. Therefore, the observed phenomenon (nearly constant rate of change of drain current with varying gate potential) can be explained by assuming a continuous decrease in DLC with the decrease in carrier concentration in the channel from positive to negative gate bias.

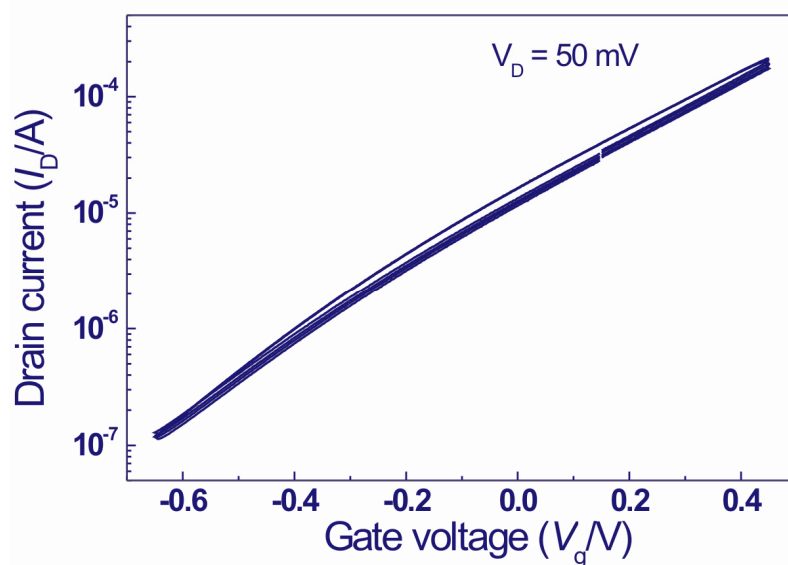


Figure 5.10 Transfer characteristics of the solid polymer electrolyte-gated transistor

In accordance with the above explanation, Fig. 5.7 shows a decrease in the charging current towards the positive electrode (negative gate) potential. Similar differential capacitance values with different electrode potentials have been previously reported for CdSe nanocrystals [Yud03].

Fig. 5.11 shows the  $I-V$  characteristic of the device. The gate voltage is varied between 0.15 to -0.45 V while the drain voltage is varied between 5 mV to a maximum of 800 mV. The saturated drain current larger than 200  $\mu\text{A}$  observed for gate voltage  $V_g = +150$  mV is extremely high for a thin film transistor [Sun07]. The *pinch-off* voltage in a field-effect transistor is defined as the voltage which is necessary to pinch off the current or to block the channel. In other words, if voltage across the drain to source voltage ( $V_D$ ) is increased to a level that its further increase does not change the drain to source current ( $I_D$ ), this characteristic voltage is referred to as pinch-off voltage. This term originates from the physical phenomenon that with an increase in  $V_D$  the depleted region in a JFET eventually reaches to equilibrium where the width of the undepleted channel determines the current. Hence, further increase in drain voltage does not lead to any increase in drain current. The pinch-off voltage for each gate potential can be determined from Fig. 5.10. It may be noted that the width of the channel can therefore be calculated from the pinch-off voltage. The pinch-off voltage at zero gate bias is thus utilized later in the study to calculate the inter-particle neck diameter.

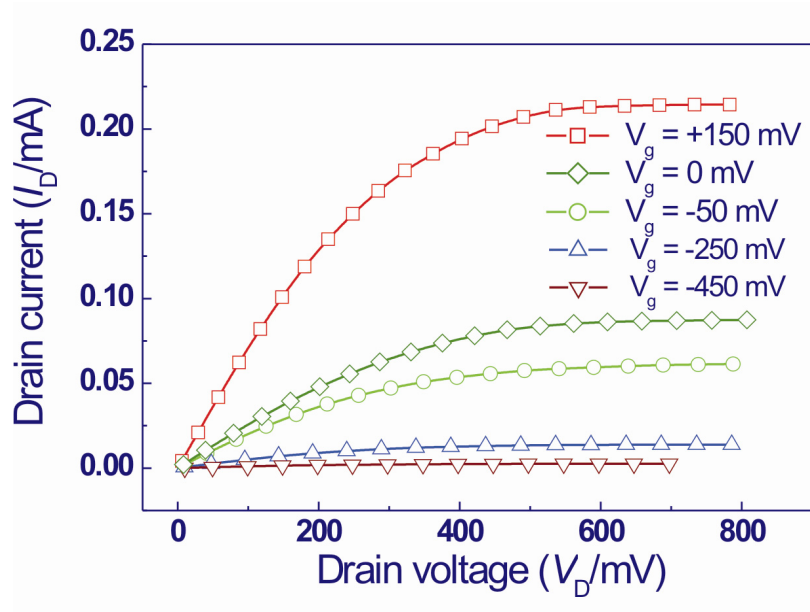


Figure 5.11 Drain current – drain voltage characteristic of the device with the gate voltage varied between 150 to -450 mV

When the gate voltage in JFET is applied between the gate and source the current flowing through the insulator (dielectric) from the gate to the source is called the gate leakage. The gate leakage in the present device is the non capacitive current flowing between the counter electrode (gate) and the channel. In other words the surface reactions, if any, on the surfaces of the nanoparticles comprising the channel would result in a leakage similar to the gate leakage in a thin film transistor (TFT) stack. To quantify this leakage the drain and source current for the same drain and gate voltage were measured separately. Fig. 5.12 shows the drain- and source-current vs. gate-voltage from 20 to 100 mV drain-voltages, respectively. The difference between these two plots gives us the value of gate leakage in the present device (Fig. 5.13). From Fig. 5.13 it is possible to conclude that the gate leakage is always more than two orders of magnitude lower than the drain-source current for the entire gate and drain voltage combinations.

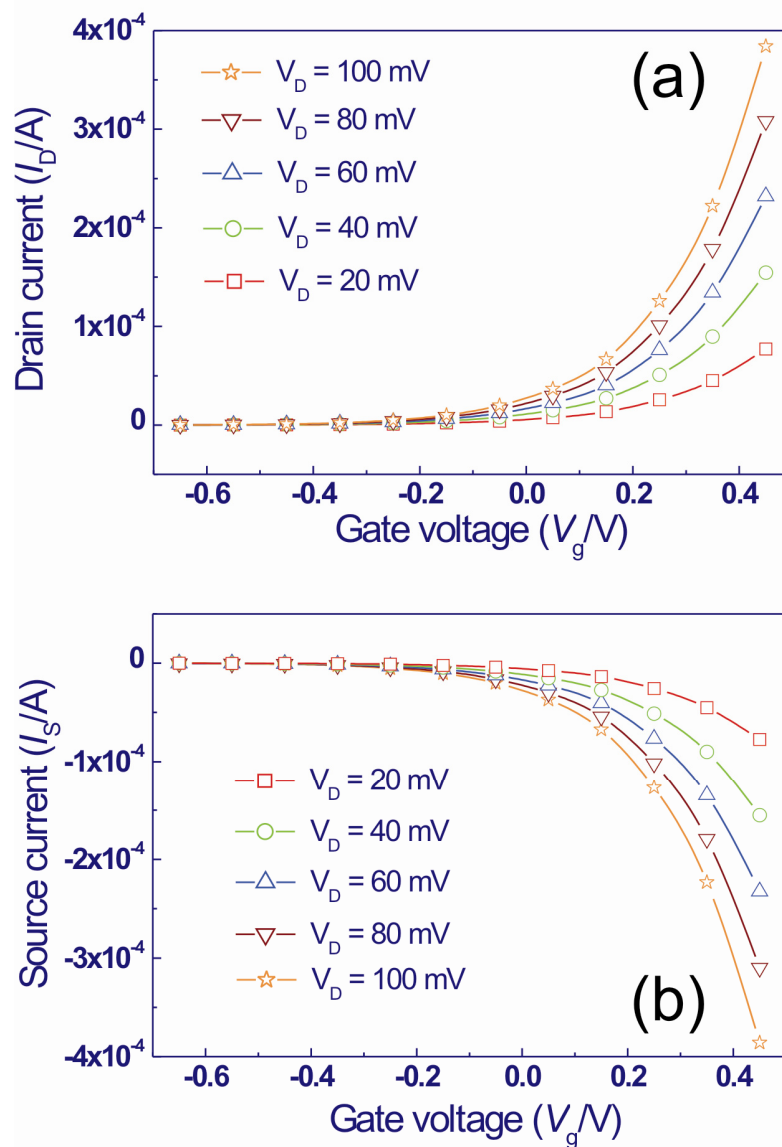


Figure 5.12 (a) The drain current and (b) source current measured at different gate ( $V_g = 450$  to  $-650$  mV) and drain voltage ( $V_D = 20$  to  $100$  mV)



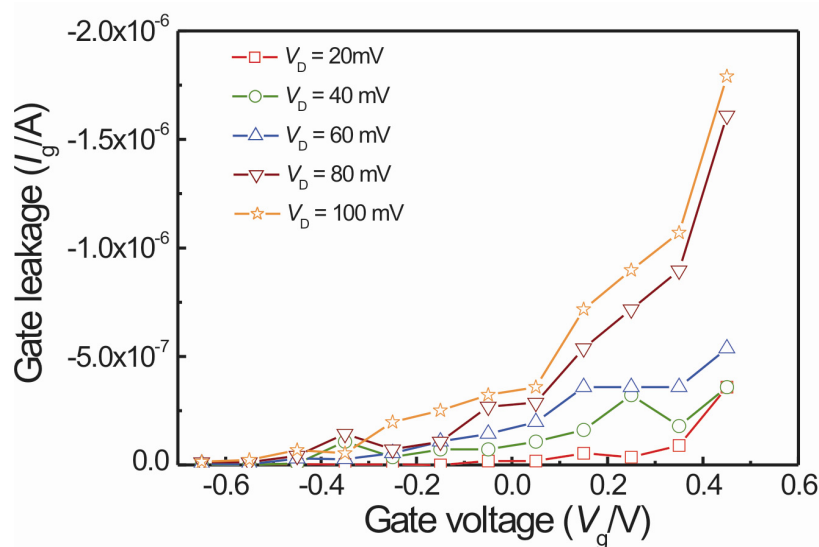


Figure 5.13 Gate leakage of the device at different gate voltage

### 5.3.3 Calculation of the field-effect mobility

The switching speed of a transistor is the inverse to the time required to switch between ON state and OFF state. The field-effect mobility ( $\mu_{FE}$ ) is the parameter which generally determines the switching speed. The field-effect mobility can have a different value than the intrinsic carrier mobility of the channel material because the electron drift velocity may change with the applied field. Therefore  $\mu_{FE}$  would also depend on the intensity of the applied field (surface/interface charge density). Here we show that the large surface charge concentration at the ITO nanoparticle surfaces coupled with their high intrinsic carrier mobility results in high field-effect mobility in our device, however, the switching speed is limited by the mobility of the ions in the polymer electrolyte, i.e., by the time necessary to apply the capacitive charge on the nanoparticle surfaces.

The equation to calculate the field effect mobility given by Sze [Sze81] for the abrupt-junction long-channel JFET is based on the thin film geometry with a gate dielectric placed on one side of the semiconductor film. This geometry, however, does not describe the situation of the present nanoparticulate channel and consequently, cannot be applied for the determination of the field-effect mobility. Moreover, the electrical field in the present study is not applied from just one side but surrounds the nanoparticulate system as the electrolyte penetrates the voids/nanopores. Therefore as a first approximation, the channel is thought to be composed of parallel nanowires (Fig. 5.14). The equation given by Sze is modified to fit the nanowire geometry where the electric field/gate surrounds the circumference of the nanowires. A good approximation of the effective number of nanowires along the channel is possible using the essential parameters, such as particle size ( $\sim 15$  nm) and porosity (0.83) (i.e. pore to particle volume ratio) as obtained from the mathematical analysis of the tomography images.

Therefore, the current passing through one of such nanowire can be calculated from the experimentally obtained saturated drain-current through the entire channel divided by the number of parallel wires/paths.

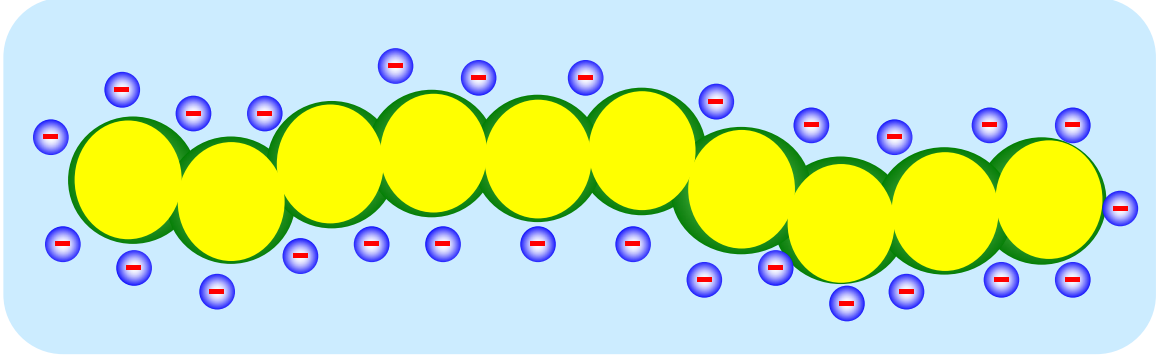


*Figure 5.14 Schematic drawing of the nanowire approximation of the nanoparticulate channel. The pinching of the interparticle necks occurs when ions come close to the particles (at negative gate potential) determines the pinch-off voltage.*

Assuming the gate dielectric surrounds the entire circumference of the nanowires, the drain current through such a nanowire channel can be written as

$$I_D = \pi q N_D \mu_{FE} \left( \frac{dV}{dx} \right) (a - h)^2 \quad (5.1)$$

where,  $I_D$  is the drain current,  $q$  is the electronic charge,  $N_D$  is the carrier concentration in the channel,  $\mu_{FE}$  is the field-effect mobility,  $a$  is the radius of the nanowire and  $h$  is the depletion depth from the surface.

Solving two dimensional Poisson equation,

$$\frac{\partial^2 V}{\partial h^2} + \frac{1}{h} \frac{\partial V}{\partial h} = -\frac{q N_D}{\epsilon} \quad (5.2)$$

With  $h \rightarrow a$  when  $V \rightarrow V_p$  we get,

$$V_p = \frac{q N_D}{4\epsilon} a^2 \quad (5.3)$$

where,  $V_p$  is the pinch-off potential,  $\epsilon$  is the dielectric constant of ITO.

Therefore, integrating equation (5.1),

$$I_D = \frac{Aa^4}{L} \left[ \frac{1}{2} \frac{V_D}{V_P} - \frac{2}{3} \left\{ \left( \frac{V_g + V_D}{V_P} \right)^{3/2} - \left( \frac{V_g}{V_P} \right)^{3/2} \right\} + \frac{1}{4} \left( \frac{V_D + 2V_g}{V_P} \right) \left( \frac{V_D}{V_P} \right) \right] \quad (5.4)$$

where,  $A = \mu_{FE} \pi \frac{q^2 N_D^2}{2\epsilon}$ ,  $V_D$  is the drain voltage,  $V_g$  is the gate voltage and  $L$  is the length of the channel. The value of the carrier density [Ede05] and static dielectric constant [Fra82, Ham83] used in the calculation are  $1.8 \times 10^{20} \text{ cm}^{-3}$  and 9, respectively. Therefore, at zero gate bias the saturated drain current is given by

$$I_{DSS} = \frac{Aa^4}{12L} \quad (5.5)$$

The average neck diameter is ( $\sim 5 \text{ nm}$ ) calculated from the experimentally observed pinch-off potential using equation (5.3) lies within the range expected from the tomography images. This value of the neck diameter is used in equation (5.5) for the mobility calculation. All potentials in this work are referred to the Ag/AgCl reference electrode. Thus it can be noted that the values of applied potential will change considerably with the change of the reference electrode. Therefore, the saturated drain current at zero gate bias ( $I_{DSS}$ ) is taken as the drain current at open circuit potential (OCP). The selection of this potential as zero gate bias is justified because of the very small build-in potential at OCP as confirmed from the small change in resistance compared to the dry sample, i.e. without an electrolyte. The calculated field-effect mobility ( $\mu_{FE}$ ) from equation (5.5) is  $24.3 \text{ cm}^2/\text{Vs}$ . This number is comparable with the intrinsic carrier mobility ( $20\text{-}60 \text{ cm}^2/\text{Vs}$ ) of ITO nanoparticles as reported by Edarth *et al.* [Ede03a, Ede05, Ede03b]. However, as mentioned previously, owing to the slow response of the electrochemical gating, which determines the switching speed in the present device, a high field-effect mobility of the channel is of lesser importance unless a fast switching can be realized by improving the electrolyte conductivity and device geometry.

The calculated saturated drain current at zero gate bias, ( $I_{DSS}/W$ ) of  $5.5 \text{ }\mu\text{A}/\mu\text{m}$  signifies high on-state current. Transconductance ( $g_m = \frac{\partial I_D}{\partial V_g}$ ), measures the ratio of the change in output current with a change in input voltage. High value ( $22 \text{ mS mm}^{-1}$ ) of specific transconductance ( $g_m/W$ ) of the device is again due to the metallic conductivity of the channel. Another important device parameter which leads to low power operation is the subthreshold swing ( $S$ ). It is defined as the gate voltage required to change the drain-source current ( $I_D$ ) by one order of magnitude. A small subthreshold swing is therefore favored for the low power operation of the transistors [Zha06]. The  $S$  value in the present device varies between  $230$  and  $425 \text{ mV dec}^{-1}$  for the positive and negative

extreme of the gate voltage, respectively. This is comparable to the best values of  $S$  reported for printable/flexible TFTs [Sun07].

An inorganic nanoparticulate channel field-effect device (JFET) has been demonstrated to work with solid electrolyte gating. The large change in channel resistance observed for such a metal-like channel can be explained in the light of a major change in charge carrier mobility/electron mean free path in line with the understanding obtained for the ITO thin films (Chapter Three). These kinds of entirely solution-processed devices are of importance in the field of low-cost electronics which can be printed from roll-to-roll. The use of the solid electrolyte as a gate made it possible to obtain a large field-effect mobility compared to nanoparticle channel devices with dielectric gating reported in the literature [Tal05, Cui05]. This is may be the first report of a nanoparticle channel transistor device with such large field-effect mobility; larger than most of the solution processed organic semiconductor channel devices reported in the literature. However, due to the slow movement of the ions in the polymeric matrix the response time of the device is rather long. A much larger switching speed would be necessary to realize all kinds of possible application, for instance, a  $100 \times 100 \times 10$  (area  $\times$  depth) pixel video display would require a minimum processing speed of 1 MHz for a 10 frames/s refresh rate. Therefore, further engineering developments are necessary to improve the response time of the device. The next chapter will offer a short summary of the state of the art of printable electronics and suitability of the device in this area of applications.

## Chapter 6

# Relation to future application: Printable electronics

### 6.1 PRINTABLE ELECTRONICS

Printable electronics (PE) may be defined as the electronic circuits and devices that can be prepared using existing printing technologies. Printable electronics have gained increasing commercial interest for “low-tech” applications with a lesser demand for performance compared to the existing high-performance electronics. Therefore, PE differs considerably from the traditional high performance Si single crystal electronics (microelectronic), where progress is primarily driven towards the reduction of critical dimensions in order to increase the speed and computing capacity. Using inexpensive materials and production methods applications are expected in areas such as logic, RFID chips, sensory skins, LED displays, LED lights, electrophoretic and electrochromic displays, photovoltaic panels, fuel cells, printable batteries, membrane keyboard, smart packaging, electronic textiles, toys and greetings cards etc. This type of electronics (sometimes referred to as macroelectronics) is typically fabricated on rigid or flexible substrates such as glass, polymer sheets etc. However, other type of rollable, bendable, wearable, biodegradable substrates such as textiles, papers have also been considered [Sun07]. Printing of transistors and logic gates with different printing techniques such as screen printing, ink jet, dry printing etc. has been proposed and also demonstrated in the literature [Sun07]. It may be very important to note that the market in printable electronics is expected to expand rapidly in coming years and this in turn results in a much larger ongoing activity in this area than commonly appears in the research articles.

## 6.2 STATE OF THE ART

Although the applications demand printed logic on a variety of different substrates so far the reports mainly include PE on glass and plastic substrates. Thin Film Transistors (TFT) with organic semiconductor channels have been favored in the past for their suitability in direct printing. Ink-jet printing of polymer TFTs has shown tremendous progress in recent years [Sir00, Kim04, Son07]. High mobility organic semiconductors with field effect mobilities of the order of  $10 \text{ cm}^2/\text{Vs}$  have been reported recently [Mic07, Nis06, Tak07, Pod03]. Although studied widely, most of the plastic electronic materials are unstable in air and quickly degrade their performance [Ser04]. As an alternative, inorganic materials have also being considered. It is often said that the options are rather limited with the inorganics, whereas the organics are *future-proof*. However, it can be undoubtedly stated that the performance of the inorganic devices in terms of a good efficiency, longer life-time, high mobility, electronic property and cost effectiveness is far superior till date than the organic devices [Har09]. It is of course understandable that the better printability would be the most important factor at the end and the organic inks are easily printable, however, the nanoparticle dispersions of inorganic materials may be an answer to this problem. Large activity is going on to produce conductive printable inks for passive structure of the devices. Nanoparticle dispersions of various metals [Hon00] and also ITO inks are being considered [Hon08]. Owing to the vast area of possible applications it is however clear that all these organic, inorganic, hybrid and also the partially printable devices may find applications in different fields needing different novelty [Das09b].

Concurrent research activities in the inorganic devices which may find applications as printable or partially printable electronics encompass the following areas:

- a) Zinc oxide devices [For04, Lee07]: This is the largest area of activity in inorganic semiconductor devices. ZnO thin films [Sun07], nanoparticulate [Oka08] and nanowire devices [Sun07] are being considered. Transistors with large field-effect mobility are reported in the literature.
- b) Amorphous and single-crystalline channel devices from InGaZnO [Naj08, Nom03].
- c) High-mobility silicon devices: solution processed silicon films [Shi06] ( $6.5 \text{ cm}^2/\text{Vs}$ ) and single-crystalline silicon ribbons [Men04, Lee05] with very high field-effect mobility ( $180 \text{ cm}^2/\text{Vs}$ ). The microcrystalline silicon devices [Men04], obtained from transfer printing, hold large promise for future applications [Nan07].
- d) Metal chalcogenide devices [Rid99, Mit04]: Field-effect mobility of the order of  $10 \text{ cm}^2/\text{Vs}$  has been reported.
- e) Nanowire devices [Sun07]: Although a very good performance has been shown [Jus07] problems with large scale production and self assembly limit their application as cheap electronics.

- f) Metal oxide nanoparticle devices [Tal05, Cui05]: Surprisingly, so far the metal oxide nanoparticle devices have not gained large attention yet. PbSe [Tal05] and  $\text{In}_2\text{O}_3$  [Cui05] nanocrystalline channels have shown very low mobility values.

### 6.3 SUITABILITY OF THE PRESENT DEVICE: STRENGTHS AND LIMITATIONS

In chapter five, a field-effect transistor device consisting of conducting nanoparticle as a channel material and a solid polymer electrolyte as gate dielectric is demonstrated [Das08b]. As a step forward, an ink-jet printing of the solid polymer electrolyte in our laboratory with a *Dimatix DMP 2831* ink-jet printer has been performed. Fig. 6.1 shows 200 and 50 micron dots of the polymer electrolyte printed in the liquid state and subsequently dried on a PMMA coated glass substrate. Our efforts have been encouraged by the ink-jet printing of the Indium Tin Oxide (ITO) nanoparticles which has been demonstrated recently by Hong *et al.* [Hon08]. The purpose of their work was to show the possibility of ink-jet printing of a high conducting film with greater than 90% optical transparency. The process temperature was reported as 300 °C. Therefore, the possibility of an all-printed solid state transistor device with an appreciable performance can be foreseen at the present state.

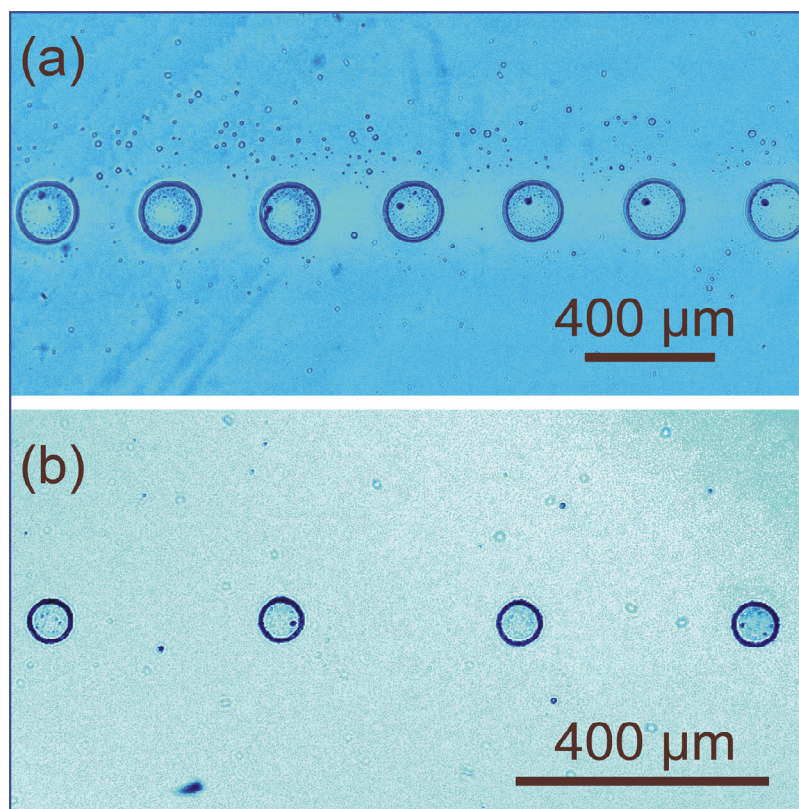


Figure 6.1 Ink-jet printed solid polymer electrolyte (PVA+H<sub>2</sub>O+KF) on PMMA (A4 950K) coated glass substrate; (a) 200×200 μm, (b) 50×50 μm dots

The strengths of the present device include:

- I. Higher environmental stability and long-term performance can be ensured compared to the organic TFTs.
- II. The working principle of the device is based on capacitive double layer charging (field effect). The gate potential is varied within the predominantly capacitive double layer window and precautions were taken to minimize the surface chemistry (redox reaction). This should result in a high reproducibility and longer life time.
- III. The gel-polymer electrolyte is mechanically stable and reports confirm that no degradation was observed for a time period of two years.
- IV. High field-effect mobility.
- V. Easy device fabrication.



- VI. Quality dispersion is not required. Generally a nanoparticle dispersion of extremely high quality is required for printed electronics to ensure a smooth interface between channel and dielectric. However, in case of the present device type, dispersions with larger agglomerate size would not degrade the device performance as the electrolyte penetrates the nanopores and the surface charge / electric field surrounds the surface of each individual nanoparticle and the necks between them.
- VII. Low gate voltage requirement ( $< 1$  V).

The current limitation of the device is its high switching time. Large field-effect mobility is therefore of lesser importance as the switching speed is governed by the ionic mobility of the electrolyte. In the present device, the switching time is the characteristic time ( $RC$ ) necessary to apply sufficient charge at the nanoparticle surface. The resistance of the electrolyte can however be improved either by an addition of nanoparticle ceramic fillers into the polymeric matrix [Yan06] or by placing the gate (i.e., the counter electrode) at the close proximity of the channel. On the other hand, it is believed that the capacitance of the device can be lowered by many orders of magnitude easily. As stated in chapter four, in the present device, the electrolyte was solution casted over the entire device [channel and electrodes (Source and Drain)]. Therefore a very large capacitance resulted from the large macroscopic electrodes (Source and Drain). Hence, a straightforward decrease in capacitance by orders of magnitude can be expected when the electrolyte is printed (as shown in Fig. 6.1) only on top of the channel and not solution casted on the macroscopically large passive structures (Fig. 5.4).

## 6.4 OPTIMIZATION OF THE PRESENT DEVICE TOWARDS INDUSTRIAL NEEDS

The processing temperature of the device demonstrated in chapter four was 550 °C. However, for practical applications a device has to be printed on polymer substrates and therefore the processing temperature should not be higher than 150-200 °C. If an organic stabilizer is used to obtain better quality dispersion with lower average agglomerate size, the post annealing temperature after spin-coating/printing usually has to be higher in order to ensure the removal of the functionalizing agents. However, in case of the present device high quality dispersion in terms of small agglomerate size is not required because the electrolyte would anyway penetrate the nanopores to reach the entire accessible primary particle surface.

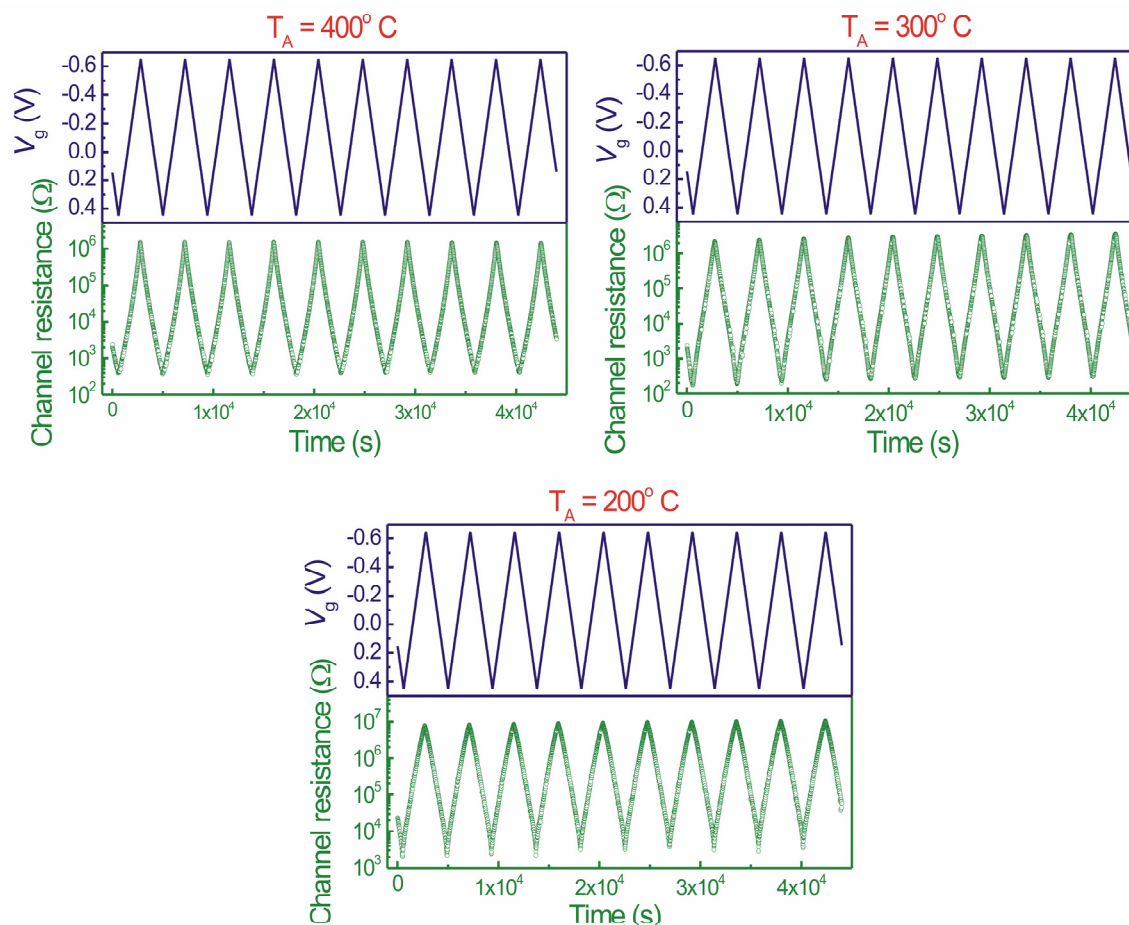


Figure 6.2 Variation in channel resistance for polymer electrolyte gated ITO transistors with varying post annealing temperature

Table 6.1 Change in on/off ratio of the ITO-polymer electrolyte transistor with the variation in the post-annealing temperature

Sample	Stabilizer	Annealing Temperature	On/off Ratio
ITO_550_17.11.07	Yes	550 °C	$2 \times 10^3$
ITO_400_01.07.08	No	400 °C	$4 \times 10^3$
ITO_300_01.07.08	No	300 °C	$1 \times 10^4$
ITO_200_01.07.08	No	200 °C	$5 \times 10^3$

Therefore, a dispersion with 15 wt.% of ITO nanoparticles in iso-propanol was prepared with ultrasonic agitation. This nanoparticle loading of 15 wt.% of ITO was found to show the best film quality in terms of a minimum sheet resistance after spin

coating and baking at 150 °C. It was noticed that in absence of an organic stabilizer the post annealing temperature could be reduced to 200 °C. Fig. 6.2 summarizes the results for different devices with different post annealing temperatures. A trend towards a minor increase in effect-size, although not very clear, can be seen from the on/off ratios listed in table 6.1. This can result from differences in annealing temperature which has two effects towards the change in effect-size, however, acting in opposite direction.

a) A decrease in carrier concentration should result with increase in temperature of annealing performed in air. The lower initial carrier concentration should lead to an increase in on/off ratio.

b) A nominal increase in average neck diameter may be expected with an increase in annealing temperature and this in turn should relate to more and more inefficient depletion of carriers at the interparticle necks. Since it is concluded that the screening of the charge carriers at the interparticle necks are playing the major role in the field-effect observed, an increase in annealing temperature would therefore also decrease the on/off ratio.

The trend in the variation of on/off ratio with respect to the annealing temperature observed (Table 6.1) is therefore due to the above mentioned counter acting effects.

It may be concluded that the realization of an all-printed device is clearly feasible. The performance, the transistor characteristics and the switching speed of the device need to be further improved for better suitability in industrial applications.



## Chapter 7

# Conclusions and outlook

### 7.1 CONCLUSIONS

The major findings of the research covered in this thesis can be summarized as follows:

- I. A reversible variation in resistance up to 1.9% for a pure metal (Au) under electrochemical double-layer charging is observed. A quantitative theoretical model is presented to account for the total observed effect. It is considered that the surface charge is screened within a very short distance inside a metal. Furthermore, a change in the shape of the electron density profile occurs at the surface and not a variation in carrier concentration inside the bulk. This surface charge-induced movement of the electron density profile results in a small shift of the centre of mass of the density profile. The theoretical model presented in this work assumes this shift of the centre of mass of the electron density profile normal to the charged surface as a variation in effective thickness of the thin film. Therefore, two contributions towards resistance modulation arise from this effect: a) the change in the effective thickness of the film, and b) a variation in the surface scattering resulting from the change in effective thickness.
- II. From the analysis of the experimental result and the model proposed in the work, it is believed that the non-linearity in the resistance variation of a metal electrode under electrochemical charging may be related to the non-linear relationship of the shift of electron density profile at different sign of surface charge and doesn't necessarily signify an onset of a chemical reaction at the metal/electrolyte interface.

- III. Similar to the pure metal (Au), electrochemical surface charge induced electrical resistance modulation is measured for degenerately doped semiconductor (Indium Tin Oxide, ITO) thin films. Reversible variation in resistance for the nominal film thickness of as low as 3.6 nm is measured within a chemical reaction free capacitive potential window. Compared to Au, a much more noticeable increase and decrease in resistance by +203% and 40%, respectively is observed for the thinnest film.
- IV. It is shown that only a small fraction (10%) of the observed increase in resistance modulation can be explained by the change in carrier density upon charging.
- V. The scanning tunneling microscopy images show a fine substructure on the grains which is believed to be due to variation in local density of states. It is also observed from the scanning tunneling spectroscopy that the spectra taken on the grain boundaries show the presence of larger concentration of surface states than the spectra taken on the grains. The origin of these rich surface states can be related to higher free volume, Sn dopant segregation and oxidation near the grain boundary. This in turn results in a reduced carrier concentration at the grain boundaries. A larger band bending observed in the spectra taken at grain boundaries also corroborate the above conclusion.
- VI. The grains are electronically rough as seen from the STM images and the grain boundaries contain lower number of carriers; thereby with the application of large surface charge at the thin film/electrolyte interface the grains will get electronically even rougher (increase in electronic surface roughness) and the applied field would penetrate deeper along the grain boundaries disrupting the conduction paths disrupted. Consequently a decrease in surface specularly leading to a larger surface scattering and a pronounced grain boundary scattering would result. It is believed that this surface charge induced tuneable modulation in electron scattering/mobility is responsible for the large field-effect observed in highly conducting oxides, such as ITO.
- VII. It is shown that a large field-effect in polycrystalline nanostructures of oxide conductors is possible despite their metallic conductivity. The dopant segregation and oxidation of the grain boundaries make it feasible to tune the electron mobility to a large extent via an applied electrostatic field.
- VIII. The concept is transferred from the ITO thin films to ITO nanoparticles and resulted in a change in resistance of four orders of magnitude.
- IX. A solution processed, easy-to-fabricate, low voltage junction field-effect transistor (JFET) device prepared with ITO nanoparticles as a channel and solid polymer electrolyte as gate dielectric shows appreciable transistor characteristics.

- X. The calculated field effect mobility ( $\mu_{FE} = 24.3 \text{ cm}^2/\text{Vs}$ ) is fairly high when compared with the existing solution-processed devices. However, the switching speed of the device is found to be limited by the conductivity of the ions within the polymer electrolyte.
- XI. A reduction in process temperature to 200 °C is demonstrated. A low working temperature increases the feasibility of the device to be fabricated over various substrates.

## 7.2 OUTLOOK

- I. At the present state the switching speed of the transistor device is large. However, it may be foreseen that an increase in conductivity of the polymer electrolyte and a better design of the transistor geometry can decrease the switching time of the device by orders of magnitude. The ionic conductivity of the polymer electrolyte can be enhanced by an addition of ceramic ( $ZrO_2$ ,  $SiO_2$ ) nanoparticle fillers into it.
- II. It is important to demonstrate an all-printed device where the nanoparticle channel and the polymer electrolyte both are printed using an ink-jet printer.
- III. Conducting oxide nanowires can also be used as the active material. The reduction in surface area of the device with the use of nanowire-channel should decrease the device capacitance and hence decrease the switching time.
- IV. From the understanding of surface charge-induced tuneable electron mobility leading to large field-effect, it is possible to envision even more interesting results in systems where electron mean free path is much larger than in a heavily doped semiconductor (Heavy doping enhances scattering at dopants and limits the electron mean free path to several nanometer). Along this line undoped indium oxide nanostructures will be an excellent system of interest.
- V. A metallic single-wall carbon nanotube (SWCNT) can be gated similarly with the solid polymer electrolyte used in the present study. As mentioned earlier in the thesis, an electrolyte can exert orders of magnitude higher local field compared to the best known dielectric. Therefore there may be a possibility of an electrochemically-gated field-effect device with the metallic nanotubes as the channel material.



## References

- [Agn78] O. P. Agnihotri, A. K. Sharma, B. K. Gupta, R. Thangaraj, "The effect of tin additions on indium oxide selective coatings" J. Phys. D: Appl. Phys., 11 (1978) 643
- [Ala00] M. J. Alam, D.C. Cameron, "Optical and electrical properties of transparent conductive ITO thin films deposited by sol-gel process" Thin Solid Films, 377-378 (2000) 455
- [And73a] W. J. Anderson, W. N. Hansen, "Observing the electrochemical interphase *via* electrode surface conductance" Electroanal. Chem. and Interfacial Electrochem., 43 (1973) 329
- [And73b] W. J. Anderson, W. N. Hansen, "Electroreflectance and conductance" Electroanal. Chem. and Interfacial Electrochem., 47 (1973) 229
- [Aud03] N. Audebrand, S. Raite, D. Louër, "The layer crystal structure of  $\text{In}_2(\text{C}_2\text{O}_4)_3(\text{H}_2\text{O})_3 \cdot 7\text{H}_2\text{O}$  and microstructure of nanocrystalline  $\text{In}_2\text{O}_3$  obtained from thermal decomposition" Solid State Sci., 5 (2003) 783
- [Ban84] D. J. Bannister, G. R. Davies, I. M. Ward, J. E. McIntyre, "Ionic conductivities for poly(ethylene oxide) complexes with lithium salts of monobasic and dibasic acids and blends of poly(ethylene oxide) with lithium salts of anionic polymers" Polymer, 25 (1984) 1291
- [Ban07] C. Bansal, S. Sarkar, A. K. Mishra, T. Abraham, C. Lemier, H. Hahn, "Electronically tunable conductivity of a nanoporous Au-Fe alloy" Scripta Mater., 56 (2007) 705
- [Bau86] E. Bauer, J. H. van der Merwe, "Structure and growth of crystalline superlattices: from monolayer to superlattice" Phys. Rev. B, 33 (1986)

## REFERENCES

- 3657
- [Bec92] D. D. Beck, R. W. Siegel, "The dissociative adsorption of hydrogen-sulfide over nanophase titanium dioxide" *J. Mater. Res.*, 7 (1992) 2840
- [Ben78] R. Benz, "Electrical conductivity of  $\text{PbF}_2$ " *Z. Phys. Chem. Frankfurt*, 95 (1975) 25
- [Ber71] A. Berman, H. J. Juretschke, "Origin of the electric field-effect in silver" *Appl. Phys. Lett.*, 18 (1971) 417
- [Bes96] F. Besenbacher, "Scanning tunneling microscopy studies of metal surfaces" *Rep. Prog. Phys.*, 59 (1996) 1737
- [Bir84] R. Birringer, H. Gleiter, H. -P. Klein, P. Marquardt, "Nanocrystalline materials: An approach to a novel solid structure with gas-like disorder?" *Phys. Lett.*, 102A, (1984) 365
- [Boe95] D. K. G. de Boer, A. J. G. Leenaers, W. W. van den Hoogenhof, "Glancing-incidence X-ray analysis of thin-layered materials: a review" *X-ray Spectrometry*, 24 (1995) 91
- [Bru84] P. G. Bruce, A. R. West, "Ion trapping and its effect on the conductivity of LISICON and other solid electrolytes" *J. Solid State Chem.*, 53 (1984) 430
- [Bru95] P. G. Bruce (Editor), "Solid state electrochemistry" Cambridge university press (1995) p. 7, 74, 95
- [Byo03] E. Byon, T. W. H. Oates, A. Anders, "Coalescence of nanometer silver islands on oxides grown by filtered cathodic arc deposition" *Appl. Phys. Lett.*, 82 (2003) 1634
- [Che02] X. J. Chen, K. A. Khor, S. H. Chan, L. G. Yu, "Influence of microstructure on the ionic conductivity of yttria-stabilized zirconia electrolyte" *Mater. Sci. Engg. A*, 335 (2002) 246
- [Com23] A. H. Compton, *Phil. Mag.*, 45 (1923) 1121
- [Cui05] T. Cui, Y. Liu, M. Zhu, "Field-effect transistors with layer-by-layer self-assembled nanoparticle thin films as channel and gate dielectric" *Appl. Phys. Lett.*, 87 (2005) 183105
- [Cul59] B. D. Cullity, "Elements of X-ray diffraction", Addison-Wesley Publishing Company, Inc. London, England (1959)
- [Das08a] S. Dasgupta, R. Kruk, D. Ebke, A. Hütten, C. Bansal, H. Hahn, "Electric

- field induced reversible tuning of resistance of thin gold films” *J. Appl. Phys.*, 104 (2008) 103707
- [Das08b] S. Dasgupta, S. Gottschalk, R. Kruk, H. Hahn, “A nanoparticulate indium tin oxide field-effect transistor with solid electrolyte gating” *Nanotechnology*, 19 (2008) 435203
- [Das09a] S. Dasgupta, M. Lukas, K. Dössel, R. Kruk, H. Hahn, “Electron mobility variations in surface-charged indium tin oxide thin films” *Phys. Rev. B*, 80 (2009) 085425
- [Das09b] R. Das, P. Harrop, “Printed, organic & flexible electronics forecasts, players & opportunities 2009-2029” [www.IDTechEx.com](http://www.IDTechEx.com)
- [Dri06] H. Drings, R. N. Viswanath, D. Kramer, C. Lemier, J. Weissmüller, R. Würschum, “Tuneable magnetic susceptibility of nanocrystalline palladium” *Appl. Phys. Lett.*, 88 (2006) 253103
- [Dur00] C. Durkan, M. E. Welland, “Size effects in the electrical resistivity of polycrystalline nanowires” *Phys. Rev. B*, 61 (2000) 14215
- [Dzh91] P. G. Dzhavakhidze, A. A. Kornyshev, A. Leibsch, M. I. Urbakh, “Theory of the second harmonic generation at the metal/electrolyte interface” *Electrochem. Acta*, 36 (1991) 1835
- [Dzh92] P. G. Dzhavakhidze, A. A. Kornyshev, A. Leibsch, M. Urbakh, “Theory of second-harmonic generation at the metal-electrolyte interface” *Phys. Rev. B*, 45 (1992) 9339
- [Eck05] J. Eckert, U. Kuhn, J. Das, S. Scudino, N. Radtke “Nanostructured composite materials with improved deformation behavior” *Adv. Engg. Mater.*, 7 (2005) 587
- [Ede85] J. Ederth, A. Hultåker, G. A. Niklasson, P. Heszler, A. R. van Doorn, M. J. Jongerius, D. Burgard, C. G. Granqvist, “Thin porous indium tin oxide nanoparticle films: effects of annealing in vacuum and air” *Appl. Phys. A*, 81 (2005) 1363
- [Ede03a] J. Ederth, P. Johnsson, G. A. Niklasson, A. Hoel, A. Hultåker, P. Heszler, C. G. Granqvist, A. R. van Doorn, M. J. Jongerius, D. Burgard, “Electrical and optical properties of thin films consisting of tin-doped indium oxide nanoparticles” *Phys. Rev. B*, 68 (2003) 155410
- [Ede03b] J. Ederth, G. A. Niklasson, A. Hultåker, P. Heszler, C. G. Granqvist, A. R. van Doorn, M. J. Jongerius, D. Burgard, “Characterization of porous indium tin oxide thin films using effective medium theory” *J. Appl. Phys.*,

## REFERENCES

- 93 (2003) 984
- [Eno91] H. Enoki, J. Echigoya, H. Suto, "The intermediate compound in the  $\text{In}_2\text{O}_3$ - $\text{SnO}_2$  system" *J. Mater. Sci.*, 26 (1991) 4110
- [Erl04] J. Erlebacher, "An atomistic description of dealloying porosity evolution, the critical potential, and rate-limiting behavior" *J. Electrochem. Soc.*, 151 (2004) C614
- [Fee94] R. M. Feenstra, "Tunneling spectroscopy of the (110) surface of direct-gap III-V semiconductors" *Phys. Rev. B*, 50 (1994) 4561
- [Fra76] G. Frank, L. Brock, H. D. Bausen, "The solubility of Sn in  $\text{In}_2\text{O}_3$  and of In in  $\text{SnO}_2$  crystals grown from Sn-In melts" *J. Cryst. Growth*, 36 (1976) 179
- [Fra82] G. Frank, H. Köstlin, "Electrical-properties and defect model of tin-doped indium oxide layers" *Appl. Phys. A*, 27 (1982) 197
- [Fra92] J. Frank, "Electron tomography: Three-dimensional imaging with the transmission electron microscope" Plenum Press, New York, (1992)
- [Fre07] M. S. Freund, B. A. Deore, "Self doped conducting polymers" John Wiley & Sons Ltd, England (2007)
- [For79] A. J. Forty, "Corrosion micromorphology of noble metal alloys and depletion gilding" *Nature*, 282 (1979) 597
- [For04] E. Fortunato, A. Pimentel, L. Pereira, A. Gonçalves, G. Lavareda, H. Águas, I. Ferreira, C. N. Carvalho, R. Martins "High field-effect mobility zinc oxide thin film transistors produced at room temperature" *J. Non Cryst. Solids*, 338-340 (2004) 806
- [Fuc38] K. Fuchs, "The conductivity of thin metallic films according to the electron theory of metals" *Proc. Camb. Phil. Soc.*, 34 (1938) 100
- [Gan89] S. Ganapathiappan, K. Chen, D. F. Shriver, "Synthesis, characterization, and electrical response of phosphazene polyelectrolytes" *J. Am. Chem. Soc.*, 111 (1989) 4091
- [Gas06] Y. Gassenbauer, R. Schafranek, A. Klein, S. Zafeiratos, M. Hävecker, A. Knop-Gericke, R. Schlögl, "Surface states, surface potentials, and segregation at surfaces of tin-doped  $\text{In}_2\text{O}_3$ " *Phys Rev. B*, 73 (2006) 245312
- [Gha80] K. P. Ghatak, A. K. Choudhury, S. Ghosh, A. N. Chakravarti, "Temperature dependence of the Debye screening length in heavily

- doped semiconductors having Gaussian band-tails” Czech. J. Phys. B, 30 (1980) 925
- [Gie86] P. Gies, R. R. Gerhardts, “Self-consistent calculation of electron-density profiles at strongly charged jellium surfaces” Phys. Rev. B, 33 (1986) 982
- [Gie03] F. J. Giessibl, “Advances in atomic force microscopy” Rev. Mod. Phys., 75 (2003) 949
- [Gil72] P. Gilbert, “Iterative methods for the three-dimensional reconstructions of an object from projections” J. Theor. Biol., 36 (1972) 105
- [Gle89] H. Gleiter, “Nanocrystalline materials” Prog. Mater. Sci., 33 (1989) 223
- [Gle00] H. Gleiter, “Nanocrystalline materials: Basic concepts and microstructure” Acta Mater., 48 (2000) 1
- [Gle01a] H. Gleiter, J. Weissmüller, O. Wollersheim, R. Würschum, “Nanocrystalline materials: A way to solids with tunable structures and properties?” Acta Mater., 49 (2001) 737
- [Gle01b] H. Gleiter, “Tuning the electronic structure of solids by means of nanometer-sized microstructures” Scripta Mater., 44 (2001) 1161
- [Gle08] H. Gleiter, “Our thoughts are ours, their ends none of our own: Are there ways to synthesize materials beyond the limitations of today?” Acta Mater. 56 (2008) 5875
- [Goo76] J. B. Goodenough, H. Y. -P. Hong, J. A. Kafalas, “Fast Na<sup>+</sup>-ion transport in skeleton structures” Mater. Res. Bull., 11 (1976) 203
- [Gre95] A. L. Greer, “Metallic glasses” Science, 267 (1995) 1947
- [Gup89] L. Gupta, A. Mansingh, P. K. Srivastava, “Band gap narrowing and the band structure of tin doped indium oxide films” Thin Solid Films, 176 (1989) 33
- [Ham83] I. Hamberg, C. G. Granqvist, “Dielectric function of undoped In<sub>2</sub>O<sub>3</sub>” Thin Solid Films, 105 (1983) L83
- [Han87] P. K. Hansma, J. Tersoff, “Scanning tunneling microscopy” J. Appl. Phys., 61 (1987) R1
- [Har09] P. Harrop, R. Das, “Inorganic and composite printed electronics 2009-2019” www.IDTechEx.com
- [Hen99] M. E. McHenry, M. A. Willard, D. E. Laughlin, “Amorphous and

## REFERENCES

- nanocrystalline materials for applications as soft magnets” *Prog. Mater. Sci.*, 44 (1999) 291
- [Hon00] C. M. Hong, S. Wagner, “Inkjet printed copper source/drain metallization for amorphous silicon thin-film transistors” *IEEE Elect. Dev. Lett.*, 21 (2000) 384
- [Hon08] S. -J. Hong, Y. -H. Kim, J. -I. Han, “Development of ultrafine indium tin oxide (ITO) nanoparticle for ink-jet printing by low-temperature synthetic method” *IEEE Trans. Nanotechnol.*, 7 (2008) 172
- [Irv66] E. C. McIrvine, “Comment on the ferroelectric-polarization field effect” *Phys. Rev.*, 148 (1966) 528
- [Iwa86] H. Iwahara, H. Uchida, S. Tanaka, “High temperature-type proton conductive solid oxide fuel cells using various fuels” *J. Appl. Electrochem.*, 16 (1986) 663
- [Jac89] P. W. M. Jacobs, J. W. Lorimer, A. Russer, M. Wasiucioneck, “Phase relations and conductivity in the system poly(ethylene oxide)-LiClO<sub>4</sub>” *J. Power Sources*, 26 (1989) 503
- [Jar97] G. Jarzqbek, Z. Borkowska, “On the real surface area of smooth solid electrodes” *Electrochem. Acta*, 42 (1997) 2915
- [Jil03] D.C. Jiles, “Recent advances and future directions in magnetic materials” *Acta Mater.*, 51 (2003) 5907
- [Jin08] H. -J. Jin, S. Parida, D. Kramer, J. Weissmüller, “Sign-inverted surface stress-charge response in nanoporous gold” *Surf. Sci.*, 602 (2008) 3588
- [Joh86] W. L. Johnson, “Thermodynamic and kinetic aspects of the crystal to glass transformation in metallic materials” *Prog. Mater. Sci.*, 30 (1986) 81
- [Jus07] S. Ju, A. Facchetti, Y. Xuan, J. Liu, F. Ishikawa, P. Ye, C. Zhou, T. J. Marks, D. B. Janes, “Fabrication of fully transparent nanowire transistors for transparent and flexible electronics” *Nature Nanotechnol.*, 2 (2007) 378
- [Kas97] S. Kasiviswanathan, V. Srinivas, A. K. Kar, B. K. Mathur, K. L. Chopra, “Observation of deviation of electronic behavior of indium tin oxide film at grain boundary using scanning tunneling microscope” *Solid State Comm.*, 101 (1997) 831
- [Kee76] M. O’keeffe, B. G. Hyde, “The solid electrolyte transition and melting in

- salts” *Phil. Mag.*, 33 (1976) 219
- [Kem85] K. Kempa, “Importance of nonlocal effects for the evaluation of static screening at a Au Surface from ellipsometry” *Surface Sci.*, 157 (1985) L323
- [Kel04] T. W. Kelley, P. F. Baude, C. Gerlach, D. E. Ender, D. Muires, M. A. Haase, D. E. Vogel, S. D. Theiss, “Recent progress in organic electronics: Materials, devices, and processes” *Chem. Mater.*, 16 (2004) 4413
- [Kie31] H. Kiessig, “Interferenz von Röntgenstrahlen an dünnen Schichten” *Ann. der Phys.*, 5 (1931) 769
- [Kim01] J. H. Kim, G. Yang, S. yang, A. H. Weiss, “Study of the growth and stability of the ultra-thin film of Au deposited on Si(100) and Si(111)” *Surface Sci.*, 475 (2001) 37
- [Kim04] Y. H. Kim, D. G. Moon, J. I. Han, “Organic TFT array on a paper substrate” *IEEE Elect. Dev. Lett.*, 25 (2004) 702
- [Kit96] C. Kittel, “*Introduction to Solid State Physics*” 7<sup>th</sup> ed. (Wiley, New York, 1996)
- [Koe75] H. Köstlin, R. Jost, W. Lems, “Optical and electrical properties of doped In<sub>2</sub>O<sub>3</sub> films” *Phys. Stat. Sol. (a)*, 29 (1975) 87
- [Kra04] D. Kramer, R. N. Viswanath, J. Weissmüller, “Surface-stress induced macroscopic bending of nanoporous gold cantilevers” *Nano Lett.*, 4 (2004) 793
- [Kum03] K.S. Kumar, H. Van Swygenhoven, S. Suresh, “Mechanical behavior of nanocrystalline metals and alloys” *Acta Mater.*, 51 (2003) 5743
- [Lee04] D. Y. Lee, S. -K. Song, S. -K. Koh, H. -K. Baik, K. M. Song, “Initial growth characterization of Au thin films on SnO<sub>x</sub> substrate by *in situ* conductivity measurement” *Electrochem. Soc.*, 151 (2004) G890
- [Lee05] K. J. Lee, M. J. Motala, M. A. Meitl, W. R. Childs, E. Menard, A. K. Shim, J. A. Rogers, R. G. Nuzzo, “Large-area, selective transfer of microstructured silicon: A printing-based approach to high-performance thin-film transistors supported on flexible substrates” *Adv. Mater.*, 17 (2005) 2332
- [Lee07] D. H. Lee, Y. J. Chang, G. S. Herman, C. H. Chang, “A general route to printable high-mobility transparent amorphous oxide semiconductors” *Adv. Mater.*, 19 (2007) 843
- [Lew00] A. Lewandowski, K. Skorupska, J. Malinska “Novel poly (vinyl alcohol)-

## REFERENCES

- KOH-H<sub>2</sub>O alkaline polymer electrolyte” *Solid State Ionics*, 133 (2000) 265
- [Lin04] Z. Q. Li, J. J. Lin, “Electrical resistivities and thermopowers of transparent Sn-doped indium oxide films” *J. Appl. Phys.*, 96 (2004) 5918
- [Luc65] M. S. P. Lucas, “Electrical conductivity of thin metallic films with unlike surfaces” *J. Appl. Phys.*, 36 (1965) 1632
- [Maa94] A. I. Maarooof and B. L. Evans, “Onset of electrical conduction in Pt and Ni films” *J. Appl. Phys.*, 76 (1994) 1047
- [Man69] C. K. Mann, “Electroanalytical Chemistry” Dekker, New York, vol. 3 (1969) p. 57
- [Mat05] F. Matino, L. Persano, V. Arima, D. Pisignano, R. I. R. Blyth, R. Cingolani, R. Rinaldi, “Electronic structure of indium-tin-oxide films fabricated by reactive electron-beam deposition” *Phys. Rev. B*, 72 (2005) 085437
- [May59] H. Mayer, *Structure and Properties of Thin Films*, Wiley, New York, (1959), p. 233.
- [May69] A. F. Mayadas, M. Shatzkes, J. F. Janak, “Electrical resistivity model for polycrystalline films - case of specular reflection at external surfaces” *Appl. Phys. Lett.*, 14 (1969) 345
- [May70] A. F. Mayadas, M. Shatzkes, “Electrical resistivity model for polycrystalline films: the case of arbitrary reflection at external surface” *Phys. Rev. B*, 1 (1970) 1382
- [Men04] E. Menard, K. J. Lee, D. -Y. Khang, R. G. Nuzzo, J. A. Rogers, “A printable form of silicon for high performance thin film transistors on plastic substrates” *Appl. Phys. Lett.*, 84 (2004) 5398
- [Mey92] E. Meyer, “Atomic force microscopy” *Prog. Surf. Sci.*, 41 (1992) 3
- [Mic07] A. P. Micolich, L. L. Bell, A. R. Hamilton, “An improved process for fabricating high-mobility organic molecular crystal field-effect transistors” *J. Appl. Phys.*, 102 (2007) 084511
- [Mis08] A. K. Mishra, C. Bansal, H. Hahn, “Surface charge induced variation in the electrical conductivity of nanoporous gold” *J. Appl. Phys.*, 103 (2008) 094308
- [Mit04] D. B. Mitzi, L. L. Kosbar, C. E. Murray, M. Copel, A. Afzali “High-mobility ultrathin semiconducting films prepared by spin coating”



- Nature, 428 (2004) 299
- [Moe01] W. Mönch, “*Semiconductor Surfaces and Interfaces*”, 3<sup>rd</sup> ed. Springer Series in Surface Science Vol. 26 (Springer, Berlin, 2001) 4<sup>th</sup> Ch.
- [Mor00] H. Morikawa, H. Kurata, M. Fujita, “On the grain boundary segregation of Sn in indium-tin-oxide thin films” J. Electron Microsc., 49 (2000) 67
- [Mry01] O. N. Mryasov, A. J. Freeman, “Electronic band structure of indium tin oxide and criteria for transparent conducting behavior” Phys. Rev. B, 64 (2001) 233111
- [Muk95] S. Mukerjee, S. Srinivasan, M. P. Soriaga, J. McBreen, “Role of structural and electronic properties of Pt and Pt alloys on electrocatalysis of oxygen reduction” J. Electrochem. Soc. 142 (1995) 1409
- [Nad98] N. Nadaud, N. Lequeux, M. Nanot, “Structural Studies of Tin-Doped Indium Oxide (ITO) and  $\text{In}_4\text{Sn}_3\text{O}_{12}$ ” J. Solid State Chem., 135 (1998) 140
- [Naj08] J. H. Na, M. Kitamura, Y. Arakawa, “High field-effect mobility amorphous InGaZnO transistors with aluminum electrodes” Appl. Phys. Lett., 93 (2008) 063501
- [Nak79] O. Nakamura, T. Kodama, I. Ogino, Y. Miyake, “High-conductivity solid proton conductors - dodecamolybdophosphoric acid and dodecatungstophosphoric acid crystals” Chem. Lett., 1 (1979) 17
- [Nan07] Nano-031 “Opportunities for nanocrystalline silicon and silicon inks in electronics” [www.nanomarkets.net](http://www.nanomarkets.net)
- [Nis96] K. Nishio, T. Sei, T. Tsuchiya, “Preparation and electrical properties of ITO thin films by dip-coating process” J. Mater. Sci., 31 (1996) 1761
- [Nis06] J. Nishide, T. Oyamada, S. Akiyama, H. Sasabe, C. Adachi, “High field-effect mobility in an organic thin-film transistor with a solid-state polymerized polydiacetylene film as an active layer” Adv. Mater., 18 (2006) 3120
- [Nom03] K. Nomura, H. Ohta, K. Ueda, T. Kamiya, M. Hirano, H. Hosono “Thin-film transistor fabricated in single-crystalline transparent oxide semiconductor” Science, 300 (2003) 1269
- [Nor08] D. J. Norris, A. L. Efros, S. C. Erwin, “Doped nanocrystals” Science, 319 (2008) 1776
- [Oat03] T. W. H. Oates, PhD thesis “Metal plasma immersion ion implantation

## REFERENCES

- and deposition using polymer substrates”, 2003.
- [Oat04] T. W. H. Oates, D. R. McKenzie, M. M. M. Bilek, “Percolation threshold in ultrathin titanium films determined by *in situ* spectroscopic ellipsometry” *Phys. Rev. B*, 70 (2004) 195406
- [Oda01] H. Odaka, Y. Shigesato, T. Murakami, S. Iwata, “Electronic structure analysis of Sn doped  $\text{In}_2\text{O}_3$ ” *Jpn. J. Appl. Phys.*, 40 (2001) 3231
- [Ohs00] J. Ohser, F. Mücklich, *Statistical Analysis of Microstructures in Materials Science*, John Wiley & Sons, Chichester, 2000, Ch. 3-4.
- [Oka08] K. Okamura, N. Mechau, D. Nikolova, H. Hahn, “Influence of interface roughness on the performance of nanoparticulate zinc oxide field-effect transistors” *Appl. Phys. Lett.*, 93 (2008) 083105
- [Oze05] T. Ozel, A. Gaur, J. A. Rogers, M. Shim, “Polymer electrolyte gating of carbon nanotube network transistors” *Nano Lett.*, 5 (2005) 905
- [Pan05] M. J. Panzer, C. D. Frisbie, “Polymer electrolyte gate dielectric reveals finite windows of high conductivity in organic thin film transistors at high charge carrier densities” *J. Am. Chem. Soc.*, 127 (2005) 6960
- [Pan06] M. J. Panzer, C. D. Frisbie, “High carrier density and metallic conductivity in poly (3-hexylthiophene) achieved by electrostatic charge injection” *Adv. Funct. Mater.*, 16 (2006) 1051
- [Pan07] M. J. Panzer, C. D. Frisbie, “Polymer electrolyte-gated organic field-effect transistors: low-voltage, high-current switches for organic electronics and test beds for probing electrical transport at high charge carrier density” *J. Am. Chem. Soc.*, 129 (2007) 6599
- [Par06] S. Parida, D. Kramer, C. A. Volkert, H. Rösner, J. Erlebacher, and J. Weissmüller, “Volume change during the formation of nanoporous gold by dealloying” *Phys. Rev. Lett.*, 97 (2006) 035504
- [Pau58a] L. J. van der Pauw, “A method of measuring specific resistivity and hall effect of discs of arbitrary shape” *Philips Res. Rep.*, 13 (1958) 1
- [Pau58b] L. J. van der Pauw, “A method of measuring the resistivity and hall coefficient on lamellae of arbitrary shape” *Philips Tech. Rev.*, 20 (1958) 220
- [Pen02] H. Peng, N. Machida, T. Shigematsu, “Preparation of silver ion conducting amorphous materials in the system  $\text{Ag}_2\text{S}-\text{SiS}_2$  by mechanical milling processes” *J. Mater. Chem.*, 12 (2002) 1094

- [Pli08] W. Plieth, "Electrochemistry for materials science" Elsevier (2008) Ch. 4, p. 101
- [Pod03] V. Podzorov, S. E. Sysoev, E. Loginova, V. M. Pudalov, M. E. Gershenson, "Single-crystal organic field effect transistors with the hole mobility  $\sim 8 \text{ cm}^2/\text{Vs}$ " Appl. Phys. Lett., 83 (2003) 3504
- [Pon05] J. L. Pons, "Emerging actuator technologies: A micromechatronic approach" John Wiley & Sons Ltd, England (2005)
- [Pop04] V. N. Popov, "Carbon nanotubes: properties and application" Mater. Sci. Engg. R, 43 (2004) 61
- [Rid99] B. A. Ridley, B. Nivi, J. M. Jacobson, "All-inorganic field effect transistors fabricated by printing" Science, 286 (1999) 746
- [Rie87] P. H. Rieger, "Electrochemistry" Prentice-Hall International Inc. (1987) p. 70, 104
- [Sag06] M. Sagmeister, U. Brossmann, S. Landgraf, R. Würschum, "Electrically Tunable Resistance of a Metal" Phys. Rev. Lett., 96 (2006) 156601
- [Sch84] W. Schmickler, D. Henderson, "Approximate solution for the electronic density profile at the surface of jellium" Phys. Rev. B, 30 (1984) 3081
- [Sch96] M. A. Schneider, M. Wenderoth, A. J. Heinrich, M. A. Rosentreter, R. G. Ulbrich, "Current transport through single grain boundaries: a scanning tunneling potentiometry study" Appl. Phys. Lett., 69 (1996) 1327
- [Ser04] R. F. Service, "Printable electronics that stick around" Science, 304 (2004) 675
- [Shi06] T. Shimoda, Y. Matsuki, M. Furusawa, T. Aoki, I. Yudasaka, H. Tanaka, H. Iwasawa, D. Wang, M. Miyasaka, Y. Takeuchi, "Solution-processed silicon films and transistors" Nature, 440 (2006) 783
- [Sid04] G. P. Siddons, D. Merchin, J. H. Back, J. K. Jeong, M. Shim, "Highly efficient gating and doping of carbon nanotubes with polymer electrolytes" Nano Lett., 4 (2004) 927
- [Sir00] H. Sirringhaus, T. Kawase, R. H. Friend, T. Shimoda, M. Inbasekaran, W. Wu, E. P. Woo, "High-resolution inkjet printing of all-polymer transistor circuits" Science, 290 (2000) 2123
- [Sme03] E. Smela, "Conjugate polymer actuator for biomedical application" Adv. Mater. 15 (2003) 481

## REFERENCES

- [Son52] E. H. Sondheimer, "The mean free path of electrons in metals" *Adv. in Phys.*, 1 (1952) 1
- [Son07] D. H. Song, M. H. Choi, J. Y. Kim, J. Jang, S. Kirchmeyer, "Process optimization of organic thin-film transistor by ink-jet printing of DH4T on plastic" *Appl. Phys. Lett.*, 90 (2007) 053504
- [Sto99] K. N. Stoev, K. Sakurai, "Review on grazing incidence X-ray spectrometry and reflectometry" *Spectrochim. Acta B*, 54 (1999) 41
- [Sun85] B. Sundqvist, J. Neve, Ö. Rapp, "Pressure dependence of the electron-phonon interaction and Fermi surface properties of Al, Au, bcc Li, Pb and Pd" *Phys. Rev. B*, 32 (1985) 2200
- [Sun07] Y. Sun, J. A. Rogers, "Inorganic semiconductors for flexible electronics" *Adv. Mater.*, 19 (2007) 1897
- [Sur95] C. Suryanarayana, "Nanocrystalline materials" *Int. Mater. Rev.*, 40 (1995) 41
- [Sur05] C. Suryanarayana, "Recent developments in nanostructured Materials" *Adv. Engg. Mater.*, 7 (2005) 983
- [Sze81] S. M. Sze, "Physics of semiconductor devices" 2<sup>nd</sup> Ed. (Wiley, New York, 1981)
- [Tah98] R. Bel Hadj Tahar, T. Ban, Y. Ohya, Y. Takahashi, "Electronic transport in tin-doped indium oxide thin films prepared by sol-gel technique" *J. Appl. Phys.*, 83 (1998) 2139
- [Tak78] T. Takahashi, H. Iwahara, "Oxide ion conductors based on Bismuthsesquioxide" *Mater. Res. Bull.*, 13 (1978) 1447
- [Tak07] J. Takeya, M. Yamagishi, Y. Tominari, R. Hirahara, Y. Nakazawa, T. Nishikawa, T. Kawase, T. Shimoda, S. Ogawa, "Very high-mobility organic single-crystal transistors with in-crystal conduction channels" *Appl. Phys. Lett.*, 90 (2007) 102120
- [Tal05] D. V. Talapin, C. B. Murray, "PbSe nanocrystal solids for n- and p-channel thin film field-effect transistors" *Science*, 310 (2005) 86
- [Tan05] T. Tanaka, "Multi-core model for nanodielectrics as fine structures of interaction zones" *Ann. Rep. Conf. on Electrical Insulation and Dielectric Phenomena* (2005)
- [The72] A. Theophilou, A. Modinos, "Metallic-field effect and its consequences in field emission, field ionization and the capacitance of a capacitor" *Phys.*

- Rev. B, 6 (1972) 801
- [Tos79] T. Tošić, M. Jevtić, D. Tjapkin, “Self-consistent screening length in a heavily doped semiconductor” Univ. Beograd. Publ. Elektrotehn. Fak. Ser. Mat. Fiz., 634-677 (1979) 148
- [Tri01] T. Trindade, “Nanocrystalline semiconductors: Synthesis, properties, and perspectives” Chem. Mater., 13 (2001) 3843
- [Tuc85] R. I. Tucceri, D. Posadas, “A surface conductance study of the anion adsorption on gold” J. Electroanal. Chem., 191 (1985) 387
- [Tuc90] R. I. Tucceri, D. Posadas, “The effect of surface charge on the surface conductance of silver in surface inactive electrolytes” J. Electroanal. Chem., 283 (1990) 159
- [Tuc04] R. I. Tucceri, “A review about the surface resistance technique in electrochemistry” Surface Science Reports, 56 (2004) 85
- [Val00] R.Z. Valiev, R.K. Islamgaliev, I.V. Alexandrov, “Bulk nanostructured materials from severe plastic deformation” Prog. Mater. Sci., 45 (2000) 103
- [Vep99] S. Veprek, “The search for novel, superhard materials” J. Vac. Sci. Technol. A, 17 (1999) 2401
- [Viv08] A. A. Vives (Edited), “Piezoelectric transducers and applications” 2<sup>nd</sup> Ed., Springer-Verlag Berlin Heidelberg (2008)
- [Wad83] H. Wada, M. Menetrier, A. Levasseur, P. Hagenmuller, “Preparation and ionic conductivity of new B<sub>2</sub>S<sub>3</sub>-Li<sub>2</sub>S-LiI glasses” Mater. Res. Bull., 18 (1983) 189
- [Wan04] W.H. Wang, C. Dong, C.H. Shek “Bulk metallic glasses” Mater. Sci. Engg. R, 44 (2004) 45
- [Wei66] R. N. Weiher, R. P. Ley, “Optical properties of indium oxide” J. Appl. Phys., 37 (1966) 299
- [Wei03] J. Weissmüller, R. N. Viswanath, D. Kramer, P. Zimmer, R. Würschum, H. Gleiter, “Charge-induced reversible strain in a metal” Science, 300 (2003) 312
- [Wei07] M. Weisheit, S. Fähler, A. Marty, Y. Souche, C. Poinignon, D. Givord, “Electric field-induced modification of magnetism in thin-film ferromagnet” Science, 315 (2007) 349

## REFERENCES

- [Whi71] M. S. Whittingham, R. A. Huggins, "Transport Properties of Silver Beta Alumina" *J. Electrochem. Soc.*, 118 (1971) 1
- [Wil96] D. B. Williams, C. B. Carter, "Transmission Electron Microscopy: A Textbook for Materials Science" Springer (1996)
- [Wol07] O. S. Wolfbeis (Series Editor), C. Steinem, A. Janshoff (Volume Editors), "Springer series on chemical sensors and biosensors: Piezoelectric sensors" Springer-Verlag Berlin Heidelberg (2007)
- [Yag06] J. Yang, "Analysis of piezoelectric devices" World Scientific Publishing Co. Pte. Ltd., Singapore (2006)
- [Yan06] C. -C. Yang, "Study of alkaline nanocomposite polymer electrolytes based on PVA-ZrO<sub>2</sub>-KOH" *Mater. Sci. Engg. B*, 131 (2006) 256
- [Yan08] C. -H. Yang, S.-C. Lee, T. -C. Lin, S. -C. Chen, "Electrical and optical properties of indium tin oxide films prepared on plastic substrates by radio frequency magnetron sputtering" *Thin Solid Films*, 516 (2008) 1984
- [Yon63] Y. Yoneda, "Anomalous surface reflection of X-rays" *Phys. Rev.*, 131 (1963) 2101
- [Yud03] D. Yu, C. Wang, P. Guyot-Sionnest, "*n*-Type conducting CdSe nanocrystal solids" *Science*, 300 (2003) 1277
- [Yue07] J. D. Yuen, A. S. Dhoot, E. B. Namdas, N. E. Coates, M. Heeney, I. McCulloch, D. Moses, A. J. Heeger, "Electrochemical doping in electrolyte-gated polymer transistors" *J. Am. Chem. Soc.*, 129 (2007) 14367
- [Zha06] Q. Zhang, W. Zhao, A. Seabaugh, "Low-subthreshold-swing tunnel transistors" *IEEE Elect. Dev. Lett.*, 27 (2006) 297

# Appendix

## Appendix A

Hall-coefficient measurement: Sample data sheet

Film thickness = 9 nm

Square-shaped (6 mm × 6 mm) ITO thin films were sputtered with contact masks to obtain the desired van der Pauw geometry for the Hall-measurements. The film thickness was measured with XRR. The ITO films were then placed inside the Quantum Design PPMS stage (puck). Fig. A.1 shows the stage (puck) with the ITO film and corner contacts. The point contacts at four corners were made carefully with silver glue (Hans Wolbring GmbH) and thin gold wire (50 μm diameter).

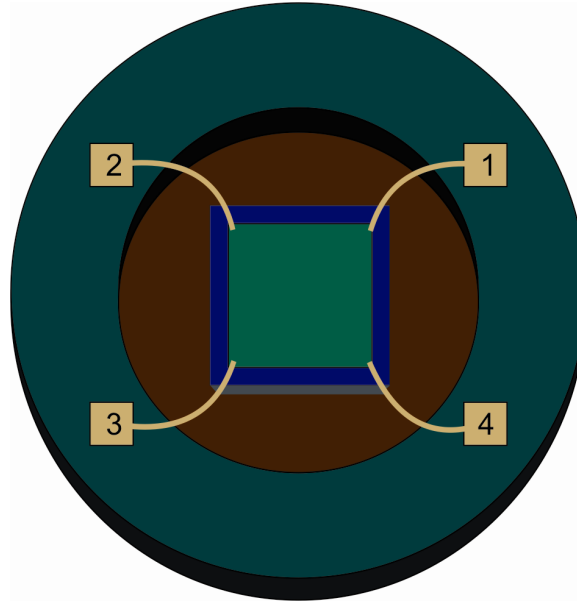


Figure A.1 Schematic of the ITO film ITO film (Green) sputtered on silicon wafer (Blue) placed inside the stage (puck).

The puck was then placed inside an extraction magnetometer (Quantum Design PPMS), for the Hall-coefficient measurement. A typical data sheet is given below.

Table A.1 Hall-voltage in micro-volt for positive and negative magnetic field and with different configuration of the applied current and measured voltage

Current (I) = 0.1 mA			
Positive field (+B) = 1 Tesla		Negative field (-B) = -1 Tesla	
Configuration	Hall-emf ( $\mu\text{V}$ )	Configuration	Hall-emf ( $\mu\text{V}$ )
$V_{24P}$	-447	$V_{24N}$	+452
$V_{42P}$	-443	$V_{42N}$	+451
$V_{13P}$	-445	$V_{13N}$	+439
$V_{31P}$	-444	$V_{31N}$	+441

$$V_C = V_{24P} - V_{24N} = -447 - 452 = -899 \mu\text{V}$$

$$V_D = V_{42P} - V_{42N} = -443 - 451 = -894 \mu\text{V}$$

$$V_E = V_{13P} - V_{13N} = -445 - 439 = -884 \mu\text{V}$$

$$V_F = V_{31P} - V_{31N} = -444 - 441 = -885 \mu\text{V}$$

$$V_C + V_D + V_E + V_F = (-899 - 894 - 884 - 885) \mu\text{V} = -3.562 \text{ mV}$$



The sum of the Hall voltages ( $V_C + V_D + V_E + V_F$ ) is negative, hence the materials is  $n$ -type.

$$\begin{aligned} \text{Therefore, } n_S &= \left| \frac{8 \times 10^{-8} IB}{e(V_C + V_D + V_E + V_F)} \right| = \left| \frac{8 \times 10^{-8} \times 10^{-4} \times 10^4}{1.602 \times 10^{-19} \times (-3.562 \times 10^{-3})} \right| \\ &= 1.4 \times 10^{14} \text{ cm}^{-2} \\ \text{and } n_0 &= \frac{n_S}{t} = \frac{1.4 \times 10^{14}}{9 \times 10^{-7}} = 1.56 \times 10^{20} \text{ cm}^{-3} \end{aligned}$$

## Appendix B

### Variation in carrier concentration of ITO thin films with electrochemical charge at the film surface

The surface charge-induced change in resistance can be explained taking two contributions into account: (A) the variation in the carrier density with surface charging, (B) the modification of carrier mobility due to a change in scattering behavior upon charging.

Hence, the resistance change can be expressed:

$$\frac{R_s}{R_{s,0}} = \left( \frac{n}{n_0} \times \frac{\mu}{\mu_0} \right)^{-1} \quad (\text{A.1})$$

If it is assumed that the surface charge-induced change in carrier mobility is not very significant as in case of a metal the above equation reduces to

$$\frac{R_s}{R_{s,0}} = \left( \frac{n}{n_0} \right)^{-1} \quad (\text{A.2})$$

Therefore, at the extreme positive and negative potential on the ITO film surfaces, the respective decrease and increase in carrier concentration can be obtained from the current integration of the cyclovoltammograms. Therefore, an expected increase and decrease in resistance can be calculated.

The instantaneous sheet carrier concentration ( $n$ ) at the extreme positive and negative surface charge is therefore  $n_s - \Delta n_s$  and  $n_s + \Delta n_s$ , respectively, and the instantaneous resistance ( $R_s$ ) at the extreme positive and negative surface charge is  $R_{s,0} + \Delta R_s$  and  $R_{s,0} - \Delta R_s$ , respectively.

Table A.2 The bulk ( $n_0$ ) and sheet ( $n_s$ ) carrier concentration, positive ( $+\Delta q$ ) and negative ( $-\Delta q$ ) surface charge density and the corresponding decrease ( $-\Delta n_s$ ) and increase ( $+\Delta n_s$ ) in sheet carrier concentration of the ITO thin films with different film thickness (for dry samples):

Film thickness (nm)	$n_0$ ( $\text{cm}^{-3}$ )	$n_s$ ( $\text{cm}^{-2}$ )	$+\Delta q$ ( $\mu\text{C}/\text{cm}^{-2}$ )	$-\Delta q$ ( $\mu\text{C}/\text{cm}^{-2}$ )	$-\Delta n_s$ ( $\text{cm}^{-2}$ )	$+\Delta n_s$ ( $\text{cm}^{-2}$ )
3.6	$6.75 \times 10^{19}$	$2.4 \times 10^{13}$	0.82	0.88	$5.52 \times 10^{12}$	$5.12 \times 10^{12}$
4.5	$9.1 \times 10^{19}$	$4.1 \times 10^{13}$	0.43	0.73	$2.68 \times 10^{12}$	$4.56 \times 10^{12}$
6	$1.3 \times 10^{20}$	$7.8 \times 10^{13}$	0.55	0.73	$3.43 \times 10^{12}$	$4.56 \times 10^{12}$
9	$1.55 \times 10^{20}$	$1.4 \times 10^{14}$	0.35	1.09	$2.18 \times 10^{12}$	$6.81 \times 10^{12}$

However, the large observed discrepancy between the experimental and the calculated value of  $R_s / R_{s,0}$  for all the films (as shown in Fig. 3.12) with different film thickness makes it obvious that equation A.2 is not valid and a large surface charge-induced modulation in carrier mobility must be present.

## Appendix C

### UV-VIS-IR spectroscopy of the ITO nanoparticles

Light absorption measurements of the ITO nanoparticles were performed using a Varian UV-VIS-NIR (Ultraviolet-visible-near infrared) spectrometer and *Spectrum Gx* FT-IR (fourier transformed infrared) spectrometer from Perkin Elmer. Figure A2 shows the photon absorption spectra of ITO nanoparticles for the range from ultraviolet ( $\lambda = 300$  nm) to infrared ( $\lambda = 8000$  nm) radiation. The ITO nanoparticles were spin coated with 3000 rpm and therefore the mean thickness of the nanoparticulate films were  $120 \pm 10$  nm as obtained from profilometry measurements and TEM tomography images (Chapter four). For the UV-VIS-NIR spectroscopy the nanoparticles were spin coated on high quality quartz glass. The nanoparticulate films for FIR (far infrared) measurements were prepared on Si wafers, Si/SiO<sub>2</sub> (200 nm) due to the better transparency of silicon in the larger wavelengths. In figure A.2 the discontinuity of the data points at  $\lambda = 2500$  nm is due to change of spectrometer and hence detector.

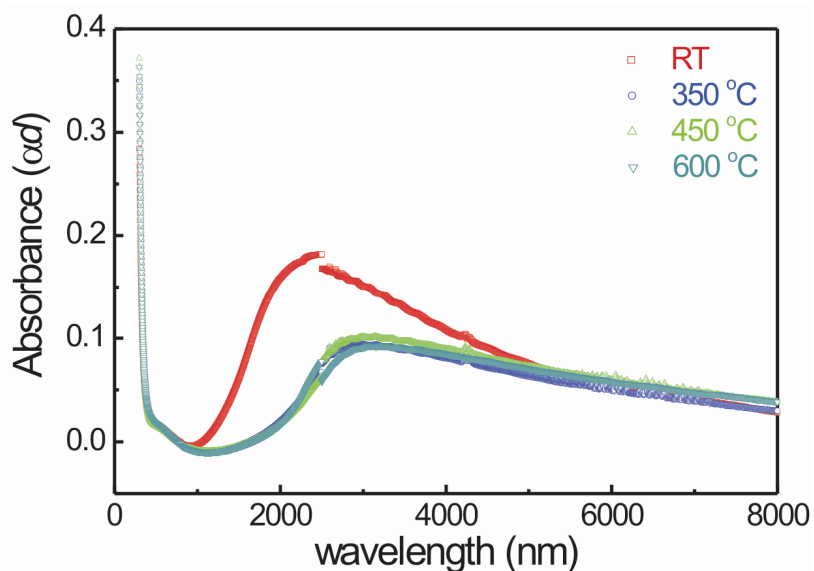


Figure A.2 Photon absorption spectra of ITO nanoparticles from ultraviolet to far infrared radiation

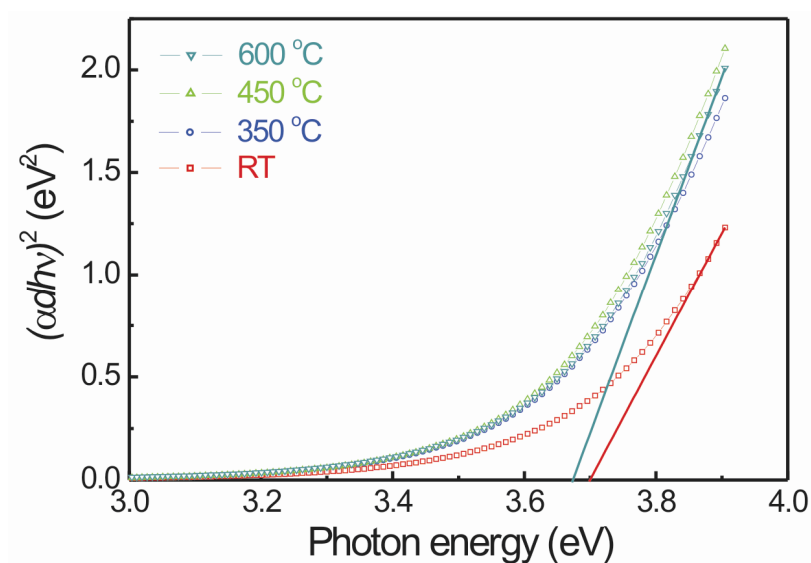


Figure A.3 Optical band gap of ITO nanoparticles with different annealing temperature (in air), obtained from  $(\alpha h\nu)^2$  vs.  $h\nu$  plot. The direct band gap is determined by extrapolating the linear part of the plot to  $\alpha = 0$ .

To determine the direct band gap of ITO nanoparticles,  $(\alpha h\nu)^2$  is plotted against the photon energy,  $(h\nu)$ , and the initial linear part of the graph is extrapolated to  $\alpha = 0$ . The value of the direct band gap ( $E_{gm}$ ) obtained for the un-annealed (RT in Fig. A.3) and 600 °C annealed samples are 3.7 eV and 3.67 eV respectively. These values matches well with the values reported in the literature [Wei66, Yan08, Gup89].

## APPENDIX

# Acknowledgement

I would like to express my sincere thanks and gratitude to all those who encouraged me and provided me with momentous assistance in making this endeavor feasible. First, I would like to thank my supervisor **Prof. Dr. Horst Hahn** for his continuous scientific input and intense encouragement throughout the whole period. I feel really grateful when I think about the amount of time he spent with me discussing my work in last three years.

Next, it should be **Dr. Robert Kruk** who was more my friend than my direct supervisor. He has got more patience than anybody I ever have seen. I am thankful to him for sharing his in-depth knowledge with me.

I would also like to thank **Dr. Maya Lukas** for her help with STM and STS measurements, **Dr. Harald Rösner** for his support with transmission electron microscopy, and **Simone Dehm** for her help in e-beam lithography. I would like to thank **Prof. Dr. Herbert Gleiter, Prof. Dr. Andreas Hütten, Prof. Dr. Chandrahas Bansal, Dr. Jörg Weissmüller, Dr. Norman Mechau** and **Dr. Ferdinand Evers** for the stimulating discussions I had with them. I would also like to convey my gratitude to all my colleagues in Hahn-group at INT, FZK for their continuous support and keeping the workgroup environment quite amusing. Especially, I would like to mention about **Dr. Mohammed Ghafari, Dr. Sylvio Indris, Philipp Leufke, Sebastian Gottschalk, Babak Nasr, Dr. Ajay Kumar Mishra, Simon Bubel, Anna Castrup, Mohsen Pouryazdan,** and **Martin Limbach.**

Special thanks to the secretaries, **Erika Schütze, Christine Batsch, Birgit Limmer** from INT, FZK and **Renate Hernichel** from TU Darmstadt for tolerating all the nuisance demands that I placed at times.

Financial Support provided by the Deutsche Forschungsgemeinschaft (DFG) through the DFG-Center for Functional Nanostructures (CFN) within sub-project D4.4 and the State of Baden-Württemberg is gratefully acknowledged.

I would also like to express my gratitude to my friends in FZK such as **Malla, Mahesh,** and **Ravi** for their companionship. Last but not the least, I would like to thank my family in India who always gave me moral support and encouragement whenever was needed.